Experimental and Numerical Investigation of Fatigue Behavior of Pearlitic Rail Steels

by

Seyed Babak Hassas Irani

A thesis submitted in partial fulfillment of the requirements for the degree of

Master of Science

Department of Mechanical Engineering
University of Alberta

Abstract

In recent years, rail transport of Canadian crude oil and coal has grown. While transportation of oil and coal by rail has demonstrated benefits, it has also raised significant concerns about transportation safety and potential impacts to the environment. In this regards, rolling contact fatigue (RCF) of railway components is one of the most crucial subjects to the safety of rail transportation. The RCF cracking is very sensitive to the microstructure of the rails which are mostly manufactured from pearlitic steels. Therefore, complete understanding of the effects of microstructural characteristics on the RCF phenomenon is critical for mitigating damage and life predictions so that components can be repaired or replaced in time before catastrophic failure occurs. In the current study, microstructural changes in pearlitic rail steels under fatigue loadings and their effects on the RCF crack initiation and propagation have been investigated by experimental and numerical approaches. Optical microscopy and micro-hardness testing are utilized to perform failure analysis on the rails that have been in service in the US. The morphologies and geometrical characteristics of the RCF cracks are analyzed. Moreover, the extent of plastic deformation in different regions of the rails is evaluated through microstructural analysis. Besides, other microstructural constituents including MnS based inclusions and white etching layers are evaluated. A microstructure-based model is built using Voronoi tessellation and continuum damage mechanics. The experimental results reveal that the maximum depths of cracks were mainly dependent on the grade of rail steel rather than the duration of service life. The maximum depths of the cracks were dependent on the thickness of largely deformed layer near the surface of the rails. Results of numerical simulations show occurrence of preferential strain accumulation in pro-eutectoid (PE) ferrite. As a result, a higher content of PE ferrite leads to a lower fatigue life of pearlitic rail steels.

To Ladan and Rasoul

Acknowledgements

I would like to express my deep gratitude to my supervisor, Dr. Zengtao Chen, for his guidance, patience and encouragement throughout my M.Sc. program. I would also like to offer my sincere appreciation to my co-supervisor, Dr. Daniel Szablewski from National Research Council of Canada (NRC), for his expertise, support and assistance.

I want to extend my thanks to the committee member, Dr. Chong-Qing Ru, for devoting his time and energy, reading my thesis and providing comments and recommendations. Additionally, I want to thank Eric E. Magel from NRC for providing me with the opportunity to collaborate with NRC's Automotive and Surface Transportation Research Centre.

I would like to gratefully acknowledge the financial support provided by Canadian Rail Research Laboratory (CaRRL). CaRRL is funded by the Natural Sciences and Engineering Research Council of Canada, Canadian Pacific Railway, Canadian National Railway, the Association of American Railways – Transportation Technology Centre Inc., the National Research Council of Canada, Transport Canada, and Alberta Innovates – Technology Futures.

Finally, I would like to thank my family and friends who always supported and encouraged me.

Table of Contents

List of Tables

List of Figures

1. Introduction

1.1 Motivation

In recent years, rail transport has grown as an alternative mode of transport of crude oil. According to a recent report by Canadian Association of Petroleum Producers (CAPP), about 185,000 barrels/day of Western Canadian crude oil was transported to market by rail. Rail volumes are estimated at around 500,000 b/d to 600,000 b/d for 2018 (CAPP 2015). Beside crude oil, rail transportation is critical to get coal to market. Canada's railroads move over 30 million tons of coal annually (CAC 2015). While transportation of oil and coal by rail has demonstrated benefits with respect to the efficient movement of oil and coal from producing regions to market hubs, it has also raised significant concerns about transportation safety and potential impacts to the environment. On 19 October 2013, a Canadian National (CN) freight train derailed 13 cars, including 4 tank cars containing petroleum crude oil and 9 tank cars of liquefied petroleum gas (LPG) near Gainford, Alberta. The train derailed when one or more rail breaks occurred due to the presence of numerous "transverse defects", which are caused by rolling contact fatigue (RCF), along the length of the high rail in the curve (TSB 2013).

The RCF phenomenon occurs in railways, gears, bearings, and other mechanical components involving rolling/sliding contact. In rails, frictional rolling/sliding contact causes plastic flow of the surface material. As the plastic deformation exceeds the fracture strain of the material, a surface crack is formed (Ekberg *et al.* 2014). RCF has both safety and economic consequences. Besides transverse rail breaks, surface initiated RCF cracks can result in a "no-test" condition during inspection by preventing the transmission and detection of ultrasonic waves. As a result, the inspector is required to stop the test and manually evaluate the rail using a

more sensitive system. This would significantly decrease the efficiency of the inspection and, hence reduce the availability of track (Ekberg & Kabo 2005; Magel 2011). Therefore, better understanding of RCF crack initiation and propagation mechanisms would be very useful to the Canadian rail sector as it would help with scheduling maintenance cycles, predicting failure and replacement.

1.2. Background

The RCF crack initiation and propagation is very sensitive to the microstructure of the rail steel which is dependent on composition and processing method (Beynon *et al.* 1996; Eden *et al.* 2005; Mughrabi 2015). Most rails are manufactured with pearlitic steels through continuous casting into bloom and then hot rolling to the required profile. Based on their composition and heat treatment, pearlitic rail steels can have different grain size, pearlite lamellae spacing and pro-eutectoid (PE) ferrite content (Cannon *et al.* 2003; Sahay & Totten 2009).

Cyclic rolling/sliding contact can significantly change the material properties and microstructure of pearlitic rail steels. It has been shown that strain partitioning occurs between PE ferrite and pearlite with preferential strain accumulation in PE ferrite. Consequently, initial crack initiation and growth mainly occurs along the favorably aligned strain-flattened PE ferrite boundaries (Eden *et al.* 2005; Garnham *et al.* 2007; Garnham & Davis 2008). In addition, surface layer of rails become anisotropic due to alignment of cementite lamellae in the pearlite colonies. It has been reported that the direction of cracks can be influenced by this anisotropy (Wetscher *et al.* 2007; Hohenwarter *et al.* 2011; Kapp *et al.* 2016). A numerical model has been developed by

Larijani *et al.* (2014) to investigate how the crack propagation in rail heads is influenced by this anisotropic layer.

Pearlitic rail steels also contain ductile nonmetallic inclusions in form of MnS based particles. Zhang *et al.* (2016) utilized various methods to characterize different morphologies of MnS inclusion in heavy rail steels. Influence of nonmetallic inclusions, including MnS particles, on mechanical properties of pearlitic rail steels was studied by Dhua *et al.* (2000). They observed that elongated MnS inclusions can act as initiation sites for fatigue cracks. This was also observed by Garnham *et al.* (2010) who investigated the role of MnS inclusions in RCF cracking.

A metallurgical feature which is commonly present on the surface of rails is white etching layer (WEL). Due to its resistance to metallographic etching, WEL appears featureless under optical microscopes (Carrol & Beynon 2007). There is no common view on the composition and formation mechanism of WEL in the literature. The main hypotheses are formation of martensitic WEL due to phase transformation (Pal *et al.* 2012; Wu *et al.* 2016) or severe plastic deformation (Al-juboori *et al.* 2017), and formation of nanocrsytalline ferritic WEL as a result of severe plastic deformation (Chen *et al.* 2016). It has been suggested that WEL is associated with RCF cracks on the rail surface (Rasmussen *et al.* 2017).

Most of the previously mentioned studies simulated the wheel/rail contact in a laboratory environment and there are limited results related to development of RCF in rails during service. For instance, Haidemenopoulos *et al.* (2016) conducted a metallographic investigation on a metro track that has been in service in Greece to determine the RCF cracks geometrical characteristics and their initiation and propagation mechanisms. In addition, subsurface

microstructure and mechanical properties of four rails that have been in use in the UK were evaluated by Alwahdi *et al.* (2013).

Numerical methods have also been utilized to investigate the relation between microstructural characteristics and RCF in pearlitic rail steels. Franklin *et al.* (2008) developed 2D microstructural models based on the "brick" model to evaluate the effect of PE ferrite content on the RCF crack initiation. However, the elements (or bricks) are independent of one another and therefore, the model is unable to capture the grain-grain interactions. In another study, Franklin *et al.* (2011) generated a 3D microstructural model using Voronoi tessellation to simulate the early stages of RCF crack propagation in pearlitic steels. But, this method is purely geometrical and the crack propagation procedure is not related to material properties.

1.3. Objective and Outline of Thesis

The primary objective of this thesis is to evaluate microstructural changes in pearlitic rail steels under fatigue loadings and their effects on RCF crack initiation and propagation. In chapter 2, the experimental failure analysis performed on the rails that have been in service in the US is presented. First, morphologies and geometrical characteristics of the RCF cracks are provided. Then, microstructural constituents and their relation to RCF cracks are discussed. Finally, the subsurface mechanical properties of the rails are evaluated. In chapter 3, a microstructure-based finite element model is developed based on Voronoi tessellation and continuum damage mechanics. The model is used to study the fatigue crack initiation and propagation mechanisms in pearlitic rail steels. Moreover, the effects of microstructural characteristics on fatigue life of these steels are investigated. Chapter 4 contains a summary of conclusions made in two previous chapters along with possibilities for future research.

2. Experimental Failure Analysis of Pearlitic Rail Steels in Service

2.1. Experimental Procedures

2.1.1. Rail samples

Five (5) rail samples were supplied by a U.S class I railroad company following their removal from a mainline freight track in November 2014. All of the rail samples were from high rail locations and had been in service for different length of time. Based on operational data provided by the company, traffic on these rails was about 21 million gross tons (MGT) per year.

Two (2) of the rail samples were from a line with 1° (degree) of curvature and were manufactured by US Steel (USS) in 1980 and 1972, respectively. Two months prior to their removal, these rails had been ground with a removal depth of approximately 0.22 mm. These rail samples are labeled as *Rail 1* and *Rail 2*, respectively (Figure 2.1).

Figure 2.1 Top view of running surface of the rail samples.

The other three (3) rail samples were removed from a line with 2° of curvature and had been produced by Rocky Mountain Steel Mills (RMSM), currently known as EVRAZ Rocky Mountain Steel, in 2002, 1994 and 2004, respectively. The grinding depth for these rails was

about 0.42 mm. These rail samples were termed correspondingly as *Rail 7*, *Rail 10* and *Rail 12* (Figure 2.1).

Visual inspection of Rail 1 and Rail 2 surfaces reveals moderate cracking at the mid-gauge regions in each of these rails. Rail 7 shows heavy cracking at the gauge and mid-gauge regions. Light cracking can be seen on top of Rail 10 and mid-gauge of Rail 12. There are also regularly spaced grooves on the surfaces of Rail 10 and Rail 12. These are grinding marks left over from the last grinding that took place prior to their removal.

2.1.2. Location of specimens

In order to survey railhead transverse and longitudinal planes, four (4) specimens were cut from each of the railhead samples. Cutting had to be performed carefully to avoid either the removal of existing cracks, the introduction of new cracks or the alteration of the microstructure. To prevent these things from happening, two large rail pieces were cut out using a band saw in transverse and longitudinal directions of each rail sample. Following that, a rotary cutting machine equipped with a diamond disk was used to cut and trim the pieces into the shape of final specimens.

As shown in Figure 2.2, the specimens were labeled based on the cutting plane and location. *Transverse Top* (TT) specimens showed transverse plane of top of the rails. *Transverse Gauge* (TG) specimens covered the mid-gauge and gauge corner of the rails. Longitudinal plane of mid-gauge of the rails was investigated through *Longitudinal Top* (LT) specimens. *Longitudinal Gauge* (LG) specimens were used to evaluate the longitudinal plane of gauge corner of the rails.

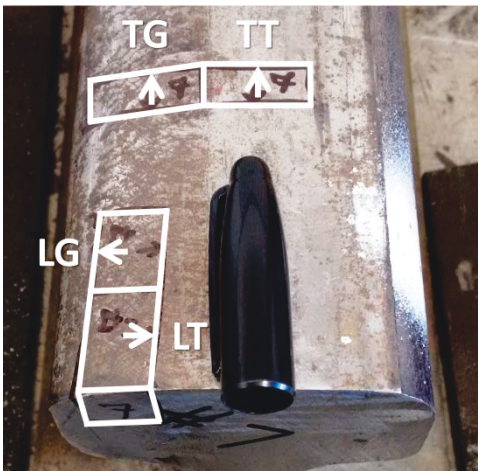

Figure 2.2 Cutting locations of transverse (TT and TG) and longitudinal (LT and TT) specimens.

2.1.3. Metallography and optical microscope

Edges of the specimens were supposed to be ground by 180 grit Silicon Carbide (SiC) papers prior to mounting in resin. This was done to prevent mount cracking at sharp corners. They were then cold mounted using epoxy resin. Since the specimens were much larger than conventional metallography specimens, it would be too time-consuming to grind their surface with SiC papers. Composite grinding disks with 45 and 15 µm diamond suspension were used instead. Then, the specimens were polished with 9 and 3 µm diamond and 0.05 µm alumina (Al_2O_3) pastes. All grinding and polishing was done using a Buehler EcoMet 4 Grinder-Polisher semi-automatic unit, and images were taken using an Olympus GX71 optical microscope equipped with a CLEMEX 1.3C camera (Figure 2.3).

Since the specimens were cracked, particles from the grinding/polishing step(s) may have remained in the cracks and resulted in scratching of the surface in the finer grinding/polishing steps. These scratch marks would appear as artifacts in the acquired images. To avoid this, the specimens were rinsed under cold running water between each grinding/polishing step. They

were then cleaned in an ultrasonic bath filled with soapy water, rinsed with distilled water, and were forced air-dried. This ensured a scratch free mirror finish on the samples.

Figure 2.3 Grinder-polisher and optical microscopy equipment.

2.1.4. Crack path analysis

The mirror-polished specimens were used to investigate the crack paths. In some of the specimens, the cracks extended over multiple fields-of-view (FOV) at the lowest microscope setting of 50X magnification. In those cases it was impossible to cover the entire crack length with a single image. As a result, several images were taken and then MosaicJ and Stitching plugins of the Image Processing and Analysis software Fiji (Schindelin *et al.*2012; Thevenaz & Unser 2007; Preibisch *et al.* 2009; Najdahmadi *et al.* 2018) were used to stitch the images together. As illustrated in Figure 2.4, acquired geometrical characteristics of the cracks included the following: length (L), depth perpendicular to the running surface (H), angle to the running surface (θ) and spacing between cracks (S). The Fiji software was utilized for these measurements.

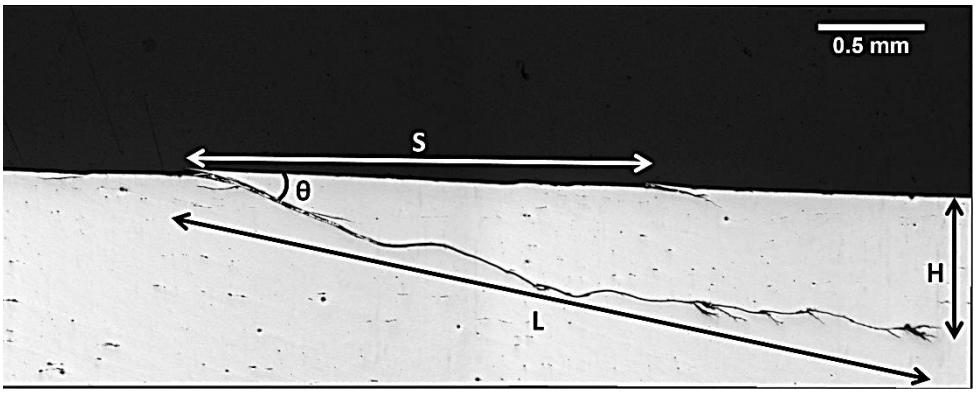

Figure 2.4 Measured geometrical characteristics of cracks.

2.1.5. Microstructural analysis

For microstructural analysis, two categories of specimens, namely LT and TG, were chosen (Figure 2.2). The reason for choosing LT specimens was that mid-gauge is the primary region that experiences wheel/rail (W/R) contact forces (Zhou *et al.* 2014) and it plastically deforms mainly in the longitudinal direction. TG specimens were chosen to evaluate lateral plastic deformation at gauge and mid-gauge regions. The specimens were etched using 2% Nital (2 ml nitric acid and 98 ml ethanol) solution at variable soak times (5 to 10 seconds depending on polished surface reaction to the etchant).

Optical images of the etched LT samples were used to measure the depth of plastic deformation. As demonstrated in Figure 2.5, the measurements were done using the areas that showed optically visible plastic deformation such as shear deformation. It should be noted that this method is subjective because it is possible that an area is plastically deformed without showing optically visible microstructural changes. In such cases, plastic deformation results in dislocation density increase which can be measured using hardness measurements or scanning electron microscopy (Davis *et al.* 2013), as discussed in the next section.

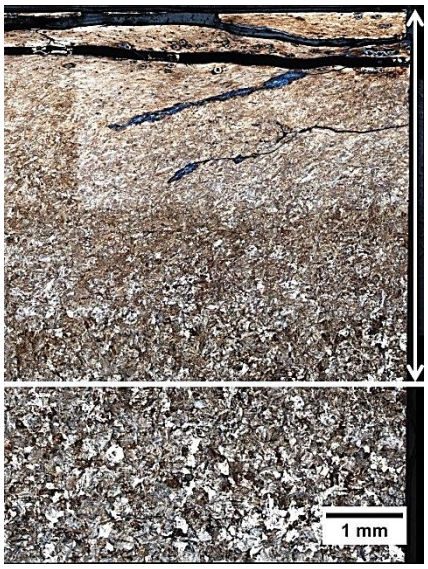

Figure 2.5 Typical measurement of depth of plastic deformation.

2.1.6. Hardness measurements

Hardness measurements were conducted on transverse specimens using the Vickers hardness test method. The measurements were done using a LECO LM 247AT micro-hardness tester (Figure 2.6a) with a 50 g load according to ASTM E384 (2016) standards. The measurements started at the depth of 50 to 80 μm from running surface and continued to an approximate depth of 3000 μm (3 mm). The least squares method was utilized to fit the hardness values of each specimen with polynomial trendlines (n=6). The hardness value at the depth of 3 mm was considered as representative of the bulk rail hardness.

As shown in Figure 2.6b, within about 1.5 mm from the surface, the measurements were done along three (3) lines normal to the surface. Then, up to a depth of 3 mm, just one line of measurement was used. The spacing between indentations was at least 2.5 indentation diameters. This was done to avoid interference between individual indentations.

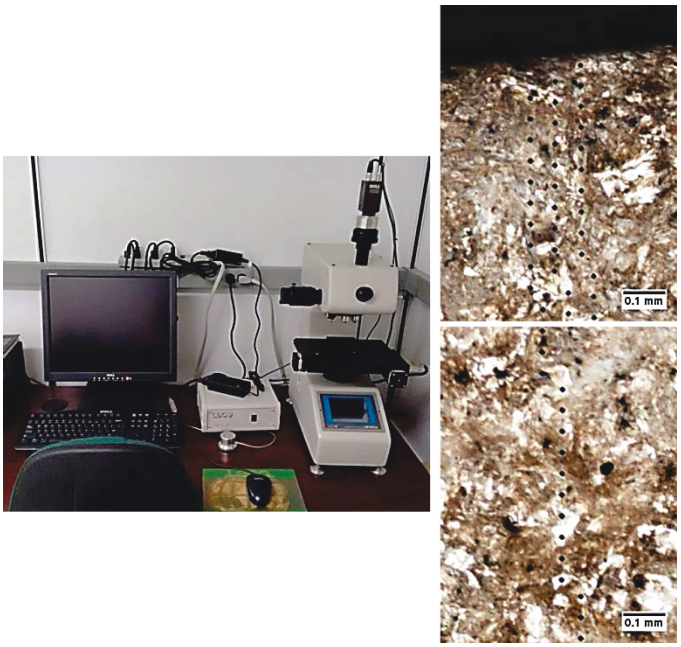

(a) (b)

Figure 2.6 (a) Micro-hardness tester (b) Indentation patterns.

2.1.7. Identification of rail grade

The steel grades of the analyzed rail samples were identified based on their bulk hardness values according to chapter 4 of AREMA Manual for Railway Engineering (2010) specifications. In addition, the grain structures of the rail samples were compared to each other in a qualitative manner (Figure 2.7). Rail 1 microstructure consisted of coarse pearlite grains and it had a bulk hardness of 300 HV, which indicate a standard grade rail steel. Microstructure of Rail 2 was similar to Rail 1 and the rail indicated a bulk hardness of 310 HV, which categorize it as a standard rail. Rail 7 had a finer grain structure in compare to two previous rails and with a bulk hardness of 365 HV it can be considered as an intermediate rail. Microstructure of Rail 10 included fine pearlite grains and the rail had a bulk hardness of 450 HV which represent a premium rail. Rail 12 is also a premium rail and had very fine grain structure and bulk hardness of 410 HV.

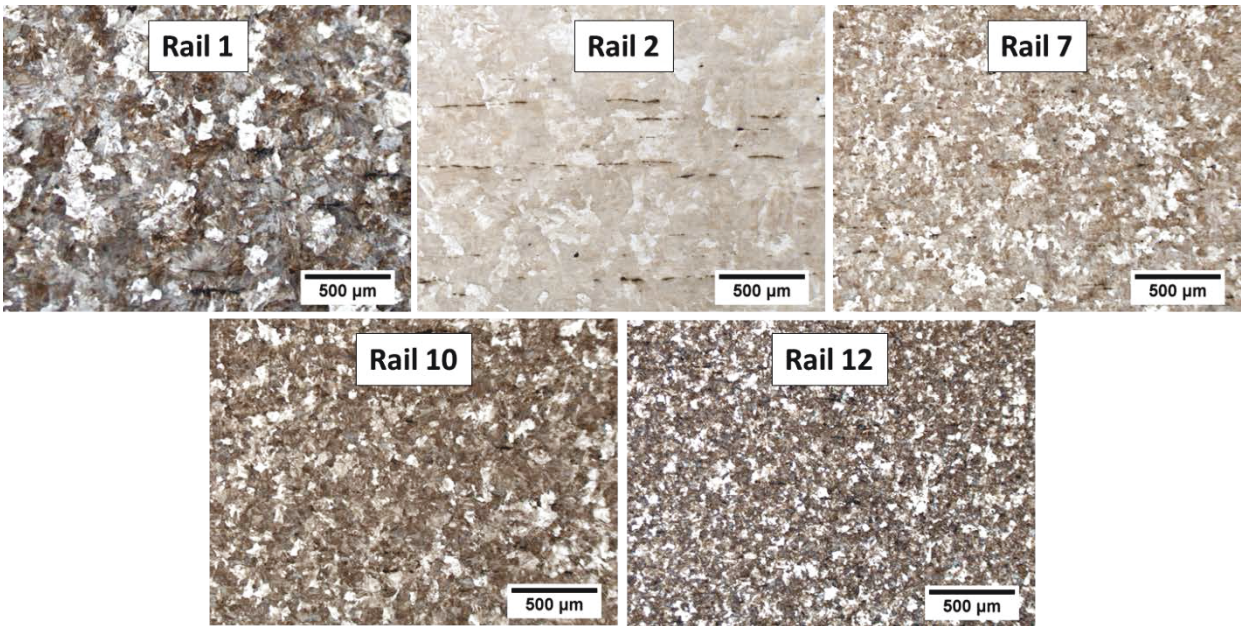

Figure 2.7 Undeformed microstructure of the rail samples.

2.2. Results and Discussion

2.2.1. Crack path analysis

Rail 1: As shown in Figure 2.8, Examination of **Rail 1-TG** specimen revealed that ***delamination*** was the main damage process at the gauge. The damage mechanism can be divided into three (3) stages: First, the crack initiates at a very small angle relative to the gauge surface. Then, the crack propagates downward to its maximum depth (relative to the gauge surface). In the 3rd stage, the crack changes its direction and propagates back toward the gauge surface. In some cases, the crack path reaches the gauge surface, so the material above the crack is no longer attached to the rail and it spalls from the surface. For Rail 1-TG specimen, the initiation angles were under 8°, the maximum depths were approximately between 50 and 80 µm and crack path length were mostly between 600 and 700 µm.

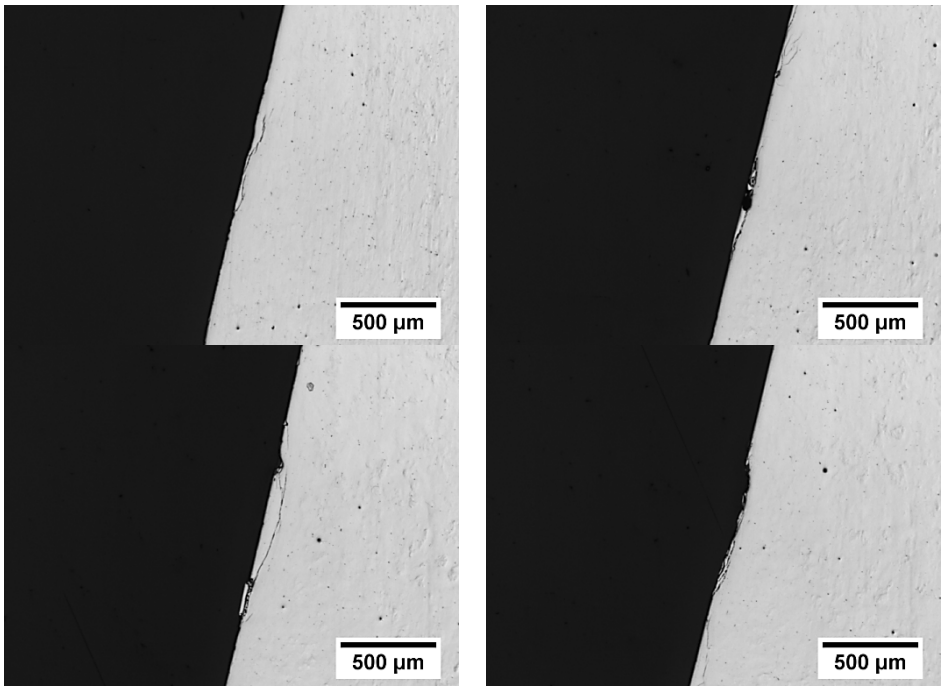

Figure 2.8 Delaminations at the gauge region of Rail 1 (Rail 1-TG).

As demonstrated in Figure 2.9a, The **Rail 1-TG** specimen showed cracks that had initiated in the mid-gauge region and propagated horizontally toward the top of rail region. These cracks had angles between 14° and 17° relative to the rail running surface. The two (2) major cracks had (partial and total) lengths of 14846 and 9206 µm and their depths were 1377 and 2222 µm, respectively. ***Crack shielding*** might be the reason that propagation of one of the major cracks had been halted. Based on this concept, when two cracks initiate close to each other, only one of them will be able to propagate further because the other one will be in a stress relieved zone (Tillberg *et al.* 2008). Besides the major cracks, another crack that seemed to be a ***subsurface crack*** was observed (Figure 2.9b). It is known that sub-surface cracks in rail steels are mainly initiated by brittle inclusions. However, since the 1970's, rail steels are mostly free of these inclusions (Garnham *et al.* 2010). The possible explanation is that the observed sub-surface crack was a portion of a surface initiated crack and the whole crack path was not captured in this cross section.

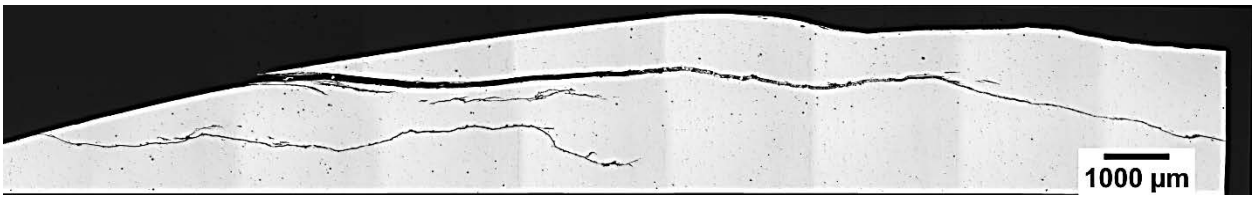

(a)

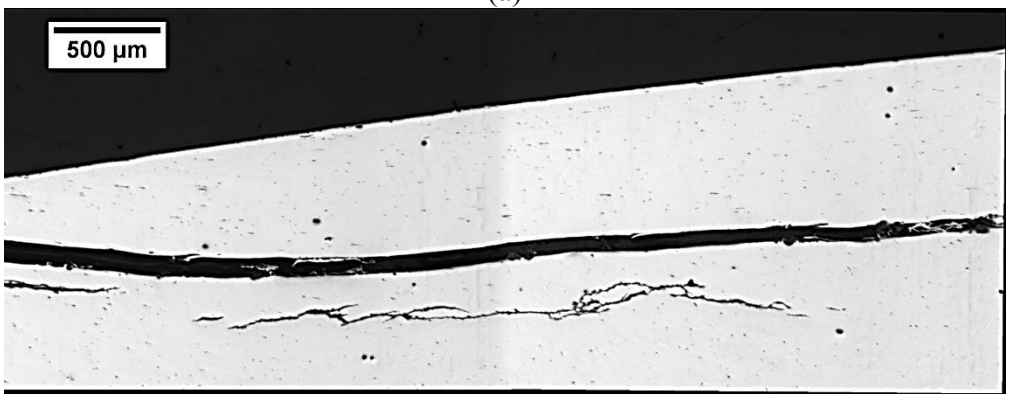

(b)

Figure 2.9 (a) Cracks in the mid-gauge region of Rail 1 (b) Suspected sub-surface crack at higher magnification (Rail 1-TG).

Rail 1-TT specimen exhibited two (2) cracks with depths of 3053 and 2545 µm in the top of rail region (Figure 2.10). These were most likely a continuation of cracks that had initiated in the mid-gauge region.

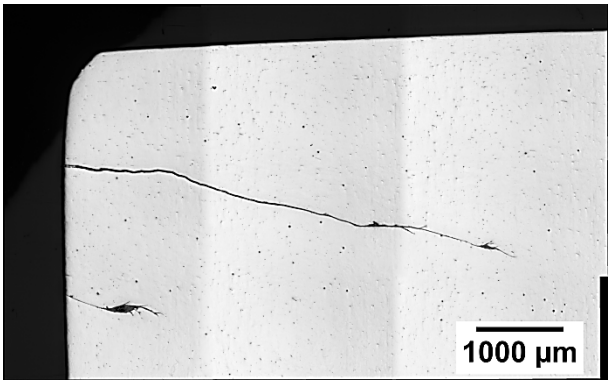

Figure 2.10 Cracks in the top of rail region of Rail 1 (Rail 1-TT).

As shown in Figure 2.11, **Rail 1-LG** specimen showed cracks that mainly had angles between 8° and 17°. The three (3) major cracks had lengths of about 5004, 7484 and 3624 µm and depths of 941, 1409 and 688 µm, respectively. Again, it was observed that one of the major cracks had been shielded.

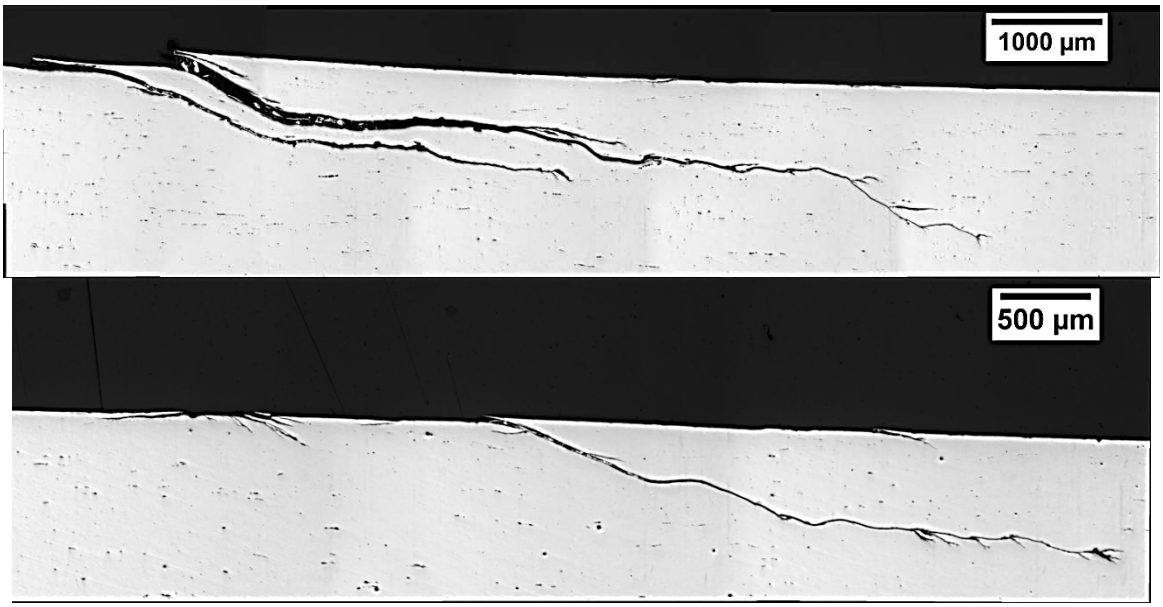

Figure 2.11 Crack in longitudinal section of the gauge region of Rail 1 (Rail 1-LG).

Evaluation of **Rail 1-LT** specimen revealed severe damage in the mid-gauge region and a network of cracks (Figure 2.12). Since the cracks were connected, it was impossible to distinguish them individually. Therefore, it was only feasible to measure the maximum depth of these cracks, which was 2219 µm.

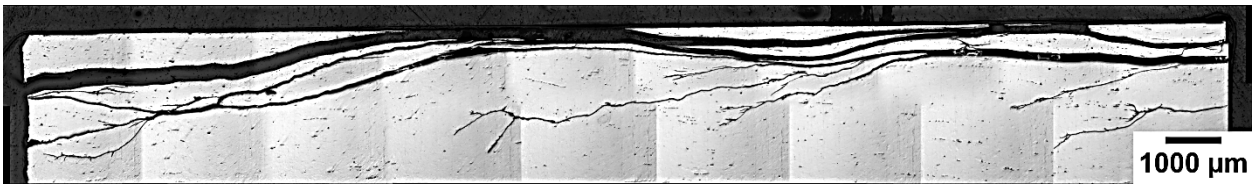

Figure 2.12 Cracks in longitudinal section of the mid-gauge region of Rail 1 (Rail 1-LT).

Rail 2: Similar to Rail 1-TG specimen, delamination was the main damage mechanism at the gauge region of **Rail 2-TG** specimen, but it was more severe in Rail 2-TG than in Rail1 (Figure 2.13a). Multiple delaminations were found in clusters and the lengths of these clusters were between 1100 and 1400 µm. It was observed that the bottom of gauge region had been plastically deformed which had resulted in a ***plastic flow lip*** (Figure 2.13b). A number of cracks had initiated at the plastic flow lip which had angles between 70° to 90°, lengths between 100 and 150 µm and depths between 50 to 150 µm.

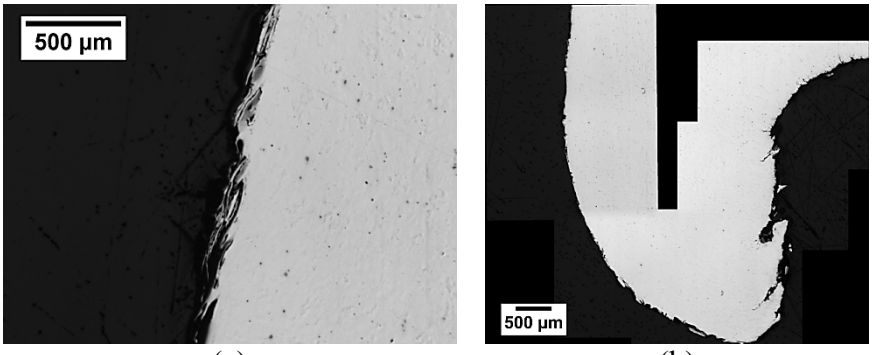

(a) (b)

Figure 2.13 (a) Delamination at the gauge region of Rail 2 (b) Plastic flow lip (Rail 2-TG).

As shown in Figure 2.14a, **Rail 2-TG** specimen also revealed two (2) major cracks in the mid-gauge region with angles of 15° and 10°, (partial and total) lengths of 10185 and 5176 µm and depths of 1773 and 420 µm, respectively. The cracks had initially propagated horizontally but changed their growth direction in the middle of their path. The larger crack diverted downward while the other crack propagated upward to a point very close to the rail running surface. If it had reached the surface, then it would have resulted in a large spall.

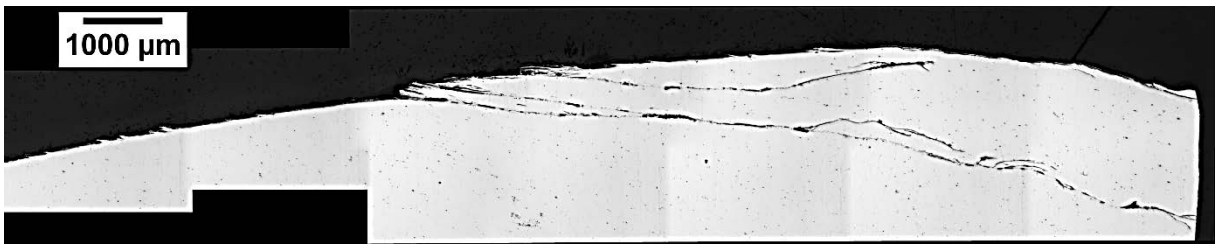

(a)

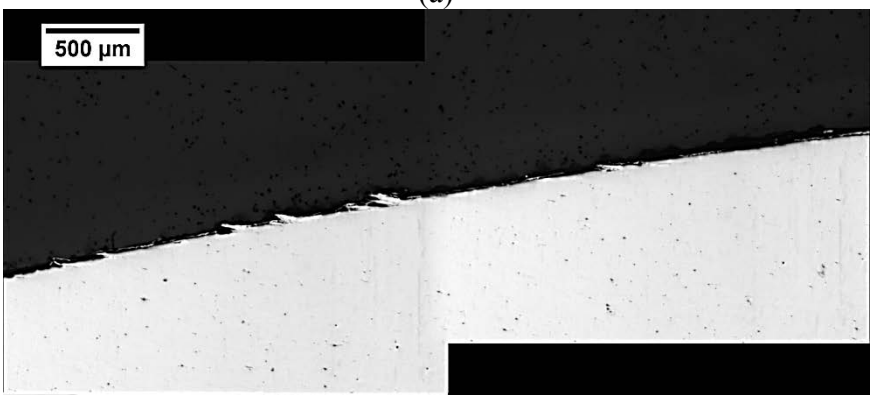

(b)

Figure 2.14 (a) Cracks in the mid-gauge region of Rail 2 (b) shallow surface cracks (Rail 2-TG).

In addition, ***shallow surface cracks*** were found in clusters at the mid-gauge region of Rail 2-TG specimen (Figure 2.14b). These cracks had angles of approximately 20° to 25°, lengths between 100 and 150 µm and depth of about 30 to 40 µm. Evaluation of **Rail 2-TT** specimen showed continuation of a crack from mid-gauge region which had a depth of 1823 µm.

As demonstrated in Figure 2.15a, **Rail 2-LG** specimen exhibited a major crack with an angle of 6 °, length of 7809 µm and depth of 813 µm. Besides the major crack, clusters of

shallow surface cracks were observed on the running surface of the specimen (Figure 2.15b). In comparison to the shallow surface cracks found on Rail 2-TG specimen, these cracks were shallower (their angles were mostly between 10° and 15° and their depths were mainly between 20 and 30 μm) but had greater lengths (between 100 and 250 μm).

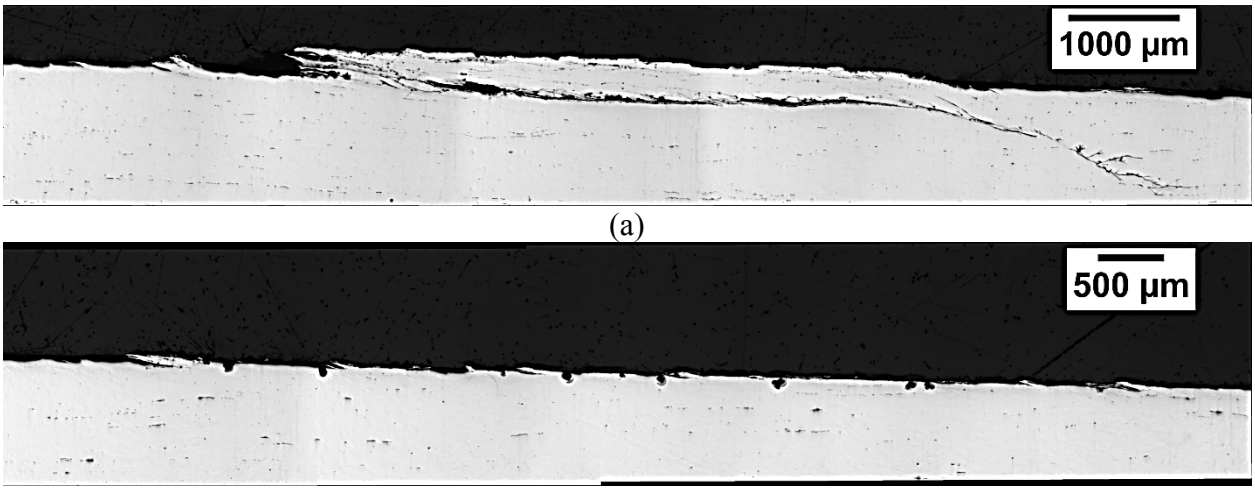

(a)

(b)

Figure 2.15 (a) Cracks in longitudinal section of the gauge region of Rail 2 (b) Shallow surface cracks (Rail 2-LG)

For **Rail 2-LT** specimen, the cracks had angles between 10° and 15° (Figure 2.16). The two (2) major cracks had lengths of 9438 and 14473 μm and depths of 1743 and 2409 μm, respectively. Also, two (2) smaller cracks were found which had lengths of 3466 and 3853 μm and depths of 985 and 665 μm.

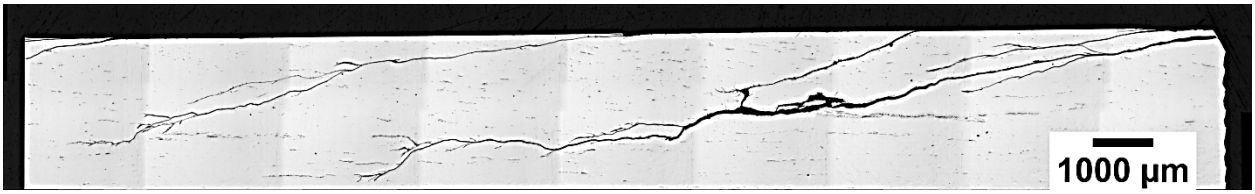

Figure 2.16 Cracks in longitudinal section of the mid-gauge region of Rail 2 (Rail 2-LT)

Rail 7: No trace of delamination or other types of damage was found at the gauge region of the **Rail 7-TG** specimen. This might have been due to the fact that the gauge of Rail 7 was smaller than to other rail samples. It was observed that five (5) cracks had initiated at gauge corner and mid-gauge regions and propagated horizontally toward the top of rail region (Figure 2.17a). This indicated ***gauge corner cracking*** (GCC) as the main cause of failure. The initiation angles of the cracks were between 10° and 20°. Total lengths of the two (2) major cracks that had initiated at the gauge corner region were 10218 and 11786 μm and their depths were 2336 and 2610 μm, respectively. The other three (3) major cracks had partial lengths of 8144, 5443 and 3470 μm and their depths were 1877, 1063 and 711 μm, respectively. **Rail 7-TT** specimen revealed two (2) major cracks that were continuations of cracks from the mid-gauge region (Figure 2.17b). Partial lengths of the cracks were 4747 and 6129 μm and their depths were 2420 and 1751 μm, respectively.

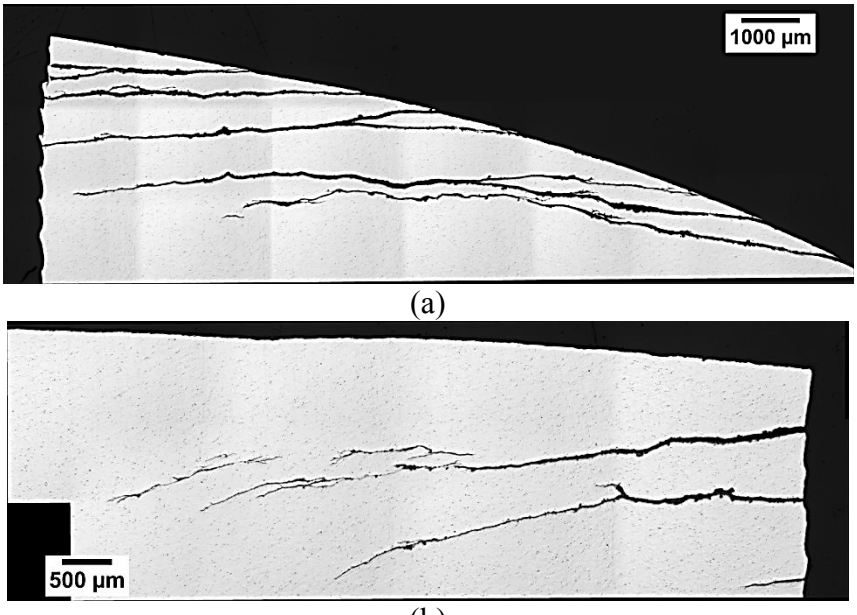

(a)

(b)

Figure 2.17 Cracks at the (a) mid-gauge and (b) top of rail region of Rail 7 (Rail 7-TG and TT, respectively).

Five (5) cracks, which had angles between 20° to 25°, were observed at the surface of **Rail 7-LG** specimen. As shown in Figure 2.18a, the three (3) major cracks had lengths of about 1993, 3622 and 4132 μm and depths of 721, 1216 and 1321 μm, respectively. **Rail 7-LT** specimen showed a number of cracks which had average spacing of 2176 μm and were parallel to each other (angles around 20°) (Figure 2.18b). Their lengths were between 1799 and 8525 μm (average length of 5210 μm) and their depths were between 940 and 2863 μm (average depth of 1960 μm).

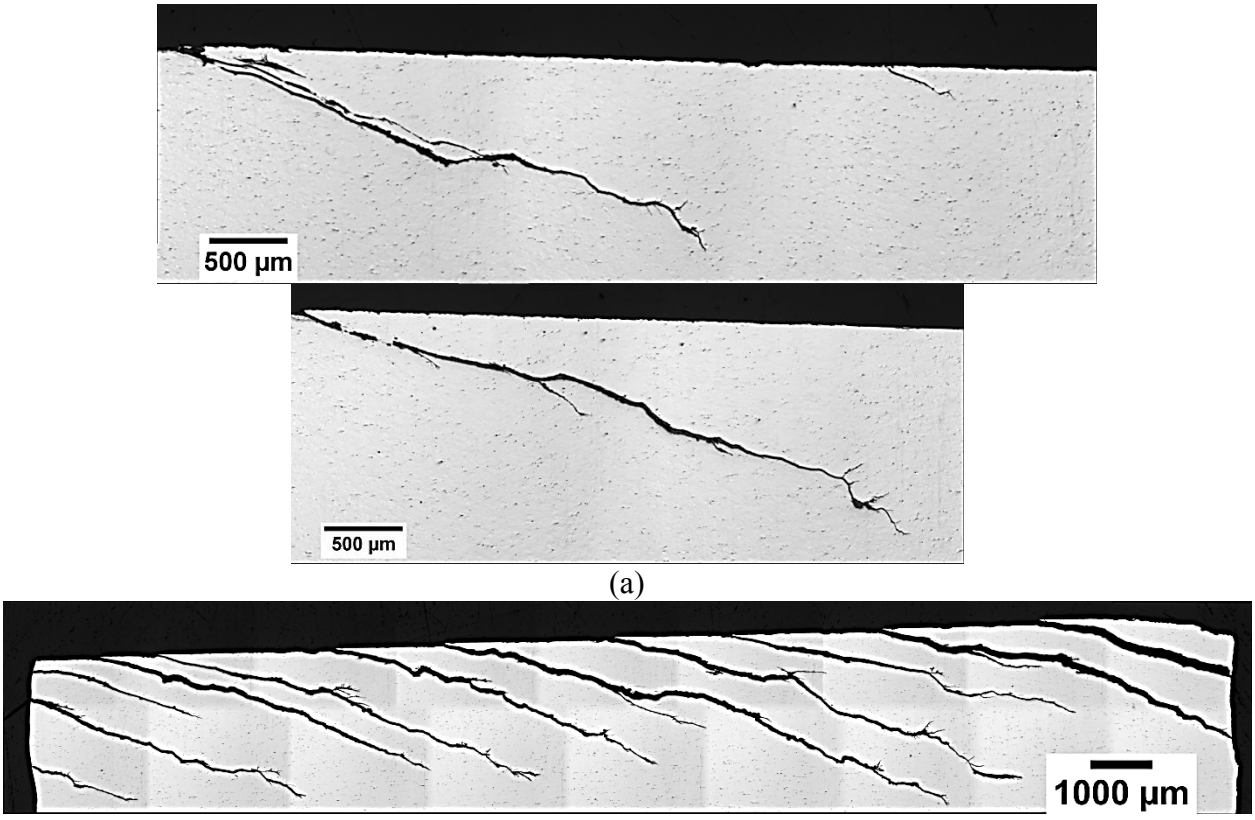

Figure 2.18 Cracks in longitudinal section of the (a) gauge and (b) mid-gauge region of Rail 7 (Rail 7-LG and LT, respectively).

The findings so far showed that the main cause of failure in Rail 1, 2 and 7 was RCF cracking at the gauge corner and mid-gauge regions. One interesting finding was that while the rails had been in service for different lengths of time, the cracks had propagated to almost the

same maximum depth in all of the LT specimens (2219 μm in Rail 1, 2409 μm in Rail 2 and 2863 μm in Rail 7). As mentioned before, the LT specimens represent longitudinal planes in mid-gauge region which is the primary region that experiences contact forces. Therefore, the LT specimens are suitable for a comparison of maximum depth of cracks in these rail samples. In addition, since Rail 7 was made of intermediate grade rail steel, it should have a higher resistance to RCF cracking in comparison to Rails 1 and 2 which were made of standard grade rail steel. However, measurements indicated that RCF damage in Rail 7 was more severe than in Rails 1 and 2.

Rail 10: As shown in Figure 2.19a, it was observed that delamination was again the main damage mechanism at the gauge region of **Rail 10-TG** specimen. But, it was much less severe than Rails 1 and 2. The crack initiation angles were under 8° and their final lengths were mainly between 150 and 300 μm. The plastic deformation at the bottom of the gauge region was excessive resulting in a severely deformed plastic flow lip (Figure 2.19b). Similar to Rail 2, a number of cracks had initiated at the plastic flow lip. The geometrical characteristics of these cracks were similar to the ones in Rail 2 (angles between 70° to 90°, lengths between 100 and 150 μm and depths of between 50 to 150 μm).

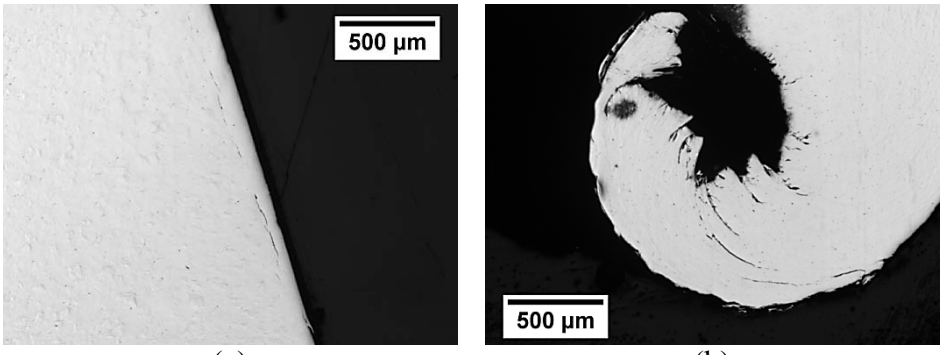

(a) (b)

Figure 2.19 (a) Delamination at the gauge region of Rail 10 (b) Plastic flow lip (Rail 10-TG).

The damage pattern at the gauge corner and mid-gauge regions of the **Rail 10-TG** specimen (Figure 2.20) was very different from the previous rail samples. There was only one (1) short major crack in the mid-gauge region of Rail 10-TG specimen. The crack had an angle of 22º, a length of 1268 µm and a depth of 563 µm. Besides this major crack, a number of shallow surface cracks were observed at the mid-gauge region of the specimen. Theses cracks had angles mostly between 10° and 15°, lengths of about 130 to 200 µm and depths of 20 to 30 µm.

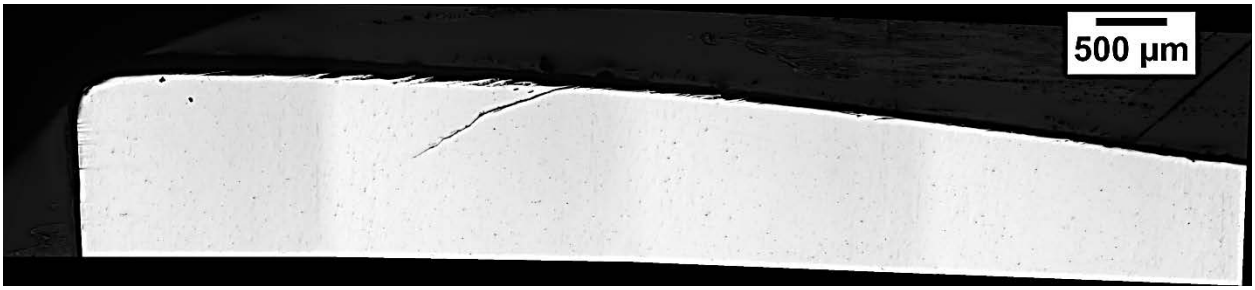

Figure 2.20 Cracks in the mid-gauge region of Rail 10 (Rail 10-TG).

As demonstrated in Figure 2.21 and Figure 2.22, **Rail 10-TT** specimen revealed a number of major cracks in the top of rail region. Two distinct zones were observed in relation to the angles of the major cracks. In the first zone (Figure 2.21), which was close to the mid-gauge region, crack angles gradually increased from 35° to 70°. The maximum depth of major cracks in this zone was 586 µm. In addition, shallow surface cracks with geometrical characteristics similar to the ones from mid-gauge region were observed in this zone. In the second zone (Figure 2.22), the cracks are almost vertical to the rail running surface and they did not show traces of shallow surface cracks. These ***vertical short cracks*** are similar to cracks that occur due to presence of a brittle phase such as martensite (Steenbergen 2015; Najdahmadi *et al.* 2014). The measured maximum depth of cracks in this second zone was 509 µm.

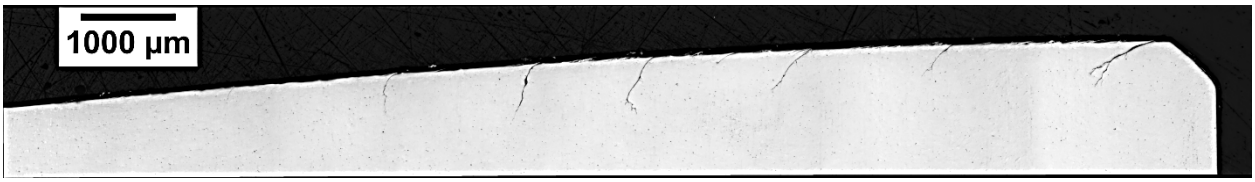

(a)

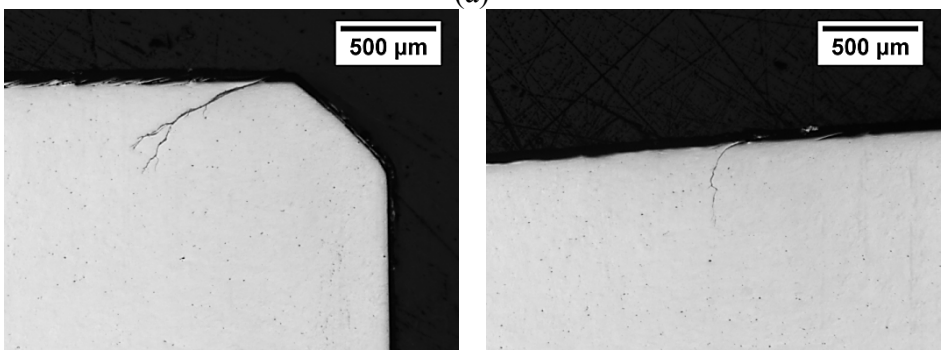

(b)

Figure 2.21 (a) Cracks in the first zone of the top to rail region of Rail 10 (b) Cracks at higher magnification (Rail 10-TT).

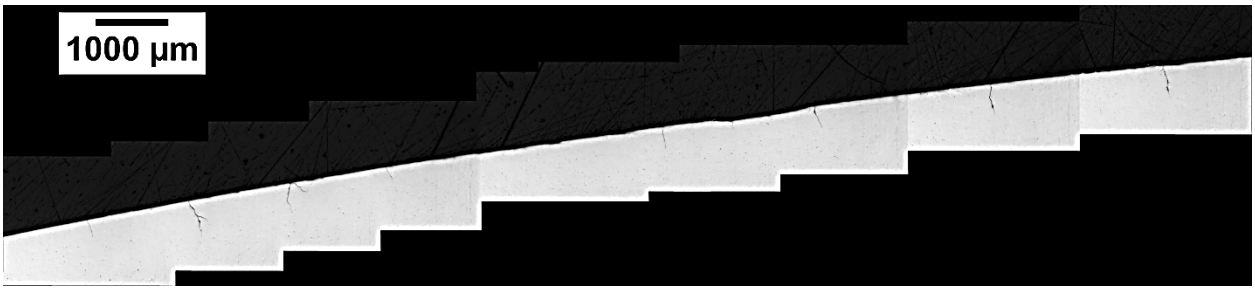

(a)

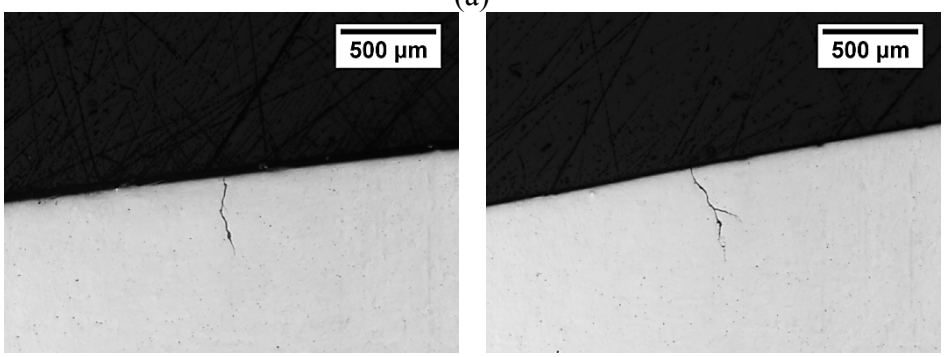

(b)

Figure 2.22 (a) Cracks in the second zone of the top of rail region of Rail 10 (b) Cracks at higher magnification (Rail 10-TT).

Rail 10-LG specimen showed delamination as the main cause of failure, and there were no major cracks on the rail running surface (Figure 2.23). As shown in Figure 2.24, a number of cracks were observed on the running surface of **Rail 10-LT** specimen. The cracks had angles between 20° and 25°. Based on their lengths, the cracks could be categorized into three types: short, medium and long cracks. The two (2) long (major) cracks had lengths of 1462 and 1815 μm and depths of 510 and 661 μm, respectively. The lengths of two (2) medium cracks were 804 and 515 μm and their depths were 366 and 319 μm. The short cracks had lengths between 200 and 350 μm and their depths were between 75 and 125 μm.

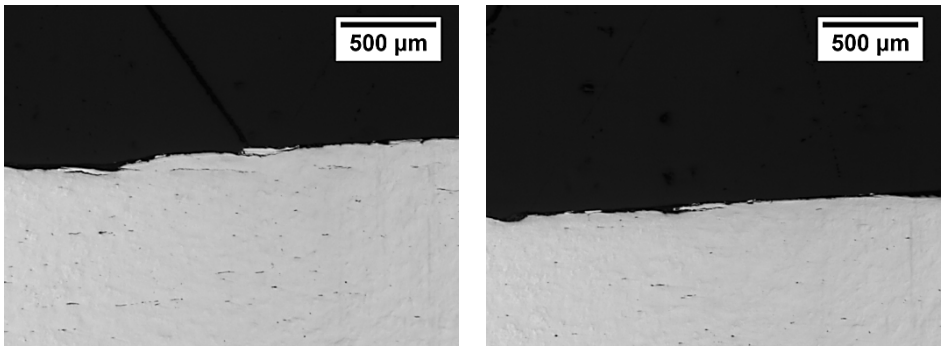

Figure 2.23 Delamination in longitudinal section of the gauge region of Rail 10 (Rail 10-LG).

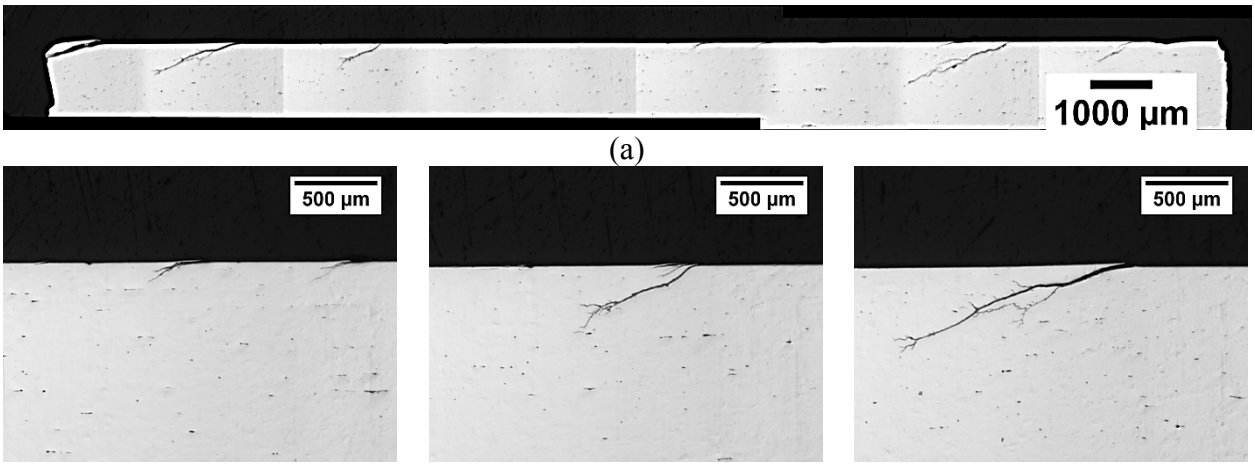

(a)

(b)

Figure 2.24 (a) Cracks in longitudinal section of the mid-gauge region of Rail 10 (b) Cracks at higher magnification (Rail 10-LT)

Rail 12: As shown in Figure 2.25, several delaminations were observed at the gauge region of **Rail 12-TG** specimen. Rail 12-TG specimen also showed four (4) major cracks along with a number of shallow surface cracks in the mid-gauge region (Figure 2.26). The major cracks had angles between 25° and 40°. The longest one had a length of 954 µm and a depth of 610 µm. The three other cracks had lengths between 441 and 584 µm and depths between 185 to 371 µm. Evaluation of **Rail 12-TT** specimen revealed that shallow surface cracks with angles between 13° and 18° were the main cause of damage at the top of rail region (Figure 2.27). Most of these cracks had lengths between 30 and 70 µm and depths between 20 and 30 µm. A short vertical crack with a length of 280 µm was also observed.

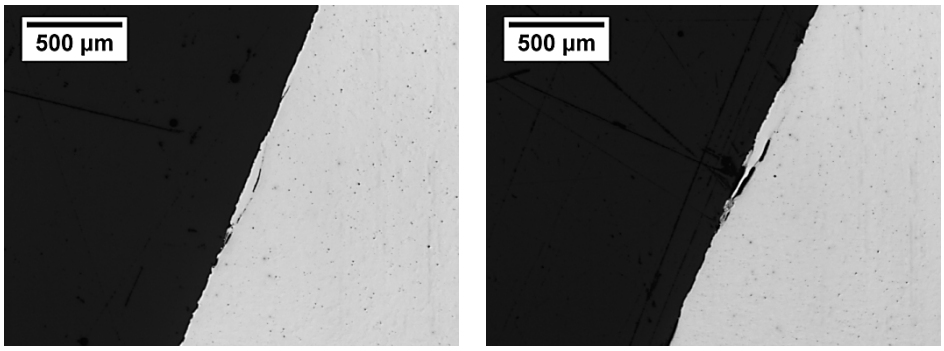

Figure 2.25 Delaminations at the gauge region of Rail 12 (Rail 12-TG)

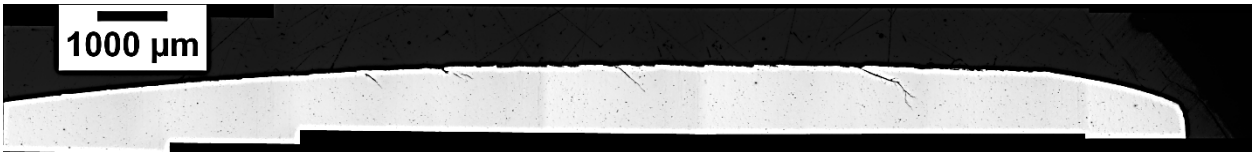

(a)

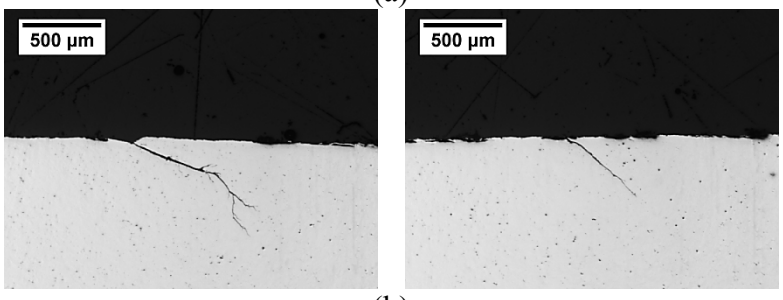

(b)

Figure 2.26 (a) Cracks in the mid-gauge region of Rail 12 (b) Cracks at higher magnification (Rail 12-TG)

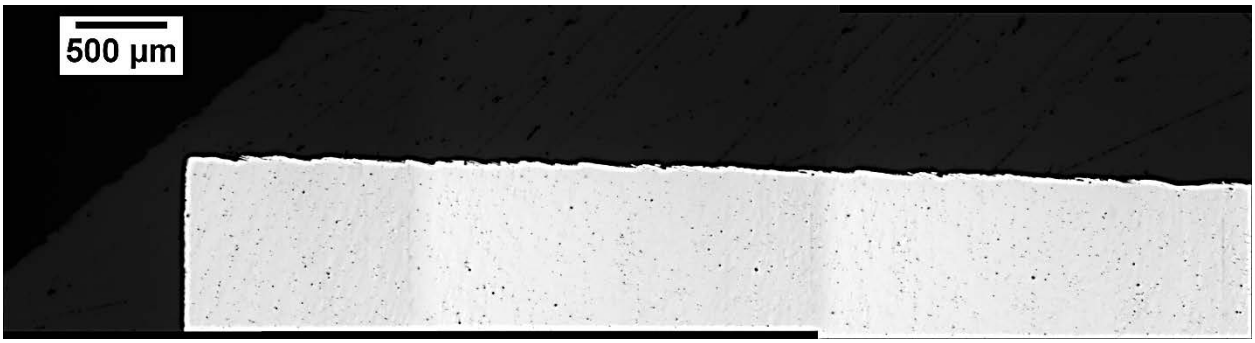

Figure 2.27 Shallow surface cracks in the top of rail region of Rail 12 (Rail 12-TT)

Rail 12-LG specimen showed a number of cracks which were evenly spaced (average spacing of 1,887 µm) and parallel to each other (angles between 20° and 30°) (Figure 2.28a). Their lengths were between 117 and 1,250 µm (average length of 568 µm) and their depths were between 30 and 482 µm (average depth of 222 µm). As shown in Figure 2.28b, **Rail 12-LT** specimen exhibited three (3) major cracks with angles of 30°, 20° and 25°. The three major cracks had lengths of 820, 1199 and 599 µm and depths of 420, 426 and 260 µm, respectively. Several shallow surface cracks were also observed.

(a)

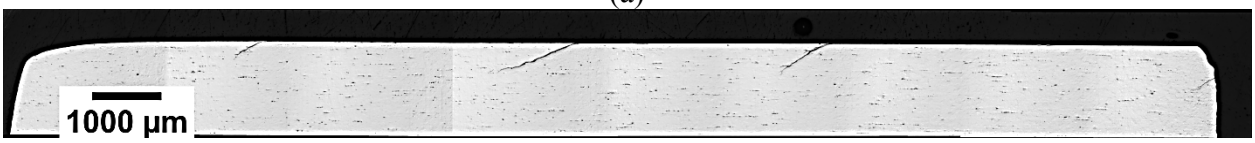

(b)

Figure 2.28 Cracks in longitudinal section of the (a) gauge and (b) mid-gauge region of Rail 12 (Rail 12-LG and LT, respectively).

It was observed that, while Rail 10 and 12 (which were made of premium grade steels) had different service times, the maximum depths of cracks in the LT specimens were the same (661 μm in Rail 10 and 610 μm in Rail 12). Considering that similar trend was observed for the three other rails, it seems that under the same traffic conditions, the maximum depths of cracks (in mid-gauge region) was mainly dependent on the rail steel grade rather than the rail in-service life. For Rails 1, 2 and 7, the major cracks crossed multiple regions: cracks initiated at the rail gauge corner and mid-gauge regions and then propagated toward the top of rail region. But, for Rails 10 and 12, the major cracks were confined to a specific region; top of rail region in Rail 10 and mid-gauge region in Rail 12.

2.2.2. Microstructural analysis

2.2.2.1. Plastic deformation

Rail 1: As shown in Figure 2.29, Etched **Rail 1-LT** specimen revealed that the microstructure consisted of three (3) regions with respect to plastic deformation: *largely deformed*, *mildly deformed* and *undeformed* regions. It should be mentioned that only the observed plastic deformation was taken into account. The largely deformed region (region I in the Figure 2.29) covered the area from running surface of the specimen to a depth of 2505 μm. Examination of this region at higher magnification showed that the area close to the surface had undergone severe plastic deformation where plastic deformation lines were parallel to the surface (Figure 2.30a). Due to severe plastic deformation, pearlite colonies were fragmented and transformed into a ***layer-like structure***. Linz *et al.* (2015) investigated the formation of the layer-like structure by the means of electron backscatter diffraction (EBSD). They proposed that in order to allow plastic strains in later stages of damaging regime, cementite lamellae break into shorter pieces. Then, the broken lamellae aligned parallel to the rail running surface which

results in a distinct layer. Below this layer-like structure, deformation of pearlite colonies was observed (Figure 2.30b). It was also observed that the angle between the plastic deformation lines and the normal to rail surface (which indicates shear strain) (Tyfour *et al.* 1996) gradually decreased as the depth from the surface increased. The mildly deformed region (region II) which had experienced small shear strains was observed between the depths of 2505 and 4788 µm (Figure 2.31a). No plastic deformation (region III) was observed in the microstructure below depth of 4788 µm (Figure 2.31b).

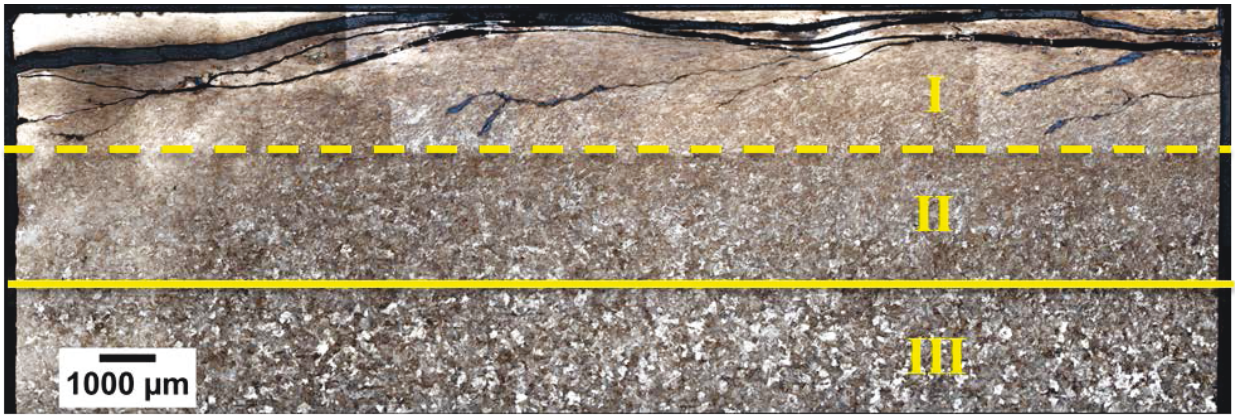

Figure 2.29 (I) Largely deformed, (II) Mildly deformed and (III) Undeformed regions in longitudinal section of the mid-gauge region of Rail 1 (Etched Rail 1-LT).

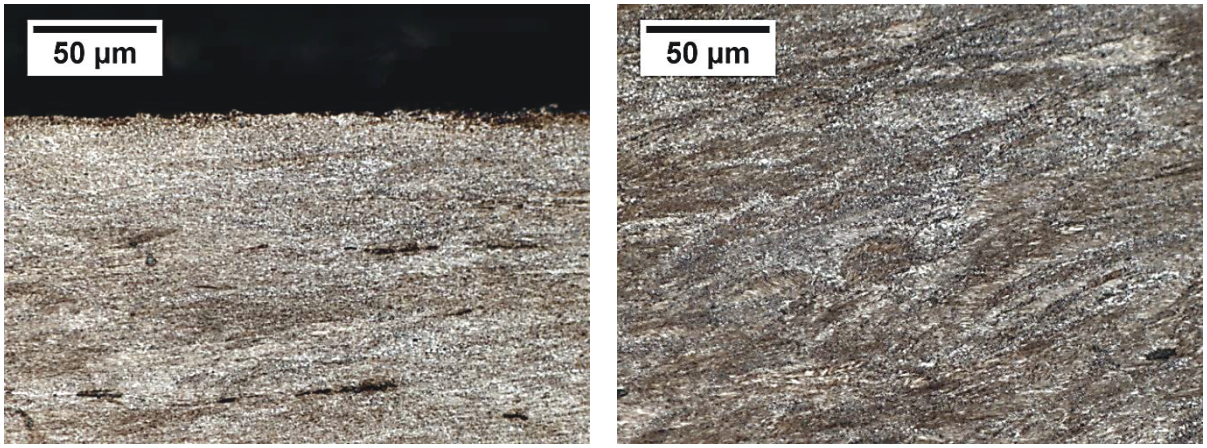

(a) (b)

Figure 2.30 Largely deformed region (region I) at higher magnification: (a) Layer-like structure (b) Deformed pearlite colonies (Etched Rail 1-LT).

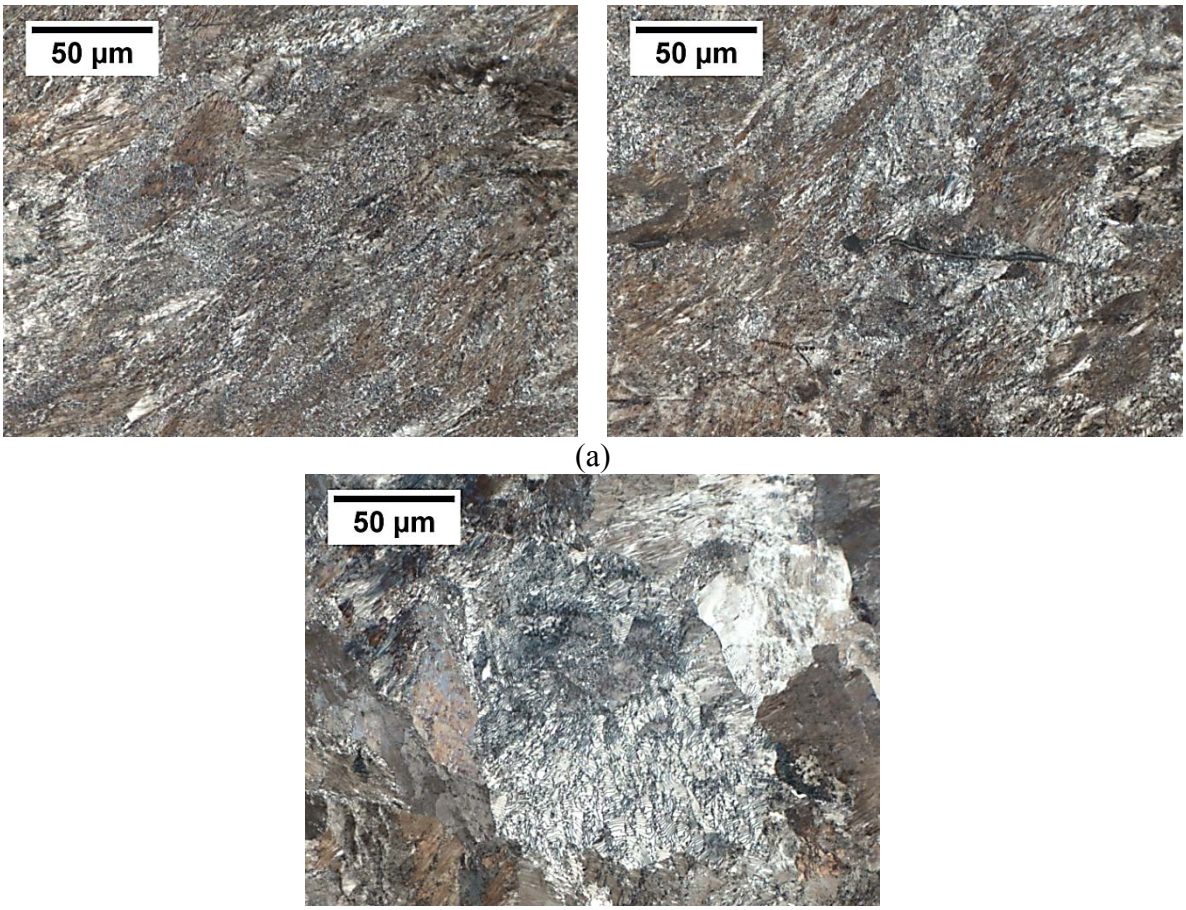

Figure 2.31 (a) Mildly deformed region (region II) (b) Undeformed region (region III) at higher magnification (Etched Rail 1-LT).

Etched **Rail 1-TG** specimen showed that the mid-gauge region had structure similar to the largely deformed region (in Rail 1-LT specimen) and a layer-like structure could be observed in the middle of the zone close to the rail running surface (Figure 2.32a). The rail gauge region of 1-TG specimen could be divided into three (3) zones (Figure 2.33). In the upper gauge zone (zone 1), pearlitic structure experienced mild plastic deformation (Figure 2.34a). A thin plastically deformed layer (Figure 2.34b) was seen at surface of the middle zone (zone 2). At the lower gauge zone (zone 3), the pearlite colonies aligned to the surface as a result of plastic deformation (Figure 2.34c).

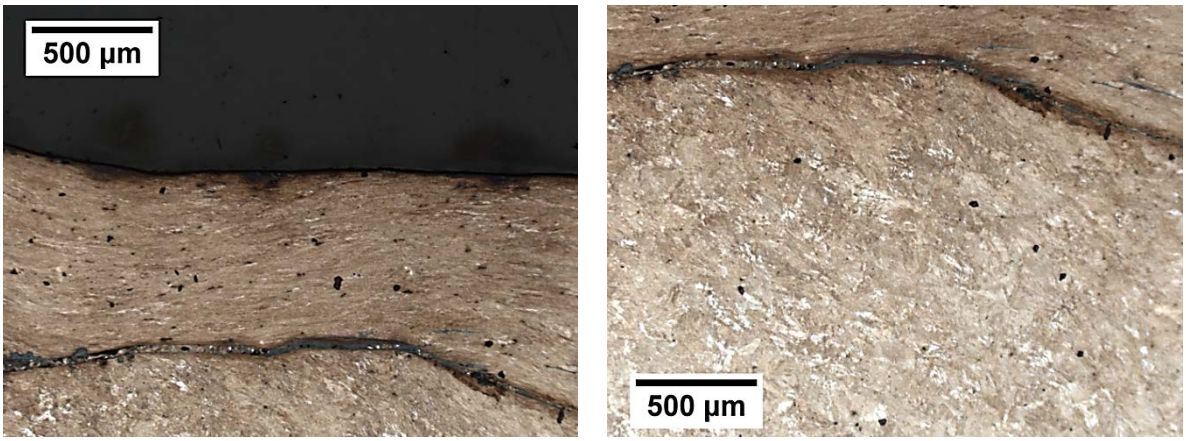

(a) (b)

Figure 2.32 (a) Layer-like structure (b) Deformed pearlite colonies in the mid-gauge region of Rail 1 (Etched Rail 1-TG).

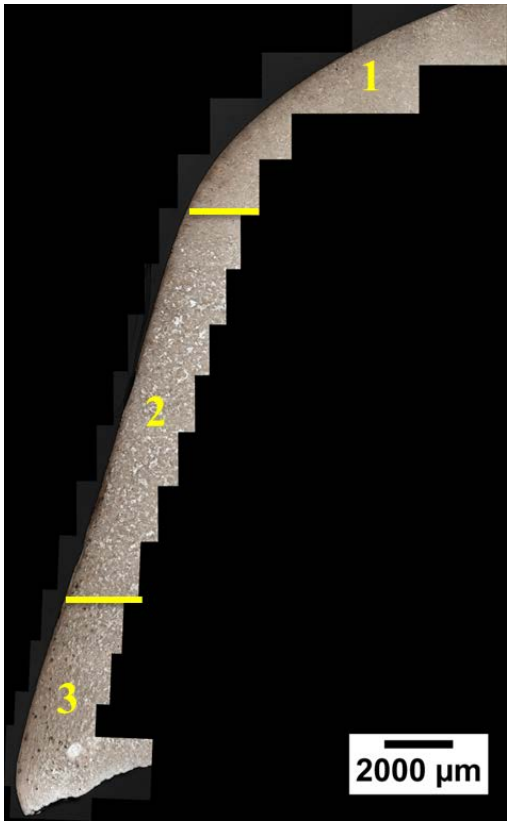

Figure 2.33 Location of (1) Upper gauge zone (2) Middle Gauge zone (3) Lower gauge zone at the gauge region of Rail 1 (Etched Rail 1-TG).

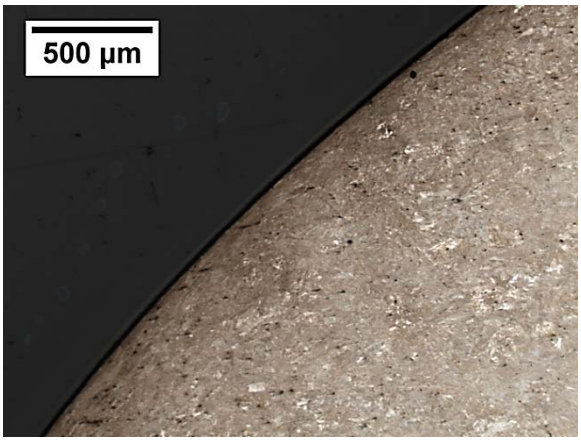

(a)

(b)

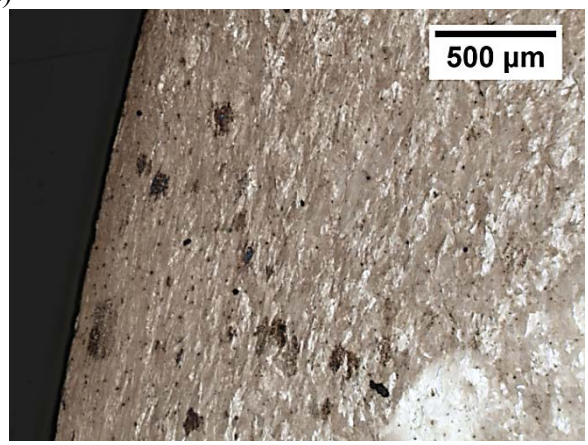

(c)

Figure 2.34 Plastic deformation at (a) Upper gauge zone (zone 1) (b) Middle gauge zone (zone 2) (c) Lower gauge zone (zone 3) (Etched Rail 1-TG).

Rail 2: Similar to Rail 1-LT specimen, etched **Rail 2-LT** specimen consisted of three (3) regions. From the rail running surface to a depth of 2598 µm there was a largely deformed region (Figure 2.35a) followed by a mildly deformed region up to depth of 4857 µm (Figure 2.35b). The layer-like structure was observed again and pearlite colonies were deformed similarly as in Rail 1-LT specimen. Etched **Rail 2-TG** specimen revealed that the microstructure in the mid-gauge region was largely deformed and exhibited a layer-like structure in the middle (close to the surface) (Figure 2.36a). However, the size of the layer-like structure was smaller in comparison to Rail 1. Four (4) zones could be identified at the gauge region of Rail 2-TG specimen. There was a mildly deformed zone (Figure 2.37a) at the top of gauge region followed by a small zone

which had a thick plastically deformed layer (Figure 2.37b). Similar to Rail 1, a thin surface layer had experienced plastic deformation in the middle of gauge region (Figure 2.37c). The lower gauge zone experienced large plastic deformation which had resulted in alignment of pearlite colonies to the surface (Figure 2.37d) and formation of a plastic flow lip. The layer-like structure could be seen at the plastic flow lip and adjacent area.

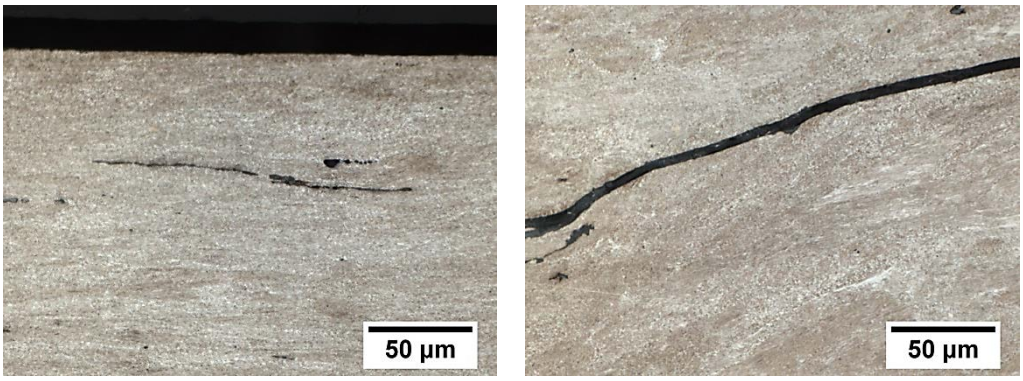

(a)

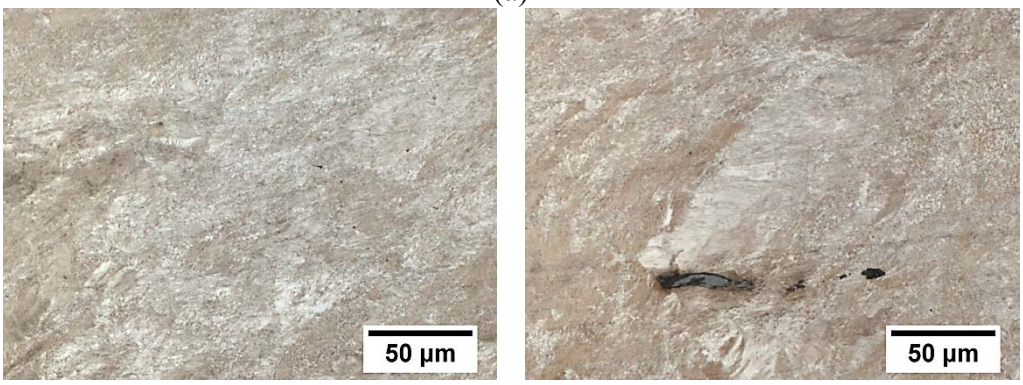

(b)

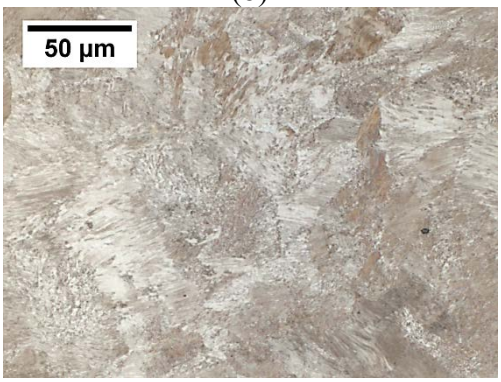

(c)

Figure 2.35 (a) Largely deformed region (b) Mildly deform region (c) undeformed region (Etched Rail 2-LT).

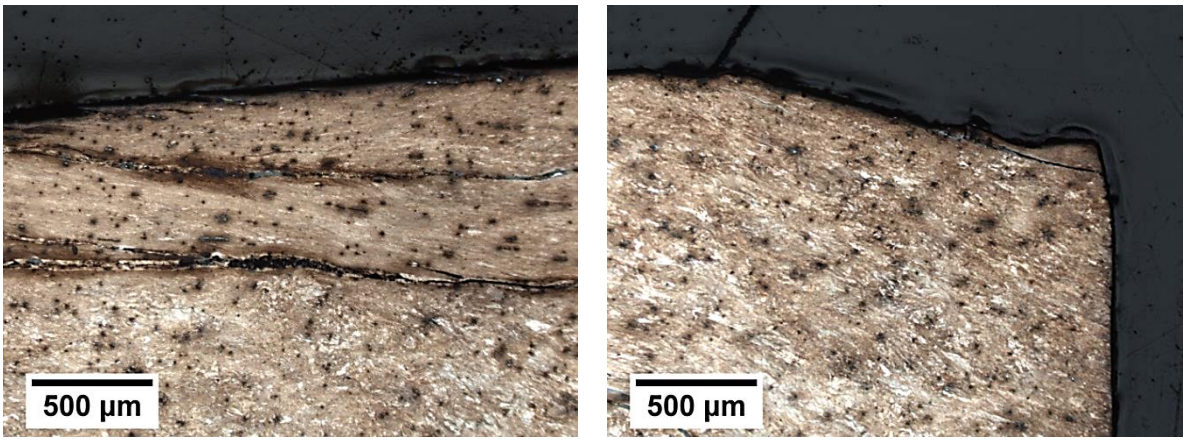

(a) (b)

Figure 2.36 (a) Layer-like structure (b) deformed pearlite colonies in the mid-gauge of Rail 2 (Etched Rail 2-TG).

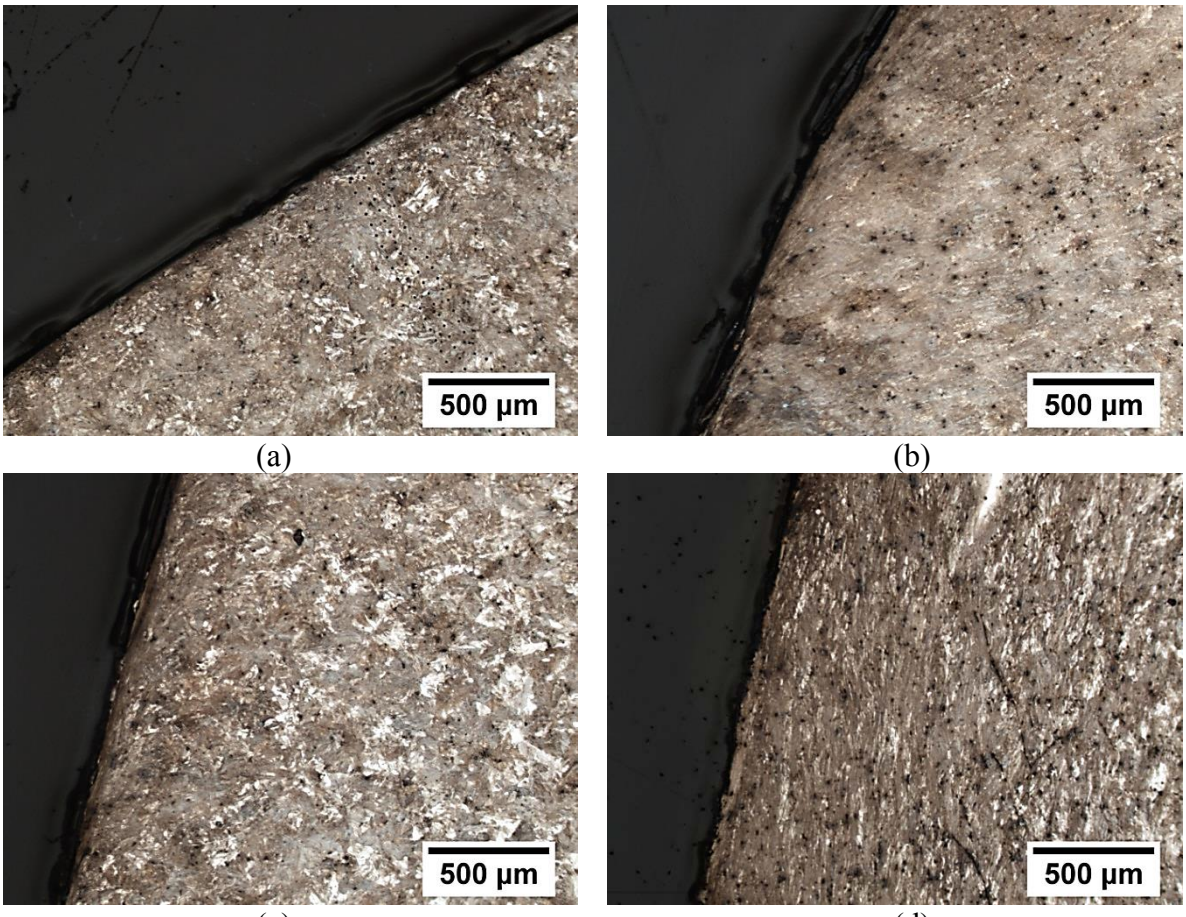

(a) (b)

(c) (d)

Figure 2.37 Plastic deformation at (a) Upper gauge zone (b) Intermediate zone (c) Middle gauge zone (d) Lower gauge zone (Etched Rail 2-TG).

Rail 7: For etched **Rail 7-LT** specimen, the depth of largely deformed region was 3030 µm from the surface (Figure 2.38a). Then, to a depth of 4831 µm there was a mildly deformed region (Figure 2.38b). The deformation features of this specimen were similar to Rail 1-LT and 2-LT specimens.

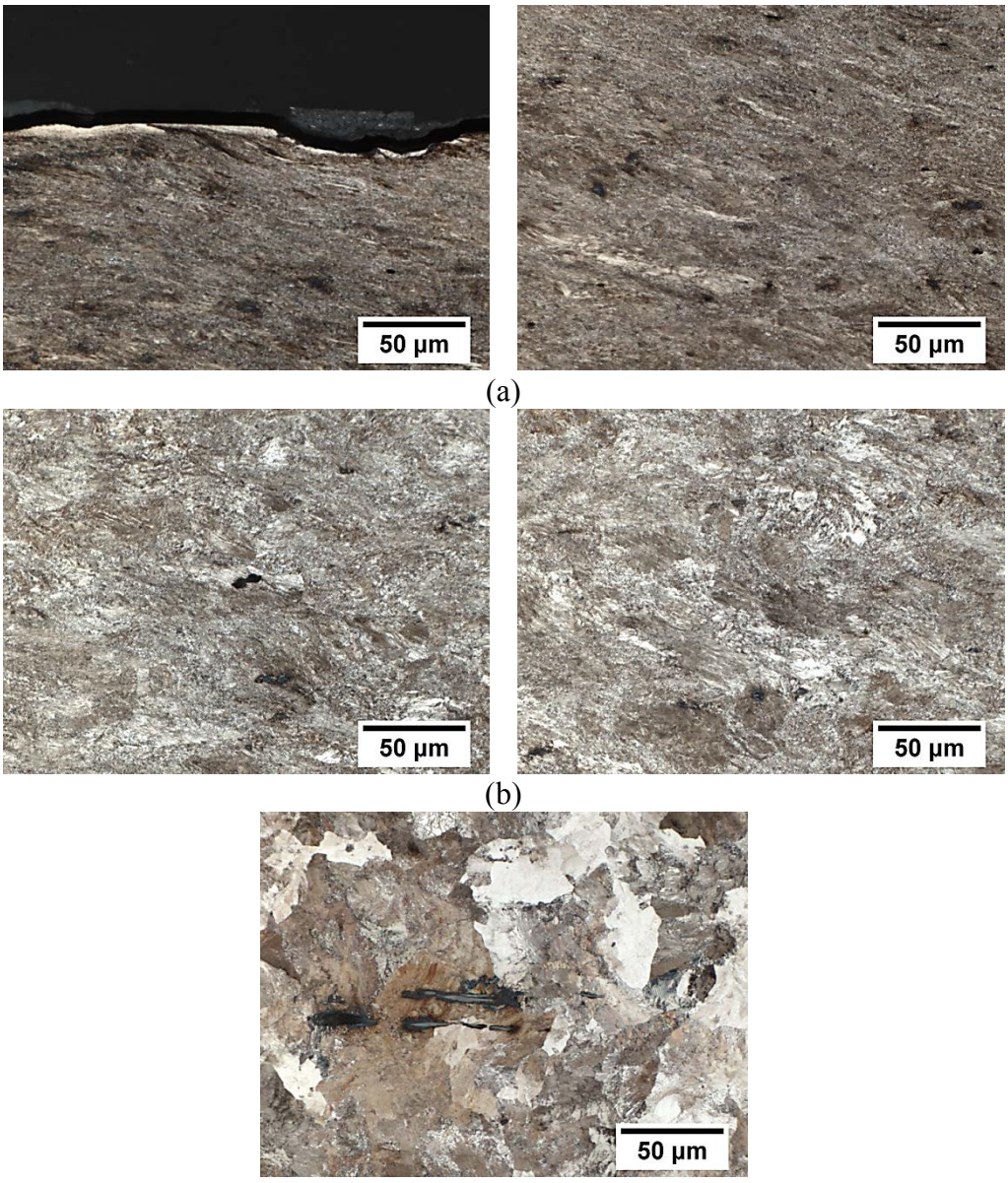

Figure 2.38 (a) Largely deformed region (b) Mildly deform region (c) undeformed region (Etched Rail 7-LT).

Etched **Rail 7-TG** specimen showed that the mid-gauge and gauge corner regions had been largely deformed and a thin layer-like structure could be observed in the area close to the rail running surface throughout the region (Figure 2.39a). The gauge region could be divided into two (2) zones. The upper zone (from top to the middle of the gauge region) had experienced significant plastic deformation up to few millimeters (Figure 240a). In the lower zone, as a result of plastic deformation, the pearlite colonies had been aligned to the rail running surface (Figure 2.40b) and a small plastic flow lip had formed. Unlike the two previous rails, there was no zone with a thin plastically deformed layer in the middle of the gauge region.

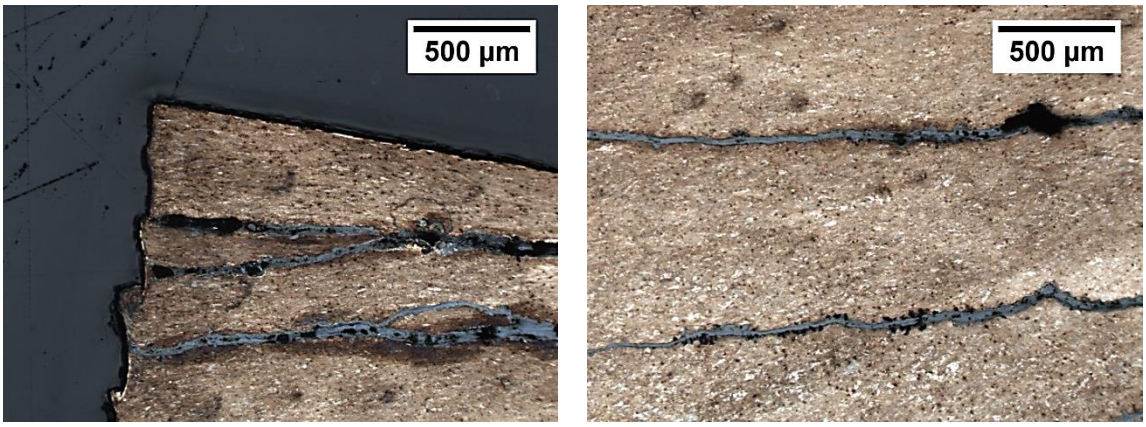

(a) (b)

Figure 2.39 (a) Layer-like structure (b) Deformed pearlite colonies in the mid-gauge of Rail 7 (Etched Rail 7-TG).

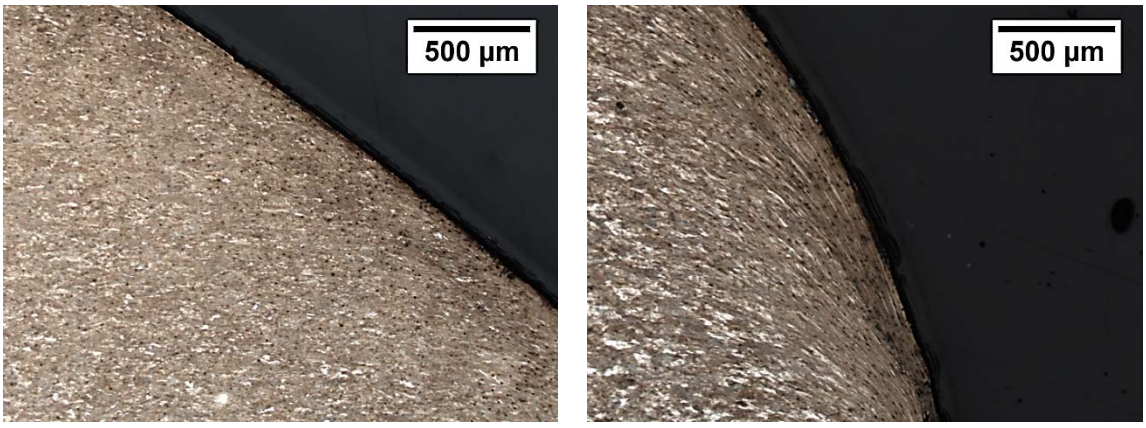

(a) (b)

Figure 2.40 Plastic deformation at (a) Upper gauge zone (b) Lower gauge zone (Etched Rail 7-TG).

From etched LT specimens (Rail 1, 2 and 7), it could be seen that depths of largely deformed regions were close to each other (2505 µm in Rail 1, 2598 µm in Rail 2 and 3030 µm in Rail 7). This was also true for the depths of mildly deformed regions (4788 µm in Rail 1, 4857 µm in Rail 2 and 4831 µm in Rail 7). It is interesting that the rails had been deformed to almost the same extent despite having different life cycle times. Moreover, comparing the maximum depths of cracks in LT samples (2219 µm in Rail 1, 2409 µm in Rail 2 and 2863 µm in Rail 7) with the depths of largely deformed regions showed that the cracks had propagated up to the boundary of the largely deformed regions. This observation was in agreement with the "***layered damage mechanism***" proposed by Donzella *et al.* (2011). Based on this mechanism, in the surface layer (called largely deformed region in the current study) shear strains were larger than the critical value which resulted in "shear band cracking". In the second layer (mildly deformed region), shear strains were smaller than the critical value and ratchetting took place. Below the second layer there was no plastic flow and shakedown behavior was dominant.

Moreover, it could be observed that the cracks follow the ***plastic deformation lines***. As mentioned previously, it has been reported that initiation and early propagation of cracks occur along pro-austenite grain boundaries, especially if there is PE ferrite at the grain boundaries. The reason is that during cyclic loading, PE ferrite strain hardens more than pearlite resulting in preferential straining in the PE ferrite (Garnham & Davis 2008; Garnham & Davis 2011). The rail microstructure can contain PE ferrite as a result of heat treatment process or decarburization during hot rolling (Carrol & Beynon 2006; Steenbergen 2017). However, there were no traces of PE ferrite in the running surfaces of examined rails. It is possible that the decarburized layer had been removed by preventive/corrective grinding during service. Also, it has been suggested that

a strong increase in defects density as a result of shear-compressive strains may reduce the amount of PE ferrite (Dylewski *et al.* 2016).

In the absence of PE ferrite, another explanation for the dependence of crack path on microstructure should be provided. Hohenwarter *et al.* (2010) studied the effect of pre-deformation and crack plane orientations on the fracture toughness of a fully pearlitic steel using high-pressure torsion (HPT). Their findings show that the deformation-induced alignment of pearlite colonies results in an anisotropic fracture behavior. The crack propagation direction that is parallel to cementite lamellae has the lowest fracture toughness which justifies why the cracks were aligned to the plastic deformation lines. In another study, Larijani *et al.* (2013) developed a numerical model to evaluate the effect of anisotropic layer on the propagation of cracks in rail heads. Their results show that anisotropy of the surface layer affects the crack propagation direction. A highly anisotropic surface layer results in downward propagation of the cracks while in a more isotropic one the cracks will propagate toward the surface. In addition, the thickness of the anisotropic surface layer influences the crack propagation rate; the larger the thickness, the higher the propagation rate.

Rail 10: Etched **Rail 10-LT** specimen had also three (3) regions, but the thicknesses of the regions were reduced in comparison to the previous rails. From the rail running surface to a depth of about 695 μm there was a largely deformed (Figure 2.41a) region and between 695 and 1420 μm there was a mildly deformed region (Figure 2.41b). Examining the area close to the rail running surface at higher magnification (500x) revealed that the layer-like structure was thin and titled pearlite colonies were dominant. Etched **Rail 10-TG** specimen exhibited mildly deformed mid-gauge and gauge corner regions (Figure 2.42). Similar to Rail 2, there were four (4) zones at the gauge region. At the top of gauge region, there were no traces of plastic deformation (Figure

2.43a). Then, there was a small zone which had been significantly deformed up to a few millimeters (Figure 2.43b). Similar to Rails 1 and 2, a thin plastically deformed layer could be observed at the surface of the middle of gauge region (Figure 2.43c). Severe plastic deformation of the lower gauge zone had created a plastic flow lip with a dominant layer-like structure (Figure 2.43d).

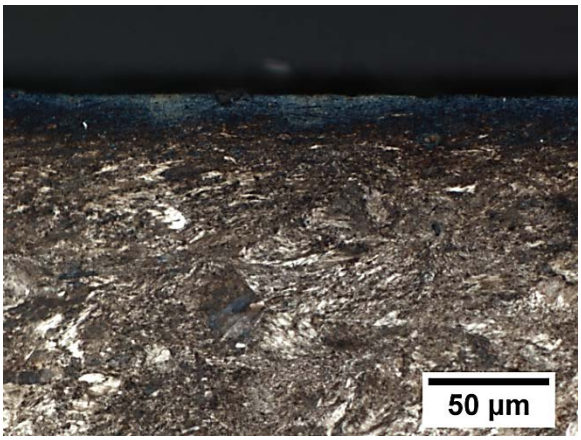

(a)

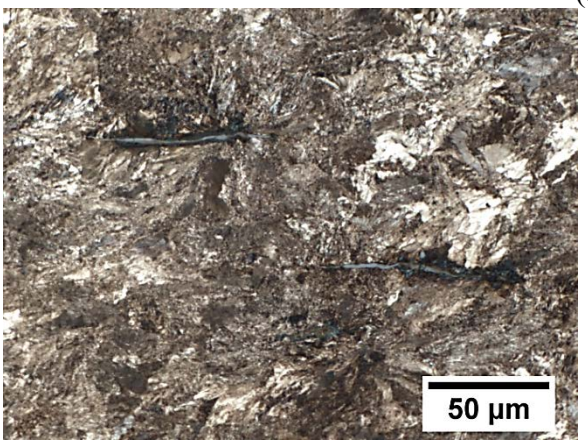

(b)

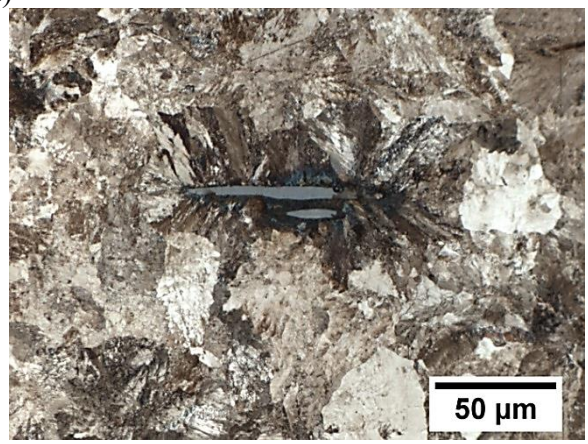

(c)

Figure 2.41 (a) Largely deformed region (b) Mildly deformed region (c) Undeformed region (Etched Rail 10-LT).

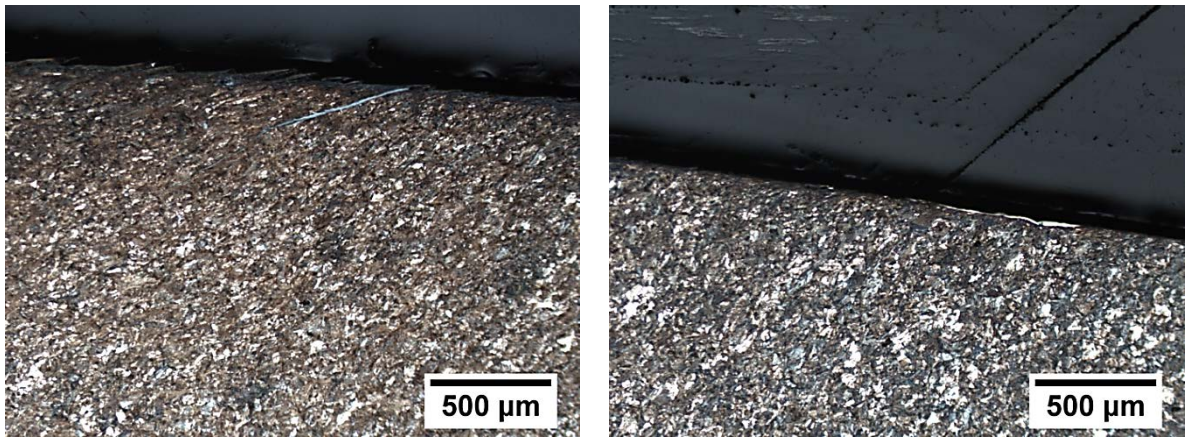

Figure 2.42 Plastic deformation in the mid-gauge and gauge corner regions of Rail 10 (Etched Rail 10-TG).

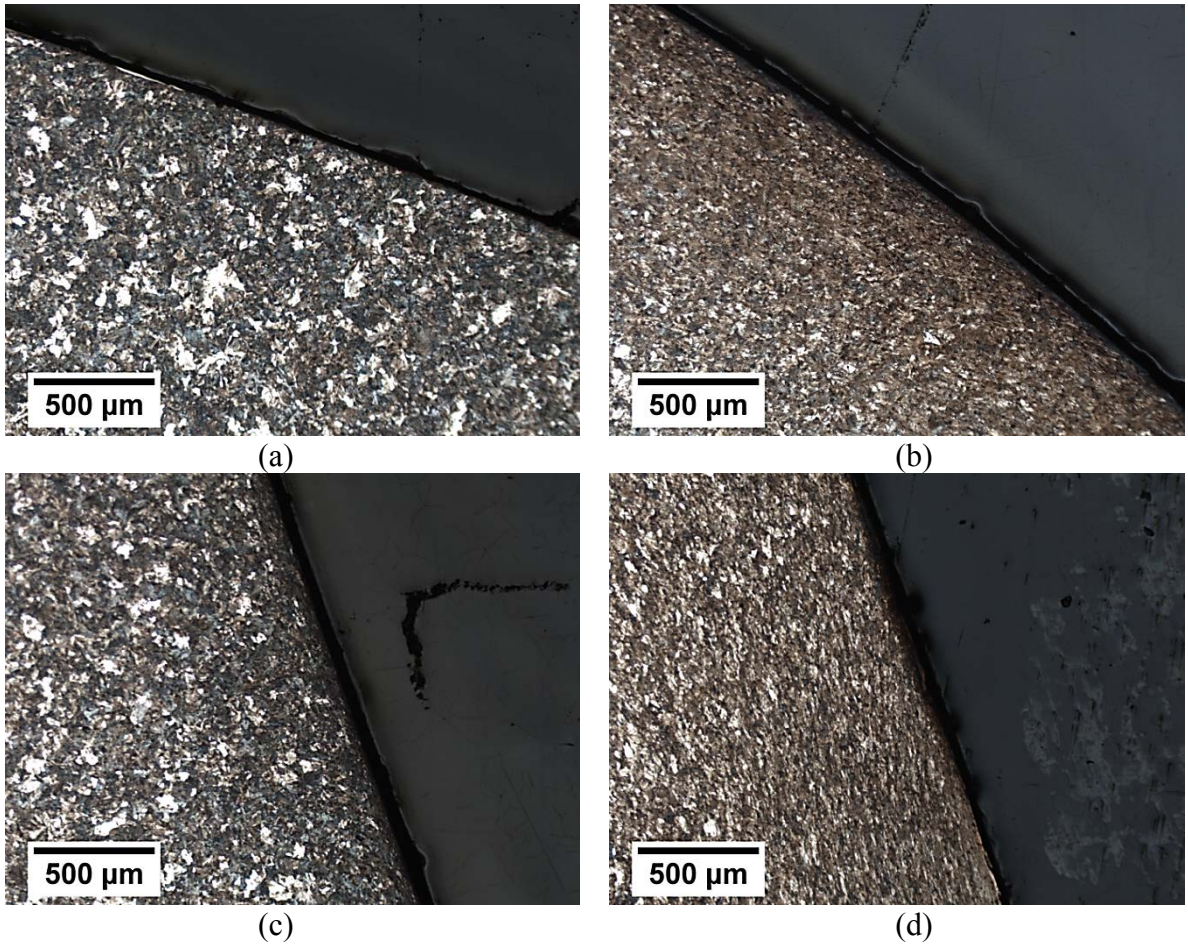

(a) (b)

(c) (d)

Figure 2.43 Plastic deformation at (a) Upper gauge zone (b) Intermediate zone (c) Middle gauge zone (d) Lower gauge zone (Etched Rail 10-TG).

Rail 12: the plastic deformation characteristics of etched **Rail 12-LT** and Rail 10-LT specimens were very similar to each other. The largely deformed region of Rail 12-LT (Figure 2.44a) had a depth of 803 µm, followed by mildly deformed region (Figure 2.44b) to a depth of 1576 µm. Also, the mid-gauge and gauge corner regions of etched **Rail 12-TG** specimen (Figure 2.45) had microstructures similar to the corresponding regions from Rail 10-TG. The gauge region of Rail 12-TG specimen consisted of three (3) zones. The upper gauge zone (Figure 2.46a) experienced significant plastic deformation up to a few millimeters while the middle zone (Figure 2.46b) consisted of a thin plastically deformed layer. Aligned pearlite colonies and a small plastic flow lip were observed at the lower gauge zone (Figure 2.46c).

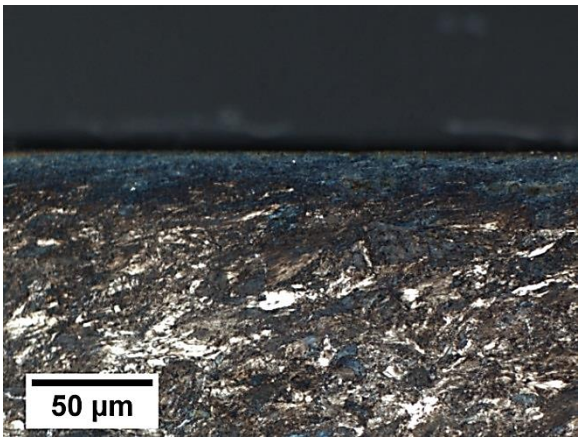

(a)

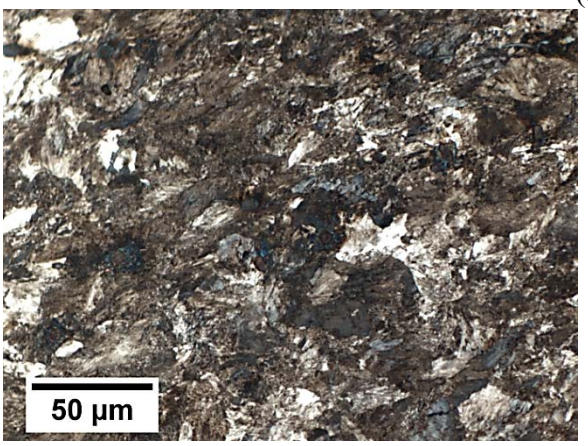

(b)

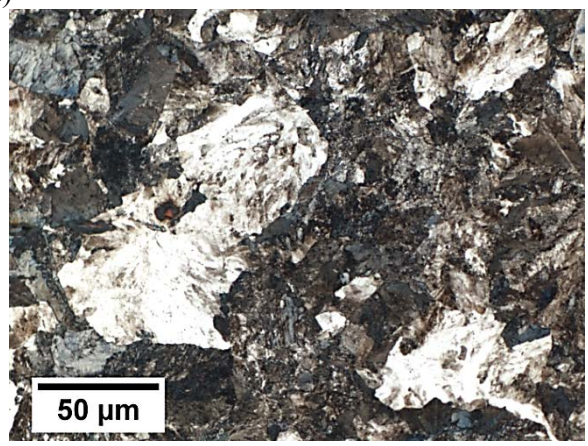

(c)

Figure 2.44 (a) Largely deformed region (b) Mildly deformed region (c) Undeformed region (Etched Rail 12-LT).

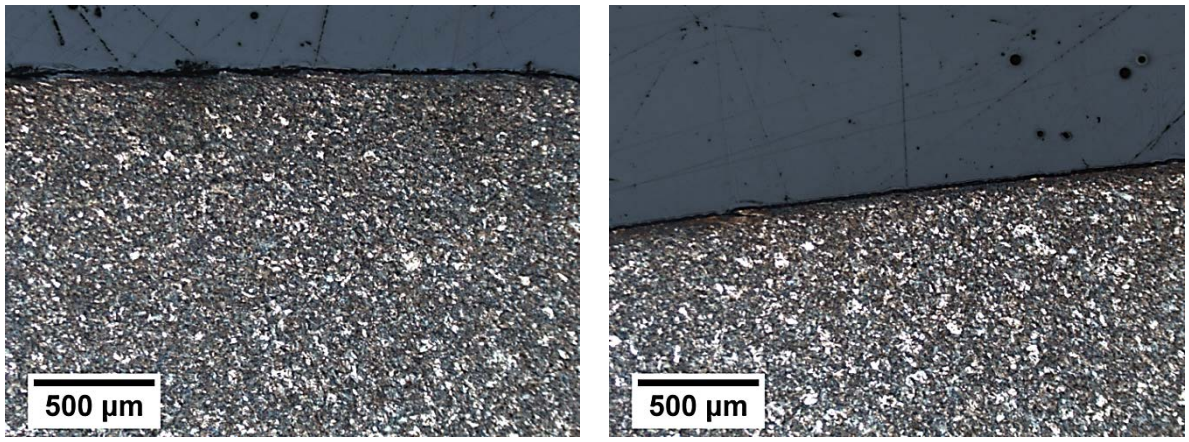

Figure 2.45 Plastic deformation in the mid-gauge and gauge corner regions of Rail 12 (Etched Rail 12-TG).

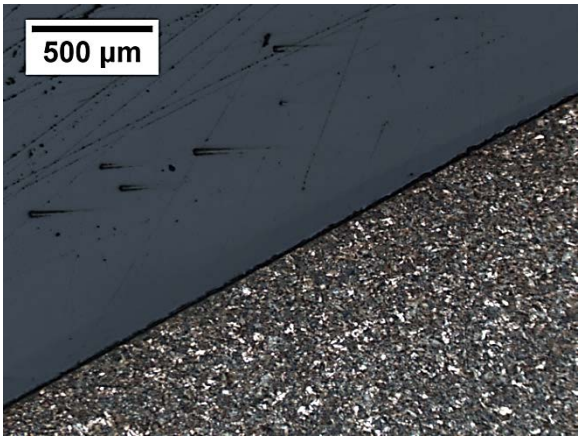

(a)

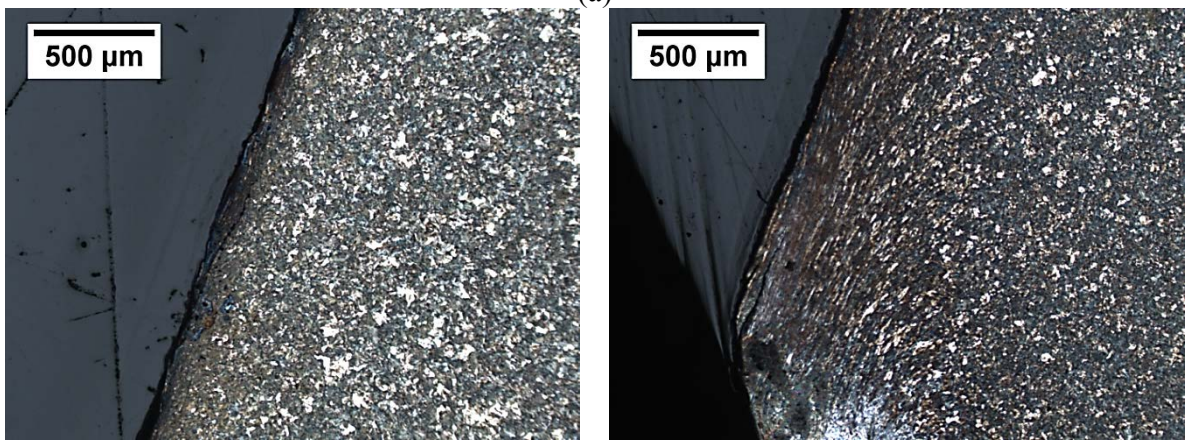

(b) (c)

Figure 2.46 Plastic deformation at (a) Upper gauge zone (b) Middle gauge zone (c) Lower gauge zone (Etched Rail 12-TG).

It could be seen that the depths of largely deformed regions (695 and 803 μm) and mildly deformed regions (1420 and 1576 μm) of Rail 10-LT and Rail 12-LT specimens were close to each other. The maximum depths of cracks in these specimens (661 μm in Rail 10 and 610 μm in Rail 12) were almost the same as the depths of largely deformed regions. Comparing these numbers with the corresponding ones for the LT specimens of the first three rails, it appeared that under the same traffic, the thickness of these layers were mainly influenced by the grade of rail steels rather than the length of service life. Donzella *et al.* (2011) have also observed that the crack depth and surface layer thickness were almost independent from cycle numbers (after damage appearance) and proposed the "***steady state shear band crack propagation***" mechanism. Based on this mechanism, the radial size of the damage process zone presented at the surface layer is almost constant. When a part of the surface layer is removed by wear, critical strain is reached in (part of) the second layer. As a result, a "stabilized growing" condition is presented at the crack tip.

The gauge regions of all rail samples except Rail 7 exhibited three (3) distinct zones with respect to plastic deformation. The difference between plastic deformation characteristics of the zones can be explained by the difference in the loading modes (normal vs. shear loads). At the upper gauge zone, the normal loads are high in compare to the shear loads. It is known that normal loads reach deeper into the rail than shear loads (Schilke *et al.* 2013). As a result, thick plastically deformed layers had developed at the upper gauge zones. In the middle gauge zone, the normal loads are low and the shear loads are high. Therefore, the middle gauge zones consisted of thin plastically deformed layers. Severe shear loads at the lower gauge zones had aligned the pearlite colonies to the rail running surface and created plastic flow lips.

2.2.2.2. MnS based inclusions

As mentioned before, brittle inclusions are rarely found in rail steels that have been manufactured since 1970's. However, rail steels still have ductile inclusions which are mainly MnS based inclusions. For the examined rails, characteristics of the MnS based inclusions including their shapes and distributions were evaluated qualitatively.

Rail 1: Examination of **Rail 1-TG** specimen revealed that in the upper zone of the rail gauge region, most of the inclusions had circular or elliptical shape. Besides, a few needle-like inclusions could be observed in this zone (Figure 2.47a). There were no traces of needle-like inclusions in the middle gauge zone and all of the inclusions were circular or elliptical (Figure 2.47b). In the lower gauge zone, the inclusions were mostly circular or elliptical along with several needle-like inclusions in the area close to the plastic flow lip (Figure 2.47c). At the mid-gauge region of the Rail 1-TG specimen, numerous needle-like inclusions were observed in the zone near the rail running surface (Figure 2.48a). Below this zone, circular or elliptical inclusions were dominant and only a few needle-like inclusions could be seen (Figure 2.48b). The **Rail 1-TT** specimen showed that the top of rail region was similar to the mid-gauge region in terms of shape and distribution of inclusions (Figure 2.49). Evaluation of **Rail 1-LG** and **Rail 1-LT** specimens exhibited axially aligned inclusion stringers (Figure 2.50).

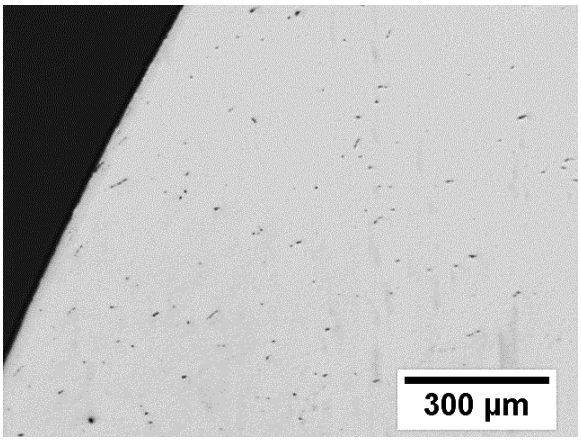

(a)

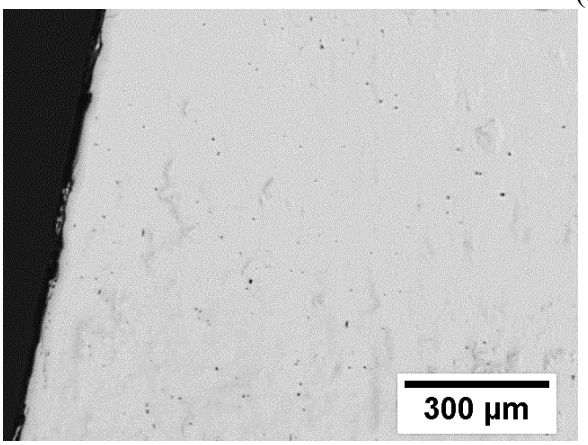

(b)

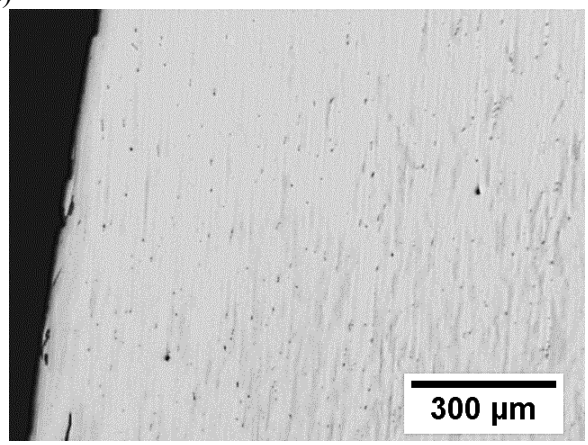

(c)

Figure 2.47 Inclusions in the (a) Upper gauge zone (b) Middle gauge zone (c) Lower gauge zone (Rail 1-TG).

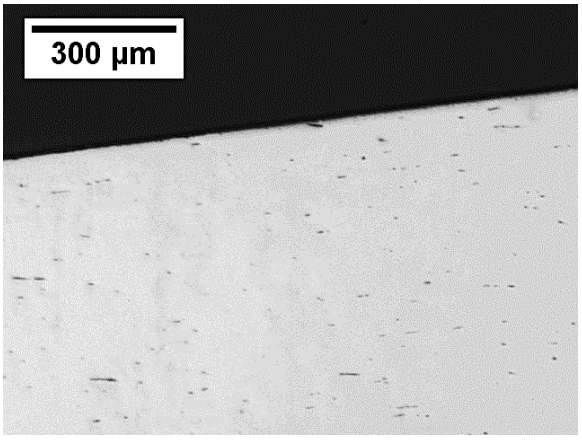

(a)

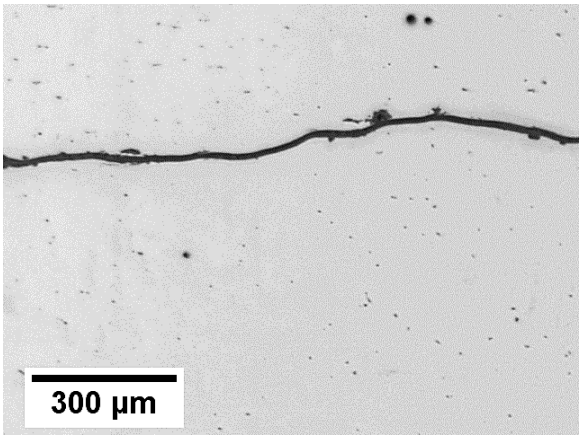

(b)

Figure 2.48 Inclusions in the mid-gauge region of Rail 1: (a) near-surface area (b) below the near surface area (Rail 1-TG).

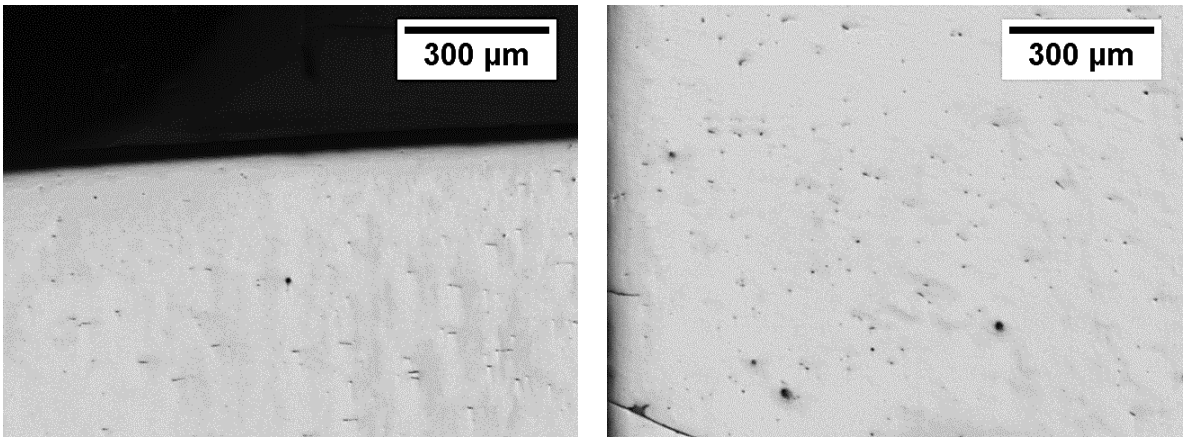

(a) (b)

Figure 2.49 Inclusions in the top of rail region of Rail 1 (a) near-surface area (b) below the near-surface area (Rail 1-TT).

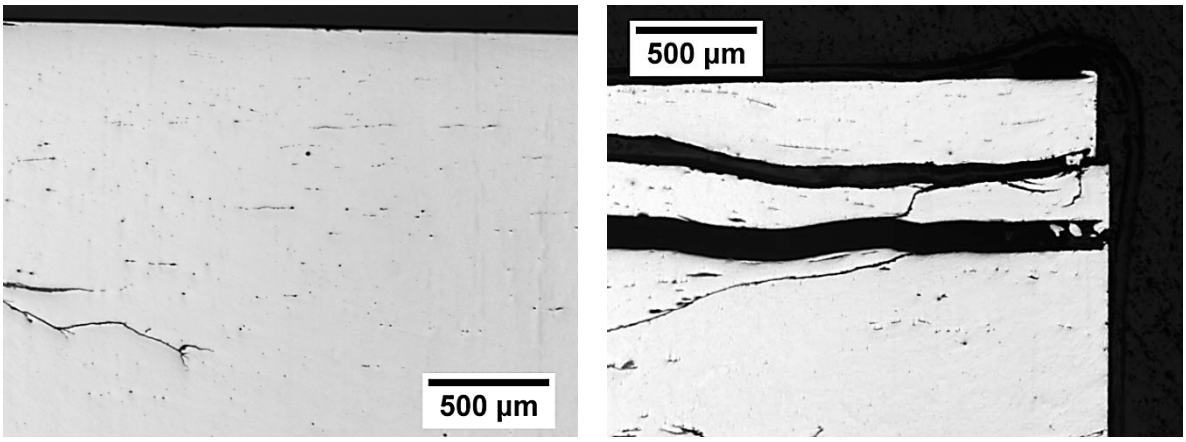

(a) (b)

Figure 2.50 Inclusion stringers in longitudinal section of the (a) gauge and (b) mid-gauge region of Rail 1 (Rail 1-LG and LT, respectively).

Rail 2: The inclusions in the upper and middle gauge zones of **Rail 2-TG** specimen were circular or elliptical with the exception of a few needle-like inclusions in the upper gauge zone (Figs 2.51a-b). In the lower gauge zone of Rail 2-TG specimen, many needle-like inclusions were observed near the plastic flow lip (Figure 2.51c). In the mid-gauge region, circular and elliptical inclusions were the dominant type (Figure 2.52). A number of needle-like inclusions could be seen mostly in the zone near the rail running surface (Figure 2.52a). **Rail 2-TT** showed

that shape and distribution of inclusions in the top of rail region were similar to the mid-gauge region (Figure 2.53). **Rail 2-LG** and **Rail 2-LT** specimens consisted of inclusion stringers which were axially aligned (Figure 2.54).

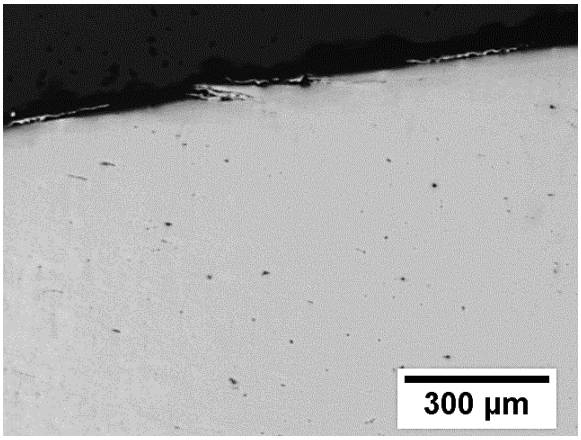

(a)

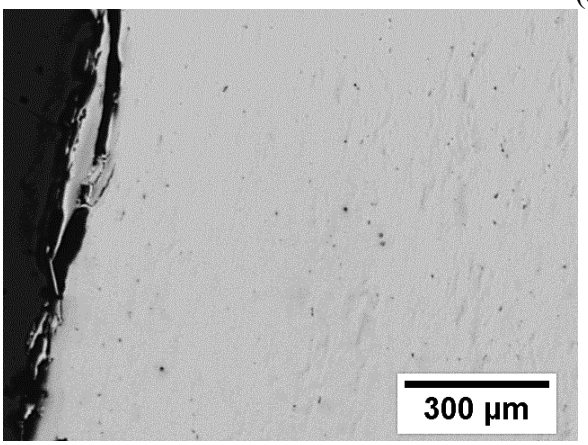

(b)

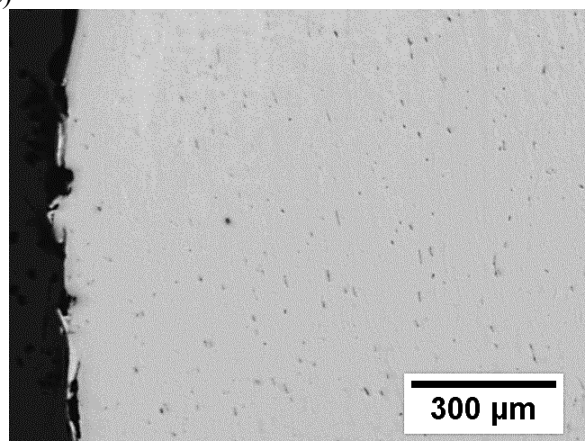

(c)

Figure 2.51 Inclusions in the (a) Upper gauge zone (b) Middle gauge zone (c) Lower gauge zone (Rail 2-TG).

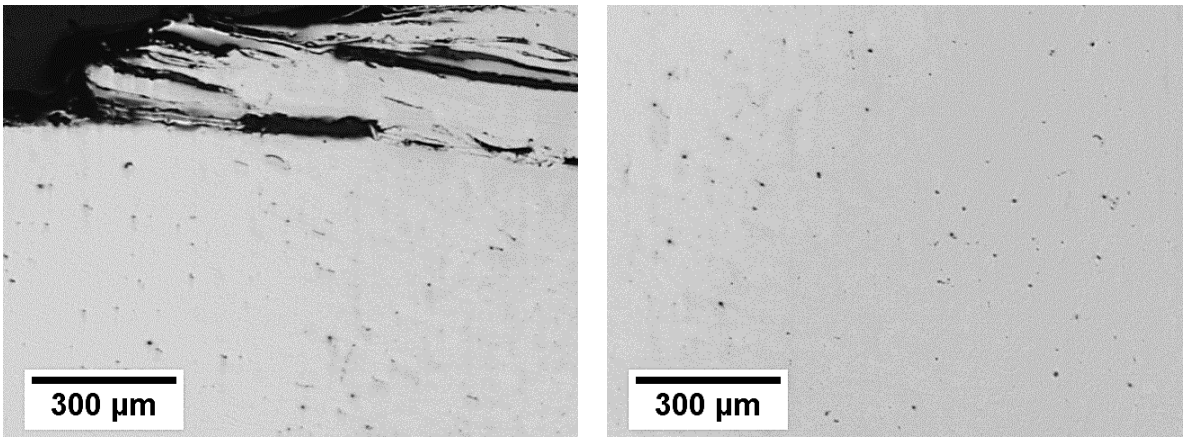

(a) (b)

Figure 2.52 Inclusions in the mid-gauge region of Rail 2: (a) near-surface area (b) below the near surface area (Rail 2-TG).

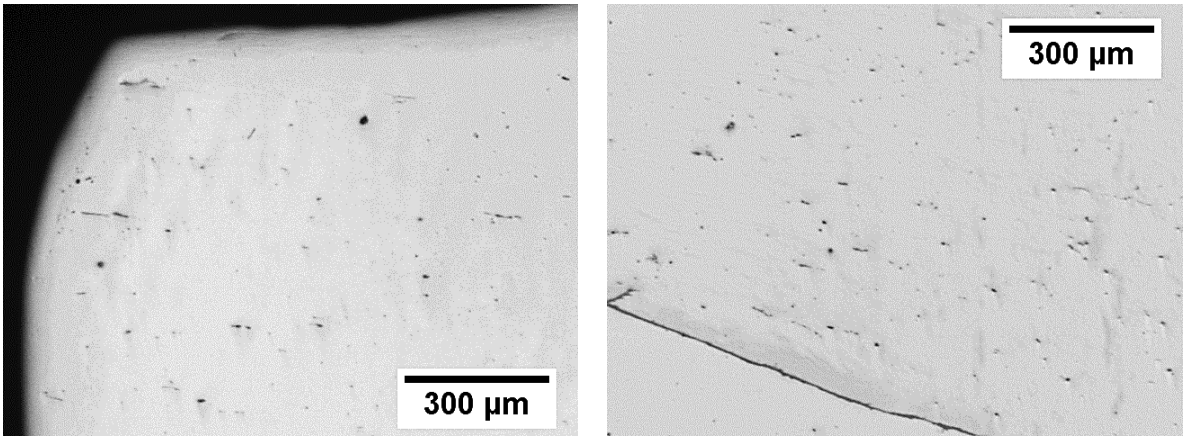

(a) (b)

Figure 2.53 Inclusions in the top of rail region of Rail 2 (a) near-surface area (b) below the near-surface area (Rail 2-TT).

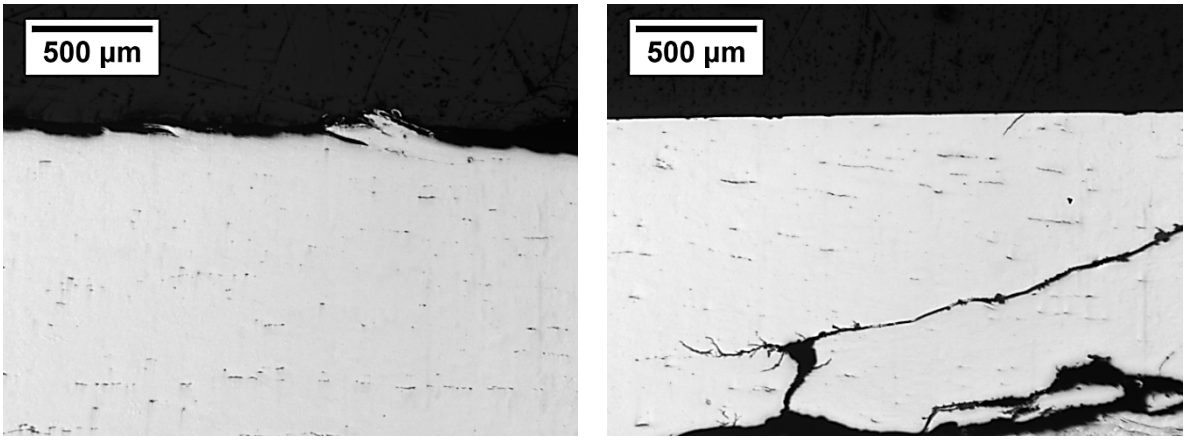

(a) (b)

Figure 2.54 Inclusion stringers in longitudinal section of the (a) gauge and (b) mid-gauge region of Rail 2 (Rail 2-LG and LT, respectively).

Rail 7: Evaluation of **Rail 7-TG** specimens showed that the inclusions in the upper gauge zone were predominantly circular or elliptical. In the lower gauge zone, several needle-like inclusions could be observed in a small area in the vicinity of the plastic flow lip and the rest of the zone contained circular or elliptical inclusions. The mid-gauge region of Rail 7-TG specimen and the top of rail region of **Rail 7-TT** specimen were covered by finely dispersed circular or elliptical inclusions and no needle-like inclusions could be traced in these regions (Figure 2.55). No axially aligned inclusion stringers were spotted in **Rail 7-LG** and **Rail 7-LT** specimens. Instead, circular or elliptical and many needle-like inclusions could be seen throughout the specimens (Figure 2.56).

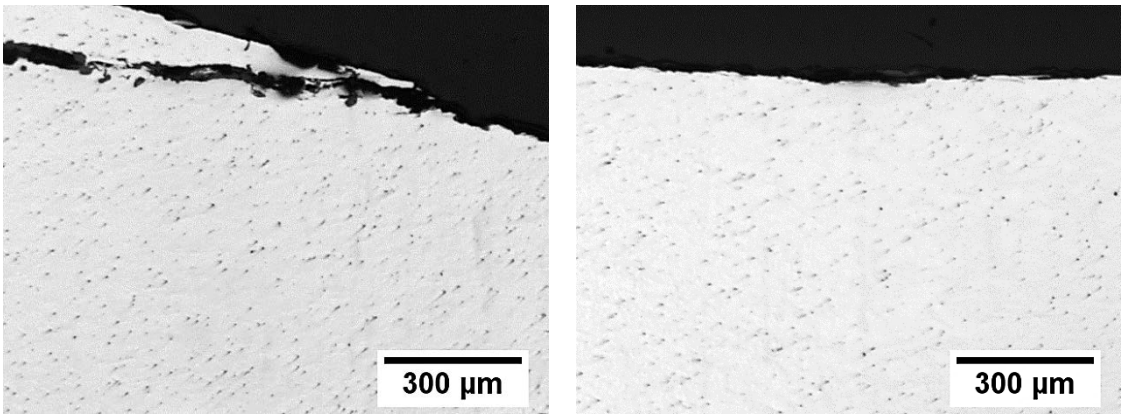

(a) (b)

Figure 2.55 Inclusion in the (a) mid-gauge (b) top of rail region of Rail 7 (Rail 7-TG and TT, respectively).

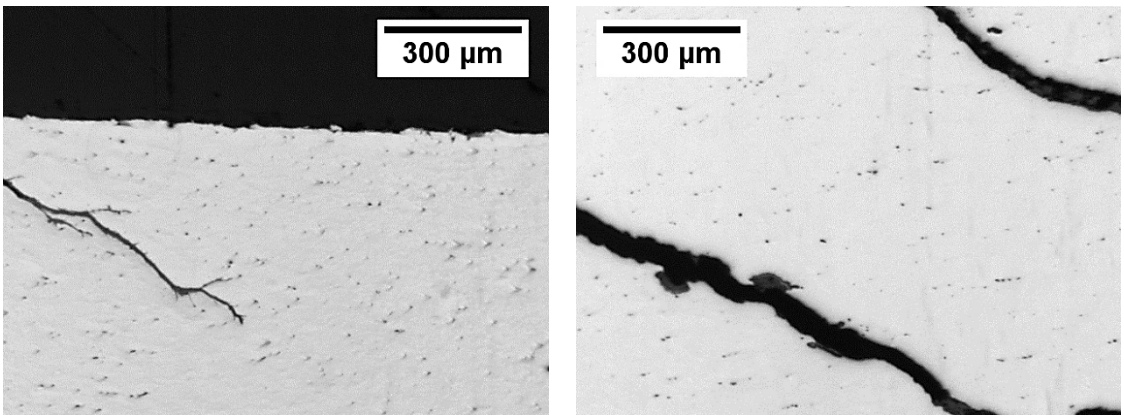

(a) (b)

Figure 2.56 Inclusion stringers in longitudinal section of the (a) gauge and (b) mid-gauge region of Rail 7 (Rail 7-LG and LT, respectively).

Rail 10: No traces of needle-like inclusion could be seen in the gauge region of **Rail 10-TG** specimen and all of the inclusions were circular or elliptical (Figure 2.57). Only a few needle-like inclusions were observed in the mid-gauge region of Rail 10-TG specimen and the top of rail region of **Rail 10-TT** specimen and circular or elliptical inclusions were the dominant type (Figure 2.58). **Rail 10-LG** and **Rail 10-LT** specimens contained axially aligned inclusion stringers (Figure 2.59).

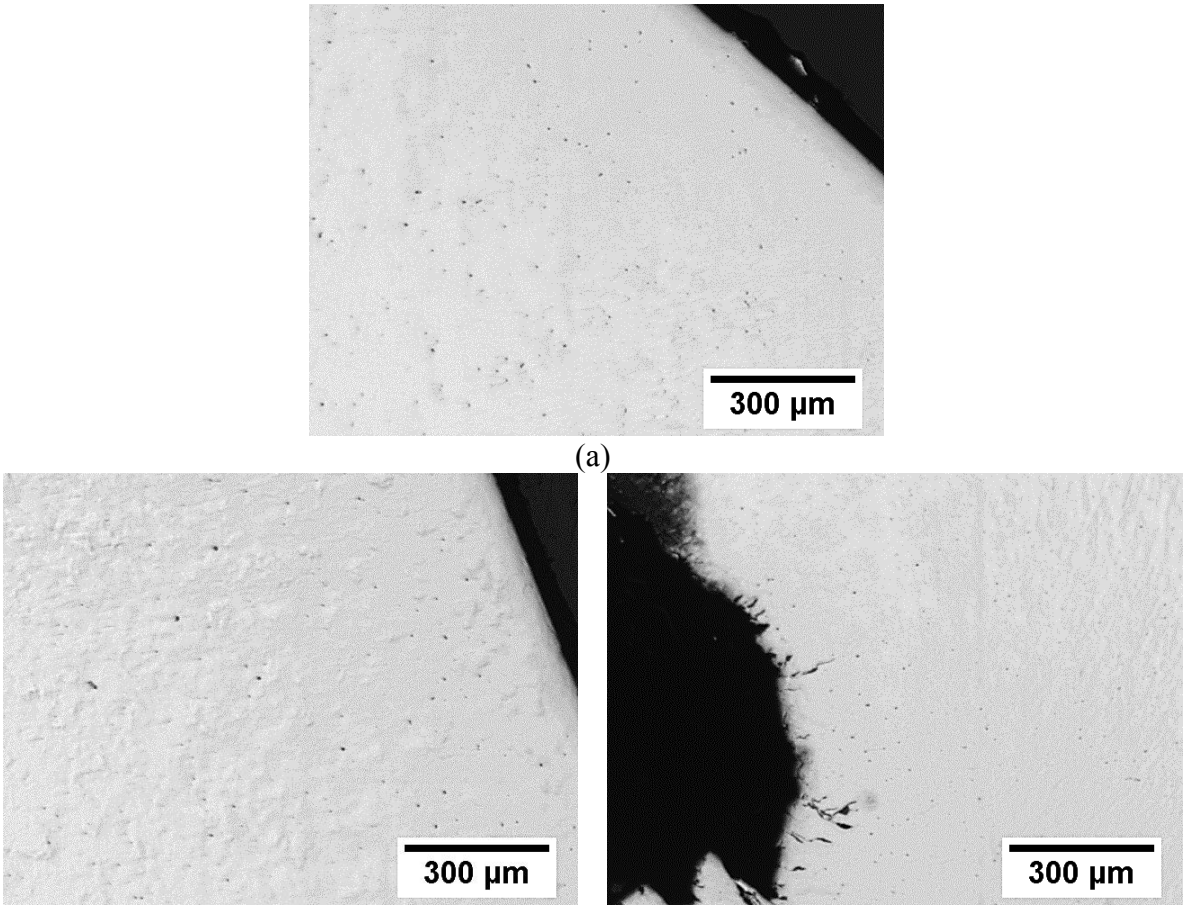

(a)

(b) (c)

Figure 2.57 Inclusions in the (a) Upper gauge zone (b) Middle gauge zone (c) Lower gauge zone (Rail 10-TG).

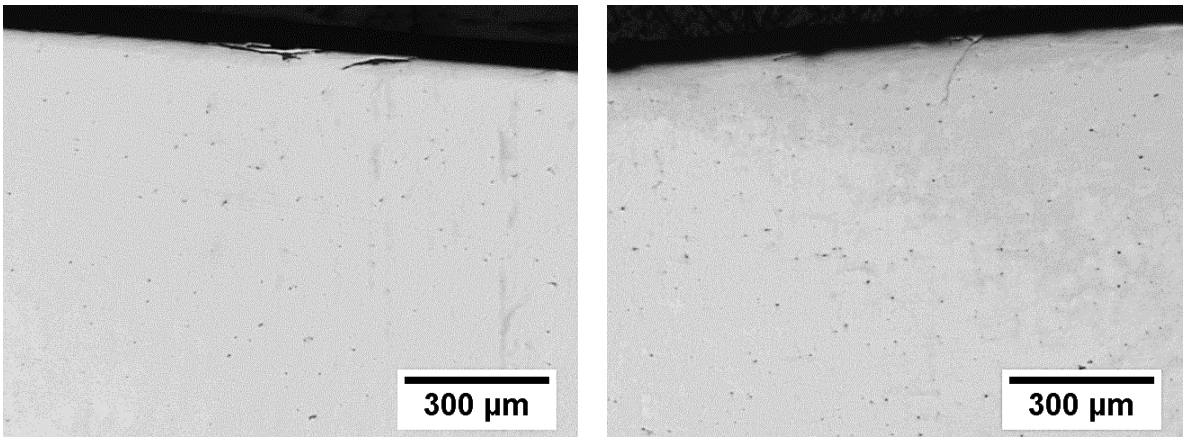

(a) (b)

Figure 2.58 Inclusion in the (a) mid-gauge (b) top of rail region of Rail 10 (Rail 10-TG and TT, respectively).

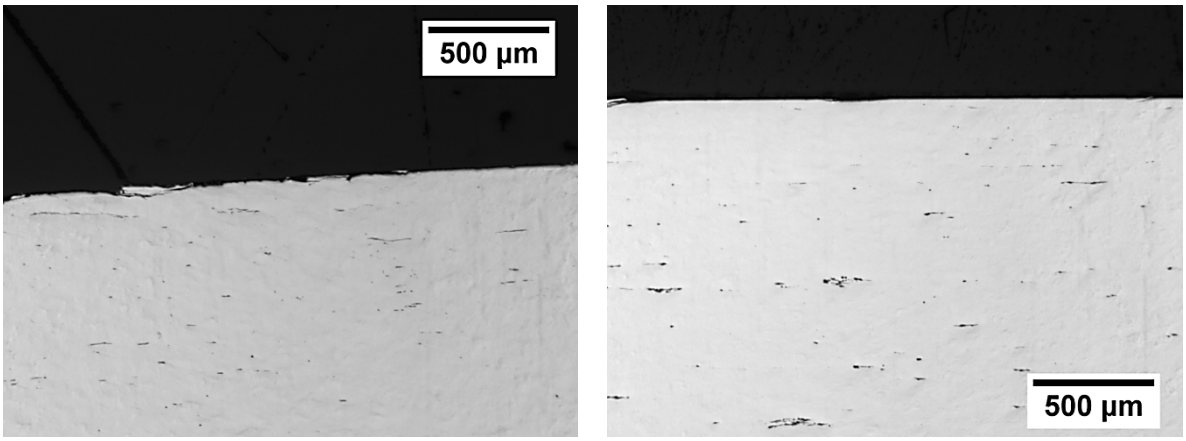

(a) (b)

Figure 2.59 Inclusion stringers in longitudinal section of the (a) gauge and (b) mid-gauge region of Rail 10 (Rail 10-LG and LT, respectively).

Rail 12: Circular or elliptical inclusions were the dominant types of inclusions in the gauge region of **Rail 12-TG** specimen and only a few needle-like inclusions could be seen in the lower gauge zone near the plastic flow lip (Figure 2.60). In the mid-gauge region of Rail 12-TG specimen and the top of rail region of **Rail 12-TT** specimen, inclusions were mostly circular and elliptical along with a few needle-like ones (Figure 2.61). Inclusion stringers, axially aligned, were observed in **Rail 12-LG** and **Rail 12-LT** specimens (Figure 2.62).

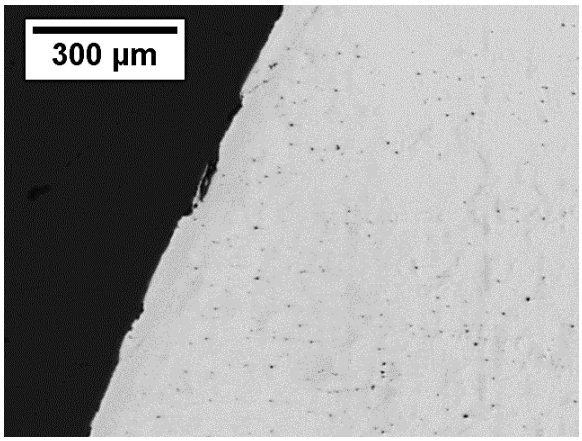

(a)

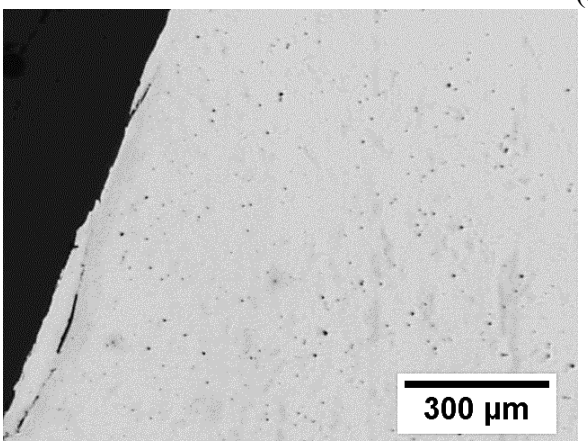

(b)

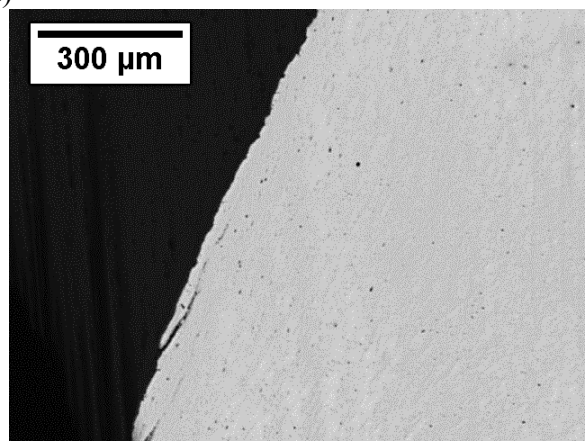

(c)

Figure 2.60 Inclusions in the (a) Upper gauge zone (b) Middle gauge zone (c) Lower gauge zone (Rail 12-TG).

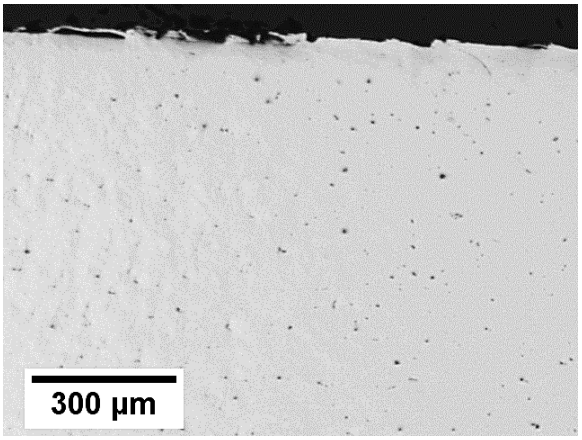

(a)

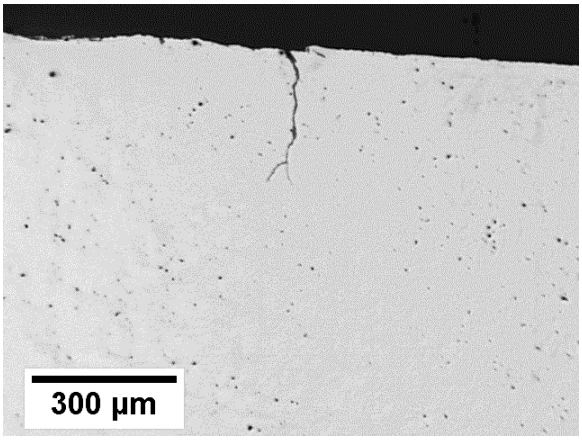

(b)

Figure 2.61 Inclusion in the (a) mid-gauge (b) top of rail region of Rail 12 (Rail 12-TG and TT, respectively).

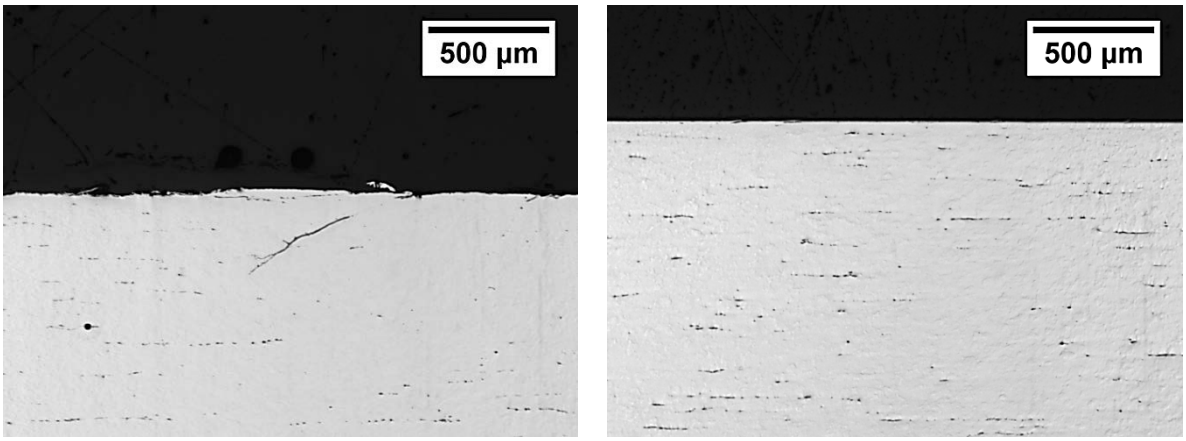

(a) (b)

Figure 2.62 Inclusion stringers in longitudinal section of the (a) gauge and (b) mid-gauge region of Rail 12 (Rail 12-LG and LT, respectively).

Comparing the results of inclusion analysis with the plastic deformation results revealed that the shape and distribution of the MnS based inclusions are correlated to the mode and severity of the loading. Examination of **TG specimens** revealed that at the upper gauge zones where the normal loads were high in compare to the shear loads, the inclusions were predominantly circular and elliptical. The shear loads became dominant in the middle gauge zones; however, they were not large enough to reach deep into the rails. It could be seen that all of the inclusions in the middle gauge zones were circular and elliptical and there were no traces of needle-like inclusions. At the lower gauge zones where the shear loads became large enough to cause significant material flow, several needle-likes inclusions were observed especially near the plastic flow lips. The lower gauge zone of Rail 10 was an exception; although it was severely deformed, no needle-like inclusions could be seen there.

In the mid-gauge regions, several needle-like inclusions were seen in the near-surface area with layer-like structure which was severely deformed as a result of high shear loads. Outside this area, inclusions were mostly circular and elliptical and only a few needle-like

inclusions could be observed. Evaluation of mid-gauge regions in the longitudinal direction (**LT specimens**) showed that the MnS based inclusion stringers in the area near the running surface were heavily deformed and flattened (Figure 2.63a). Away from the running surface, the inclusions were less elongated and more elliptical (Figure 2.63b).

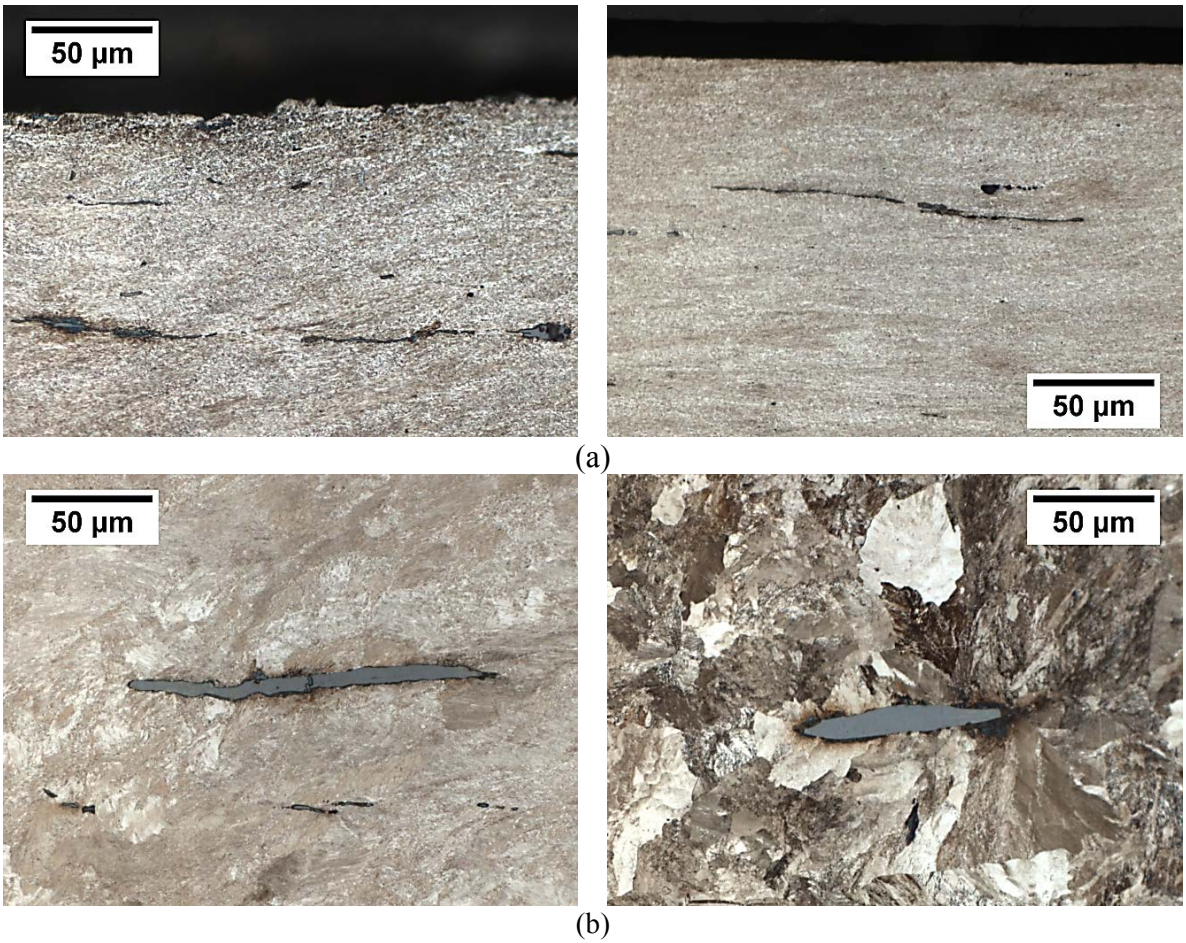

Figure 2.63 (a) Flattened MnS based inclusions in near-surface area (b) Undeformed inclusions.

These observations were in agreement with the study done by Garnham *et al.* (2010) on the deformation of ductile inclusions in rail steel under rolling contact loads. They observed that MnS based inclusions at the depths of used rail heads were in the form of axially aligned elongated ellipsoids and had circular or elliptical shapes in the transverse cross sections. As a

result of cyclic strain accumulation near the surfaces of the rail heads, these inclusions had become gradually flattened in axial and transverse directions, leading them to have a disc shape. These flattened MnS based inclusions act as planes of weakness and expedite RCF by facilitating initiation and propagation of cracks.

2.2.2.3. White etching layer (WEL)

During metallographic observations of the etched LT and TG specimens, presence of WELs on most of the specimens was noticed. Qualitative characteristics of the WELs and their correlation with initiation and propagation of the cracks were investigated.

Rail 1: Although the near-surface area of the etched **Rail 1-LT** specimen had experienced severe plastic deformation which made it susceptible to WEL formation (Carroll & Beynon 2007; Steenbergen & Dollevoet 2013), there were no traces of WEL in this specimen. Similarly, the mid-gauge and gauge corner regions of the etched **Rail 1-TG** specimen had a severely deformed near-surface area, without any indications of WEL. No WEL was observed at the surface of the upper gauge zone. The middle zone contained an almost continuous WEL throughout its surface (Figure 2.64a). Moreover, layers which had a dark brown color could be seen between the WEL and the deformed pearlite (Figure 2.64c). According to Carroll and Beynon (2007), this layer is pearlite with cementite lamellae that are on the verge of break up as a result of severe plastic deformation. It should be noted that this layer was not a ***"brown etching layer"*** which is a distinct featureless layer and has similar properties to WEL (Li *et al.* 2016; Messaadi & Steenbergen 2018). At lower gauge zone, almost half of the surface was covered with continuation of the WEL from the middle zone (Figure 2.64b).

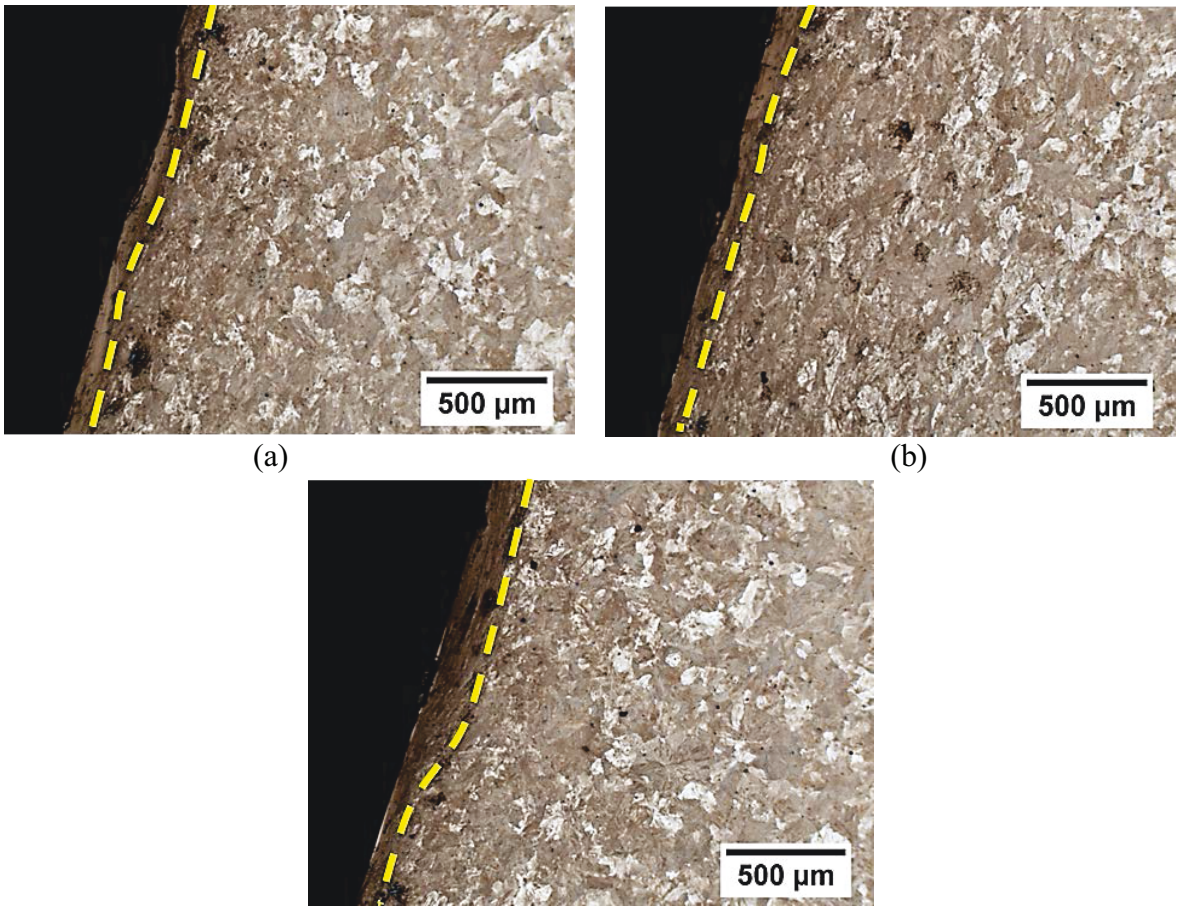

(a) (b)

(c)

Figure 2.64 WEL in the (a) Middle gauge zone (b) Lower gauge zone and (c) Dark brown layer (Etched Rail 1-TG).

Rail 2: similar to Rail 1, the area near the surface of the etched **Rail 2-LT** specimen had been severely deformed, but, no WEL was observed at the surface of the specimen. This was also true for the mid-gauge and gauge corner regions of the etched **Rail 2-TG** specimen. While no WEL could be seen at the surface of the upper gauge zone, a continuous WEL was observed throughout the middle and lower gauge zones (Figure 2.65). In addition, dark brown layers could be seen at parts of these zones.

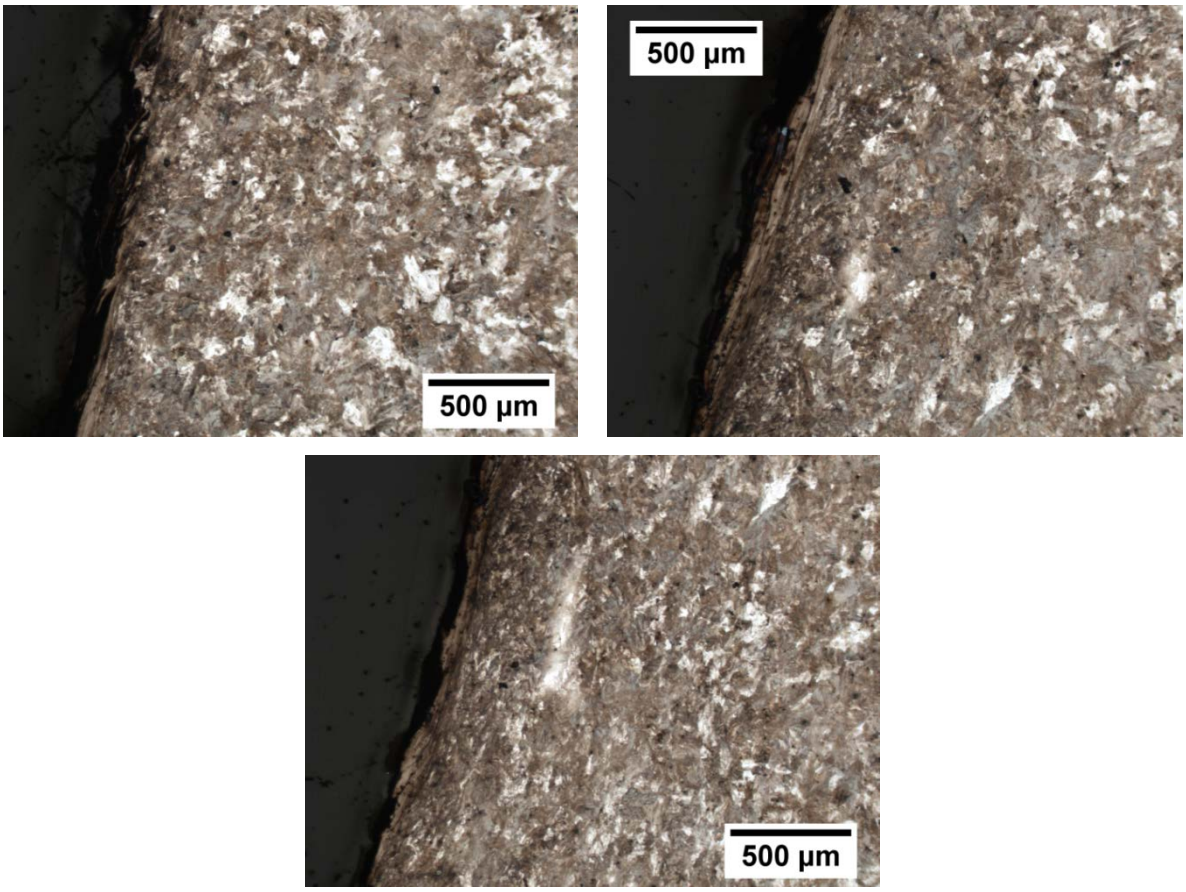

Figure 2.65 WEL at the middle and lower gauge zones (Etched Rail 2-TG).

Rail 7: unlike the two previous rails, WELs could be seen at the surface of the etched Rail **7-LT** specimen (Figure 2.66). Significant portions of the WELs were located at the opening of the cracks on the surface. Examination of the etched **Rail 7-TG** specimen also showed the presence of white etching islands at the surface of the mid-gauge and gauge corner regions, mainly at the openings of the cracks (Figure 2.67). Thin WELs could be seen all over the upper and lower gauge zones (Figure 2.68).

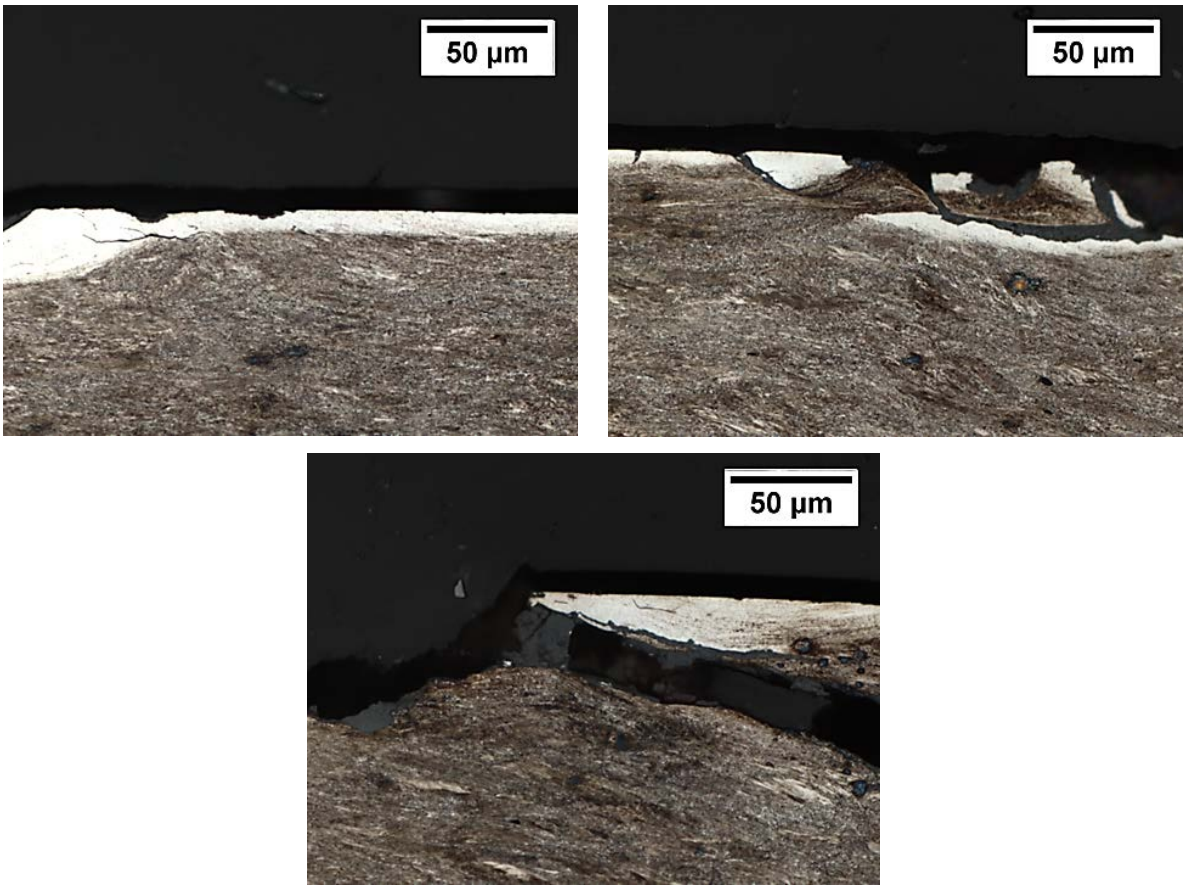

Figure 2.66 WELs at surface of longitudinal section of the mid-gauge region of Rail 7 (Etched Rail 7-LT).

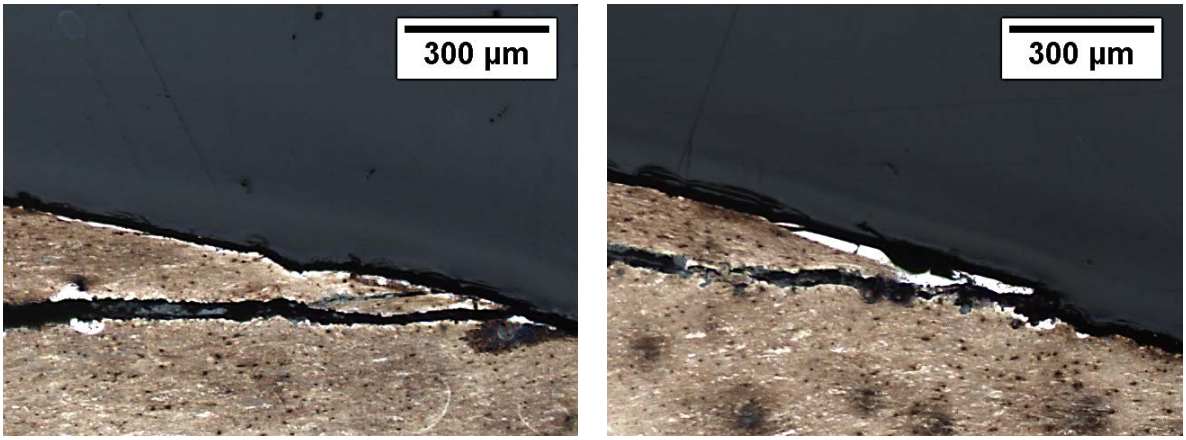

Figure 2.67 WEL at the mid gauge and gauge corner regions of Rail 7 (Etched Rail 7-TG).

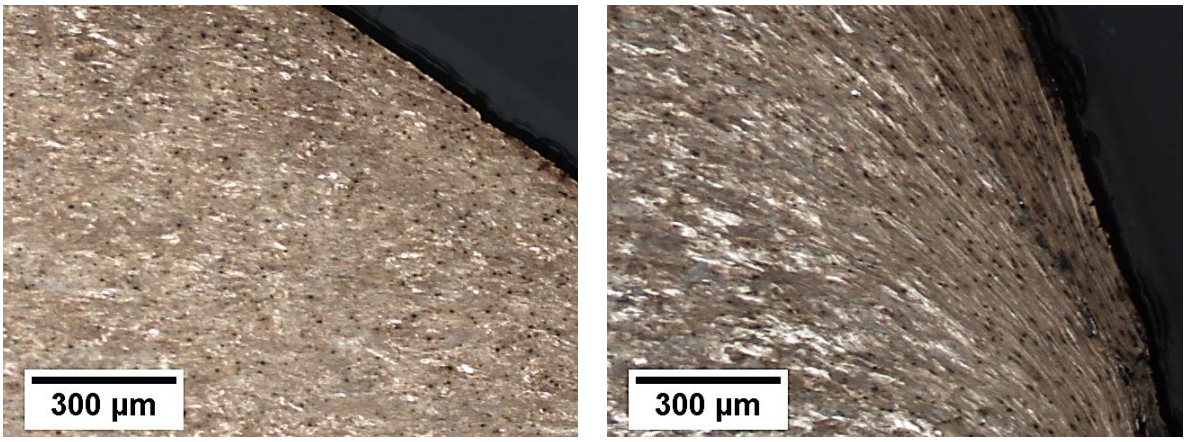

Figure 2.68 WEL at the upper and lower gauge zones (Etched Rail 7-TG).

Rail 10: A continuous layer with navy blue color was observed at the surface of the etched **Rail 10-LT** specimen. Evaluation of this layer at a higher magnification revealed that it was a WEL stained by the residual etchant (Figure 2.69). The attempts to remove the stain by repeating the metallographic preparation were unsuccessful. In addition to the WEL at the surface, pieces of white etching material could be seen inside the cracks. One interesting observation was existence of a large piece of white etching material inside one of the cracks (Figure 2.70). While presence of white etching material at subsurface is common for bearings (Sadeghi *et al.*2009), it has not been reported for rails. One possible explanation could be that the white etching material formed due to severe plastic deformation caused by crack face rubbing (Gould *et al.* 2017). Examination of the etched **Rail 10-TG** specimen showed a continuous WEL at the surface of the mid-gauge region and several white etching islands in the gauge corner region (Figure 2.71). Several thin WELs were observed at the surface of the upper gauge zone (Figure 2.72a). An area near the end of the middle gauge zone (close to the lower gauge zone) was covered with a thick continuous WEL (Figure 2.72b). In addition, a continuous thin WEL could be observed all over the lower gauge zone (Figure 2.72c).

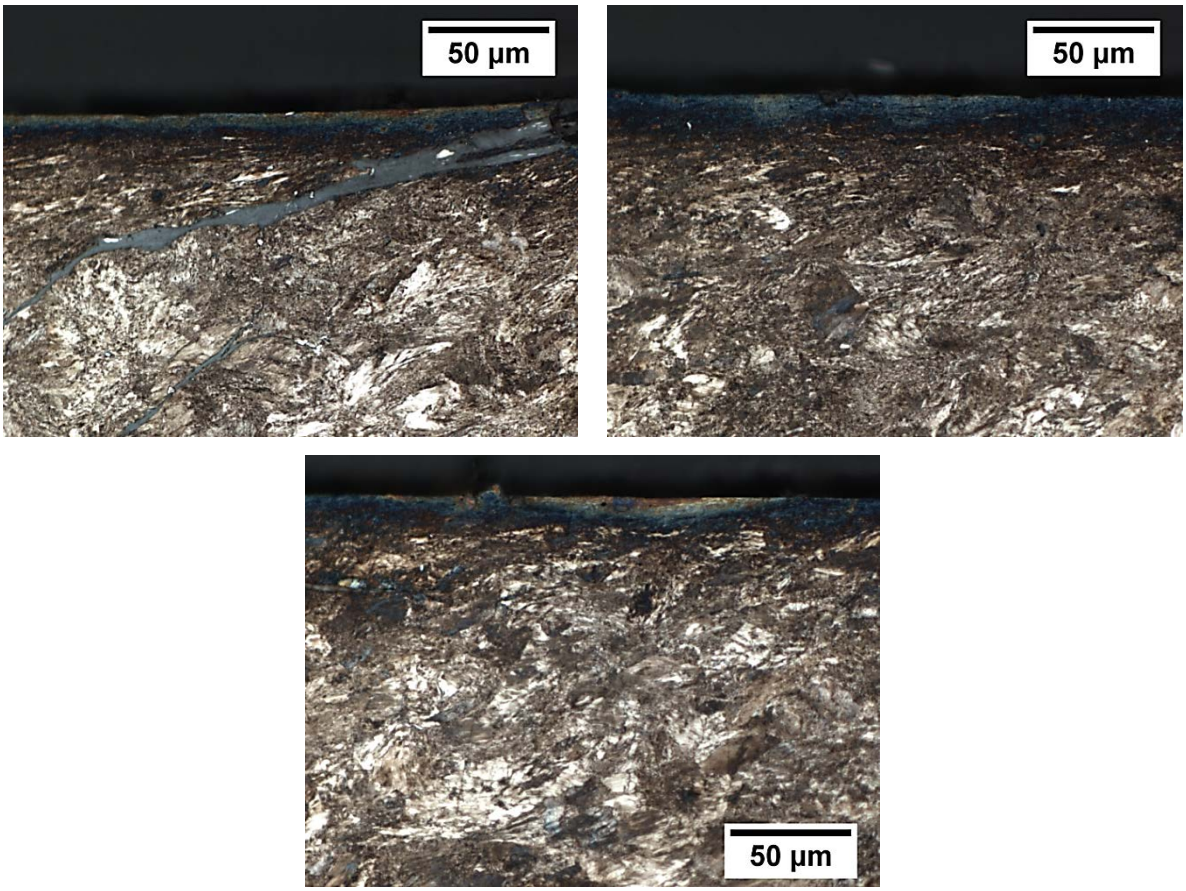

Figure 2.69 WELs at surface of longitudinal section of the mid-gauge region of Rail 10 (Etched Rail 10-LT).

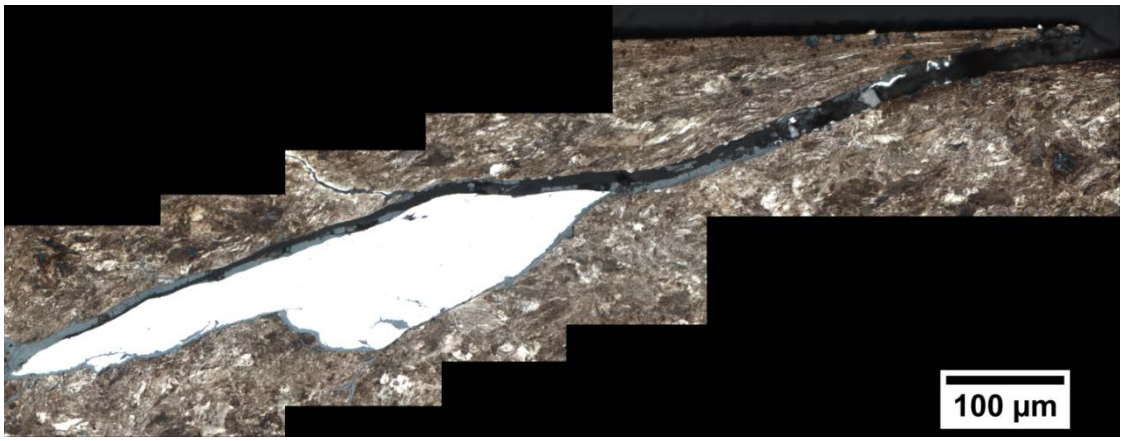

Figure 2.70 White etching material inside a crack (Etched Rail 10-LT).

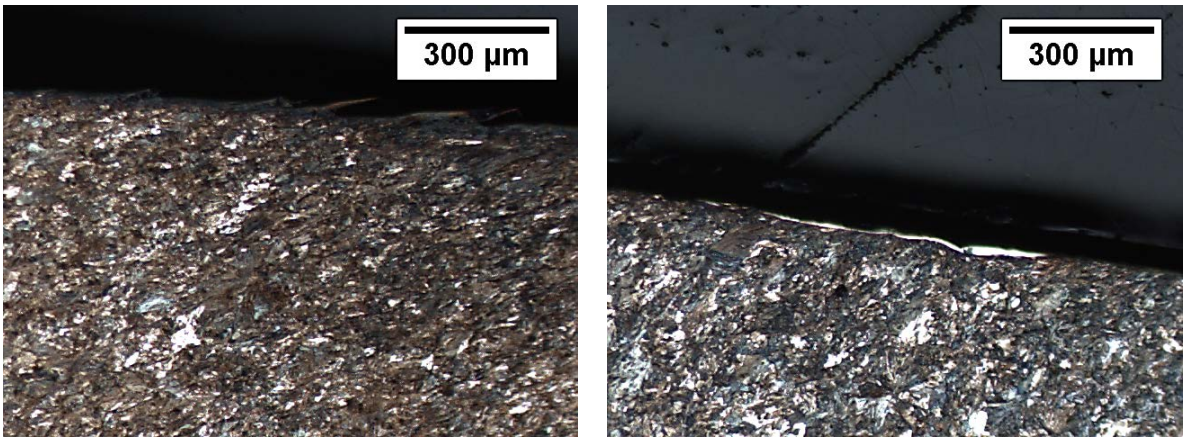

Figure 2.71 WEL at the mid gauge and gauge corner regions of Rail 10 (Etched Rail 10-TG).

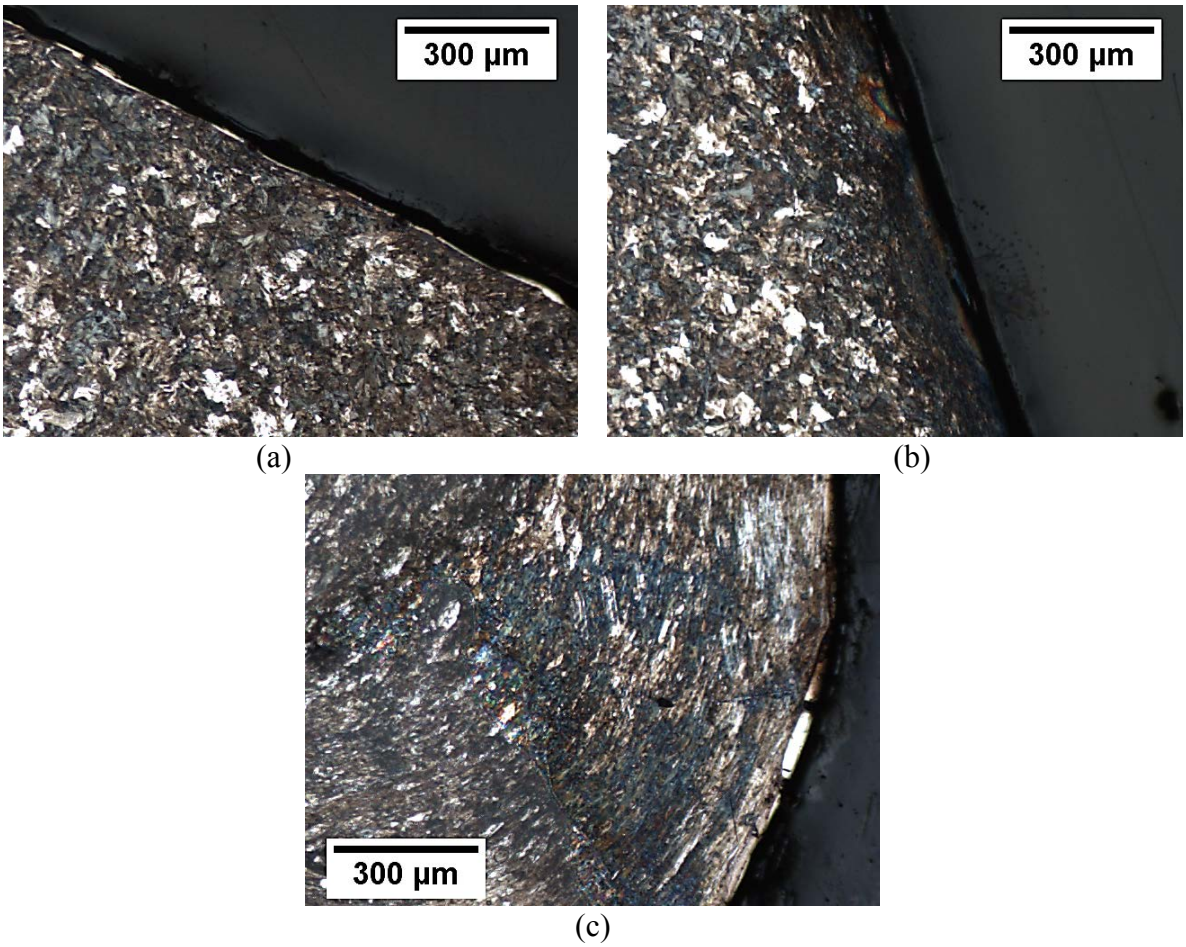

(a) (b)

(c)

Figure 2.72 WEL at the (a) Upper gauge zone (b) Middle gauge zone (c) Lower gauge zone (Etched Rail 10-TG).

Rail 12: Similar to Rail 10, a large area at the surface of the etched **Rail 12-LT** specimen was covered with a continuous WEL that was stained by the residual etchant (Figure 2.73a). Also, pieces of white etching material were observed inside the cracks (Figure 2.73c). Evaluation of the etched **Rail 12-TG** specimen revealed that the surfaces of mid-gauge and gauge corner regions were cover by a continuous WEL (Figure 2.74). While there was no WEL at the surface of the upper gauge zone, a continuous WEL was observed throughout the surfaces of the middle and lower gauge zones (Figure 2.75).

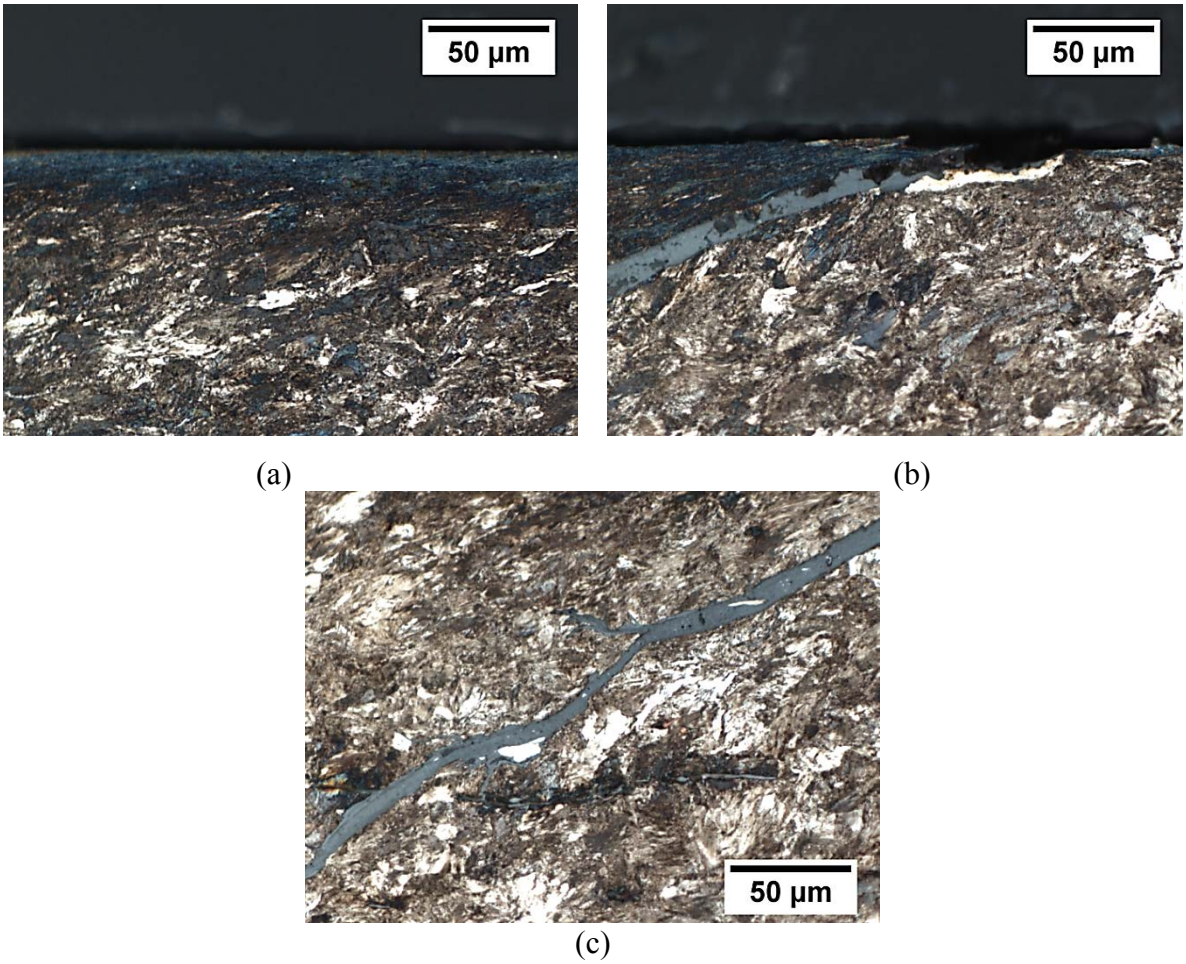

(a) (b)

(c)

Figure 2.73 WELs at surface of longitudinal section of the mid-gauge region of Rail 12 (Etched Rail 12-LT).

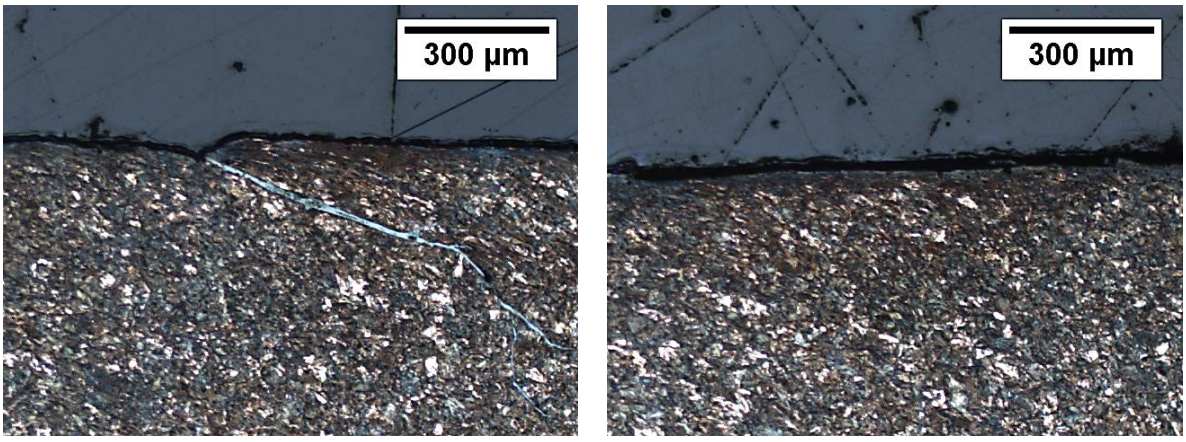

Figure 2.74 WEL at the mid gauge and gauge corner regions of Rail 12 (Etched Rail 12-TG).

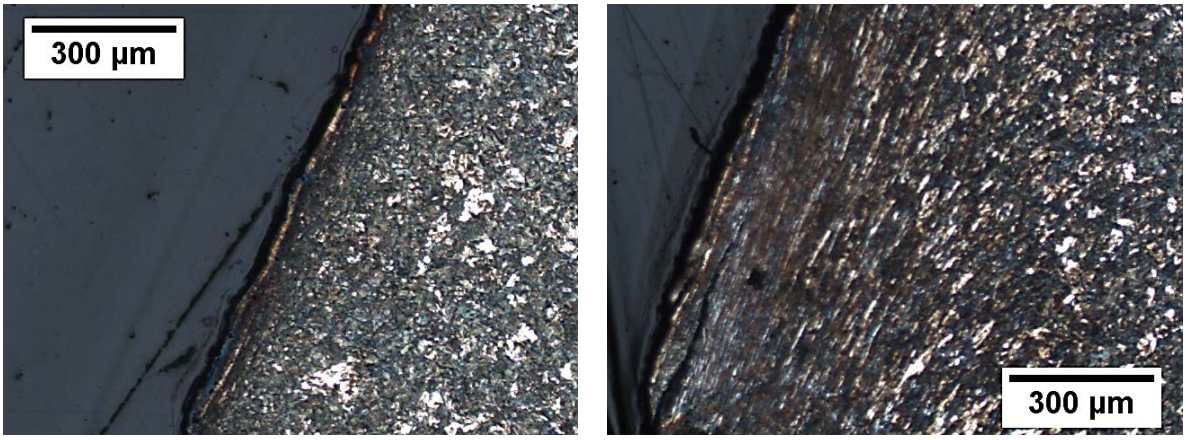

Figure 2.75 WEL at the middle and lower gauge zones (Etched Rail 12-TG).

The observations made of the WELs formed on the specimens were compared to the results from the plastic deformation analysis. For the LT specimens from Rail 1, 2 and 7 a large area near the surface had experienced severe plastic deformation, which should have made them susceptible to WEL formation. However, only the Rail 7-LT specimen showed a continuous WEL and there were no WELs at the surface of the Rail 1-LT and Rail 2-LT specimens. In

addition, while the LT Specimens from Rail 10 and 12 showed thin severely deformed areas, a continuous WEL was seen at the surface of both of them. These observations suggest that the severe plastic deformation (caused by train operation) was not responsible for the formation of WELs observed at the surface of LT specimens from Rail 7, 10 and 12, and another explanation should be provided. Steenbergen (2016) and Rasmussen *et al.* (2017) showed that grinding can cause formation of WELs on rail surfaces. Also, they reported that the head hardened rails are much more vulnerable to this damage compared to standard grade rails. The reason is that the grinding induced WELs on the surface of standard grade rails delaminate during train operation. These reports correspond well with the findings of the current study where Rail 1 and 2 were made from standard grade rail steel, and Rail 7, 10 and 12 were made from intermediate and premium grade rail steels. At the upper gauge zones, where the normal loads were dominant, no WELs could be observed at the surface of rail samples with the exceptions of Rail 7-TG and Rail 10-TG. For Rail 7-TG, this could be explained by the fact that its upper gauge zone had a layer similar to the thin plastically deformed layers from the middle gauge zones of other TG specimens. However, no explanation could be found for the presence of WELs at the upper gauge zone of Rail 10-TG. WELs could be seen at the surface of the middle and lower gauge zones of the TG specimens, where the shear loads were dominant. Since the middle and lower gauge zones are not affected during the grinding, their WELs were formed as a result of sever plastic deformation caused by train operation.

In order to see if there were any connections between the formation of the WELs and initiation of cracks, micrographs of WELs were compared to the ones from the crack path analysis. These comparisons revealed that WEL was the main reason behind the delaminations which were observed at the gauge regions of Rail 1, 2, 10 and 12 **TG specimens**. Angled crack

had initiated in the WEL and after reaching the deformed layer just below the WEL, propagated along the deformation line. In cases that there was a gap in the WEL near the crack tip, it had propagated toward the gauge surface. These findings support the damage mechanism proposed for the delamination in the crack path analysis section and are in agreement with the observations of other studies (Rasmussen *et al.* 2017; Zeng *et al.* 2017). For Rail 2, it could be seen the delamination at the gauge region had peeled up.

Considering the length of the cracks in the mid-gauge and gauge corner regions of Rail 7, it seemed that the initiation of the cracks was not related to the observed WELs. Moreover, as previously mentioned, significant portions of the white etching materials were accumulated at the cracks tips. This suggests that the cracks had initiated due to ratcheting, and then the WELs build up during crack growth phase because of increased microslip at the opening of these cracks (Steenbergen 2015). For the mid-gauge and gauge corner regions of Rails 10 and 12, the continuous WELs were peeled up in some areas, resulting in the formation of shallow surface cracks. Some of these shallow surface cracks had propagated down into the pearlitic structure. Examination of the **LT specimens** resulted in observations similar to the ones made for the mid-gauge regions of the TG specimens.

2.2.2.4. Decarburization

There were no decarburized layers at the running surface of the examined rails. However, evaluation of etched TG samples revealed presence of decarburized layers at the plastic flow lips of all the rail samples except Rail 7. The decarburized layers were found in locations outside the wheel/rail contact zone. It is possible that these were remaining of initial decarburized layers that could not be removed by grinding because of their locations. Another explanation could be that the temperature had increased because of severe shear strains resulting in decarburization.

The decarburized layer of **Rail 1** (Figure 2.76a) had a length of 2274 µm and its thickness varied between 120 and 220 µm. The length of decarburized layer for **Rail 2** (Figure 2.76b) was 3197 µm and its thickness varied between 120 and 320 µm. For **Rail 10** (Figure 2.76c), it was not possible to measure the length and thickness of the decarburized layer because the plastic flow lip was severely deformed. The decarburized layer of **Rail 12** (Figure 2.76d) had a length of 1023 µm and a thickness varying between 120 and 320 µm.

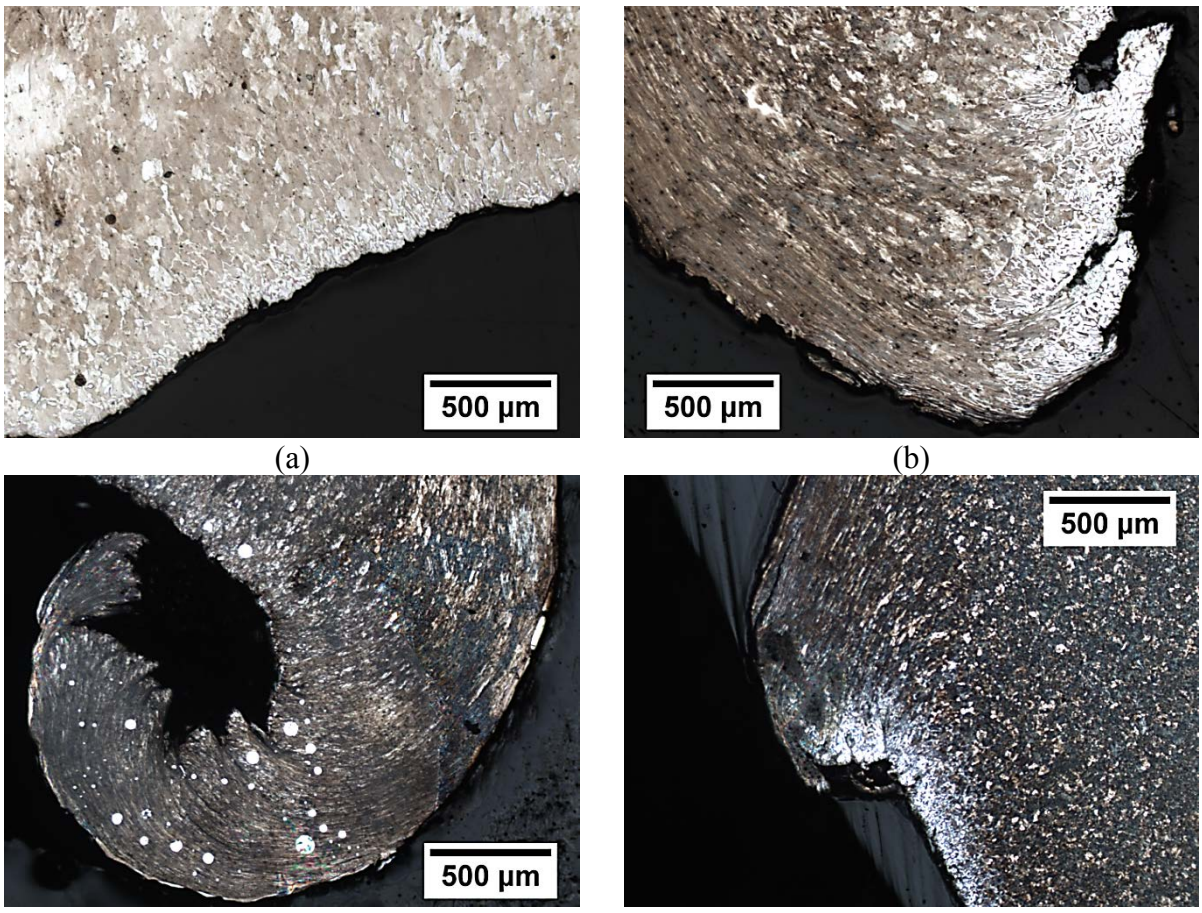

(a) (b)

(c) (d)

Figure 2.76 Decarburized layer at the plastic flow lip of (a) Rail 1 (b) Rail 2 (c) Rail 10 (Rail 12).

A decarburized layer is softer than pearlitic microstructure, which makes it more prone to cracking. A number of cracks were observed at the decarburized layers of Rails 2 and 10 which had severely deformed plastic flow lips. In addition, several cracks could be observed at the

decarburized layers of Rails 1 and 12. The significance of these cracks is that they may cause a ***reverse transverse defect***. This type of defect initiates at a plastic flow lip and propagates as a result of bending stresses. However, details of its initiation and propagation mechanisms are not clear yet (Magel *et al.* 2016).

2.2.2.5. Role of fluids in crack propagation

It was observed that the crack roots and cracks in general were filled with a material (Figure 2.77). It has been shown that the material is iron oxide, indicating that water had probably played a role in crack propagation. It has been proposed that water can facilitate the crack growth through ***fluid entrapment/pressurization*** mechanism. In this mechanism, water is trapped in a small initiated crack after a passing wheel seals the crack mouth. The pressurized water increases the stress intensity factor (ΔK), resulting in a higher crack growth rate (Haidemenopoulos *et al.* 2106). This mechanism seems to be reasonable only for 2D cases or very short cracks because in 3D it is not feasible that a wheel completely close a crack (Garnham *et al.* 2011; Schilke *et al.* 2013). Besides, it has been suggested that the volumetric expansion that happens during the oxidation can play a role in crack propagation and branching process (Steenbergen & Dollevoet 2013). On the other hand, oxidation can reduce the crack propagation rate by impeding crack closure during unloading (Haidemenopoulos *et al.* 2106).

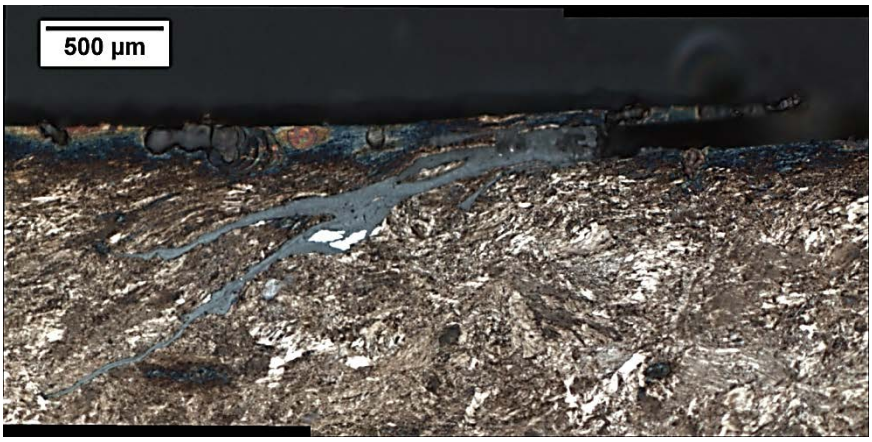

Figure 2.77 Oxidation products inside a crack.

2.2.3. Hardness measurements

Vickers micro-hardness measurements were conducted in the top of rail and gauge regions of transverse specimens (TT and TG specimens, respectively) to evaluate the mechanical properties in the near-surface area of the rail samples. Ideally, the measurements should have also been done in the mid-gauge regions of the longitudinal specimens (LT specimens) and the mid-gauge and gauge corner regions of the transverse specimens (TG specimens). However, in the first three rail samples (Rail 1, 2 and 7), these regions were severely cracked and it was not feasible to do the measurements.

Rail 1: The hardness values measured from near the running surface to depth of 1500 µm of **Rail 1-TT** specimen were highly scattered (Figure 2.78a). However, the trend showed that the hardness was, on average, ~325 HV throughout this range. Between depths of 1500µm and 2000µm, the hardness values decreased to 300 HV, and stabilized at this value afterwards. For **Rail 1-TG** specimen (Figure 2.78b), up to depth of 1500 µm, hardness values were ~340 HV. The hardness decreased slightly to ~325 HV between depths of 1500 µm and 2000 µm, then remained at ~325 HV up to a depth of 2500 µm, and decreased to 300 HV beyond that depth.

The etched Rail 1-TG specimen revealed that the hardness measurements were done in the upper gauge zone which had experienced mild plastic deformation.

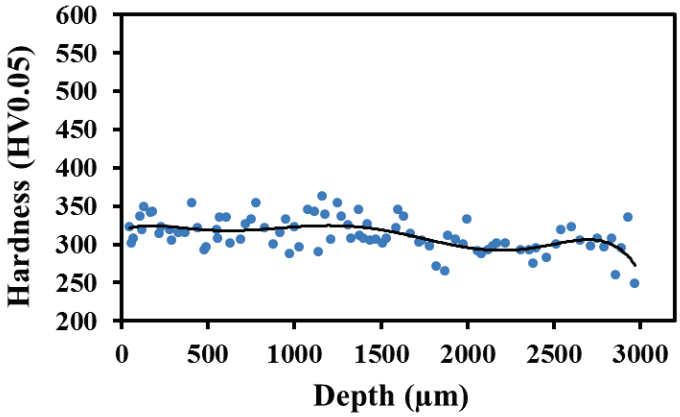

(a)

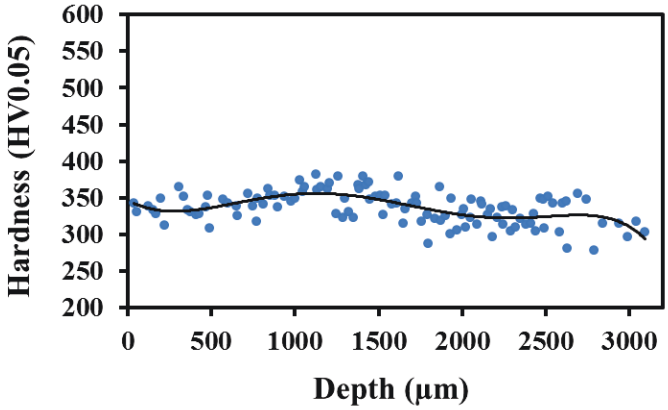

(b)

Figure 2.78 Micro-hardness depth profiles of (a) Top of rail (b) Gauge region of Rail 1 (Rail 1-TT and TG, respectively).

Rail 2: Hardness measurements conducted on **Rail 2-TT** specimen indicated a trend similar to the one of Rail 1-TT specimen (Figure 2.79a). The hardness was 325 HV up to a depth of 1500 µm, then, decreased slightly to 310 HV between depths of 1500 µm and 2000 µm and stayed at this value afterwards. For **Rail 2-TG** specimen (Figure 2.79b), the hardness decreased from 325 HV to 290 HV within the first 300 µm. Then returned to 325 HV at a depth of 1000 µm. Localized softness in near-surface area has been attributed to presence of PE ferrite

(Dylewski *et al.* 2016). However, PE ferrite was not observed in the specimen, and no other explanation could be found. Between depths of 1000 µm and 1500 µm, the hardness decreased to 310 HV, and remained at this value beyond 1500 µm. Examination of the etched Rail 2-TG specimen showed that the measurements were performed in the upper gauge zone which was mildly deformed.

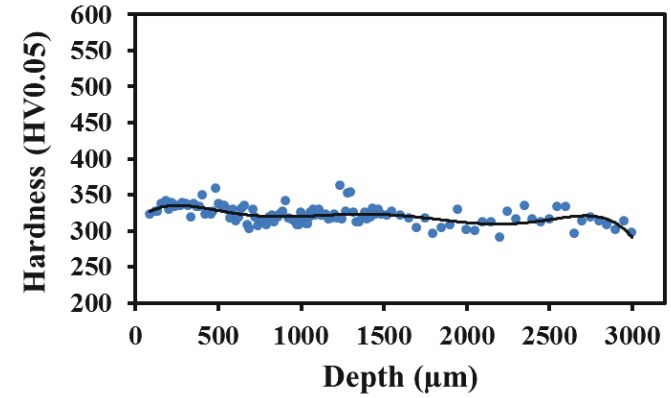

(a)

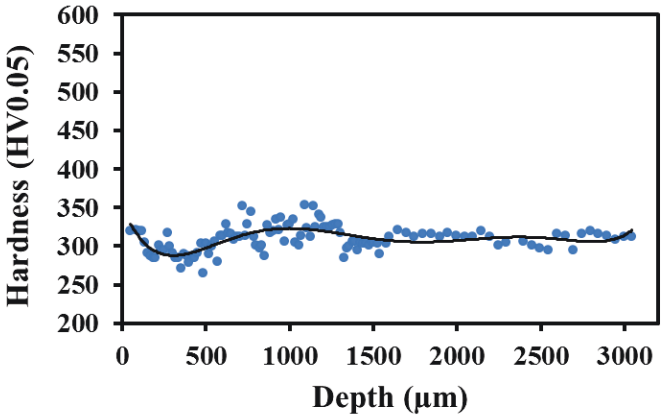

(b)

Figure 2.79 Micro-hardness depth profiles of (a) Top of rail (b) Gauge region of Rail 2 (Rail 2-TT and TG, respectively).

Rail 7: Rail 7-TT specimen showed that the hardness decreased from 385 HV to 365 HV between the running surface and a depth of 500 µm, and then remained at this value (Figure 2.80a). The hardness measurements of the **Rail 7-TG** specimen (Figure 2.80b) showed a gradual

decrease of hardness from 420 HV to 400 HV within depth of 1500 µm. Then, the hardness gradually decreased to 365 HV between the depths of 1500 µm and 2500 µm, and remained at this value afterwards. Evaluation of the etched Rail 7-TG specimen revealed that the measurements were taken in an area close to the lower gauge zone, which exhibited significant plastic deformation up to a few millimeters.

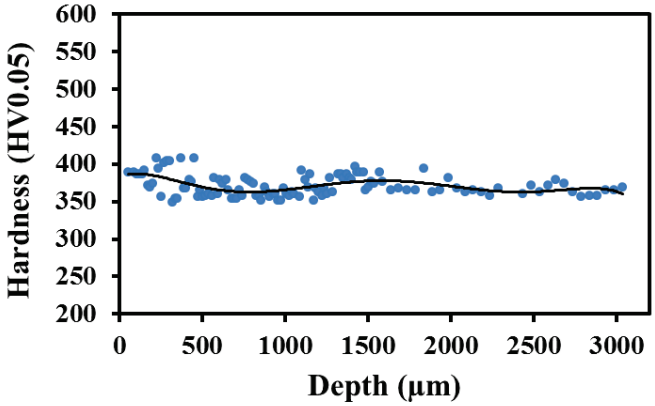

(a)

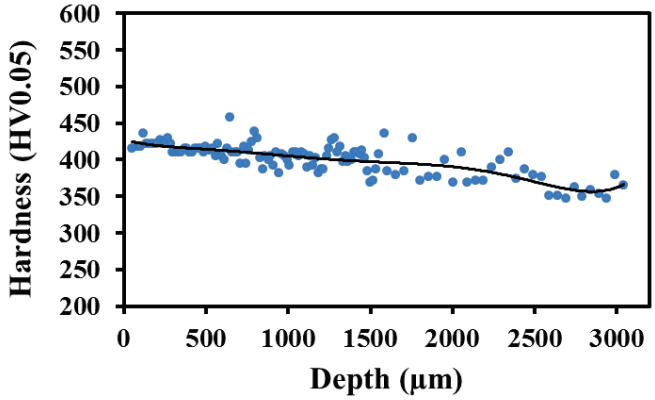

(b)

Figure 2.80 Micro-hardness depth profiles of (a) Top of rail (b) Gauge region of Rail 7 (Rail 7-TT and TG, respectively).

Rail 10: Hardness measurements done on **Rail 10-TT** specimen demonstrated a sharp decline from 525 HV to 460 HV within depth of 500 µm and remained at this value afterwards (Figure 2.81a). For **Rail 10-TG** specimen (Figure 2.81b), a sharp decrease in the hardness from

535 HV to 480 HV was observed between the running surface and depth of 500 µm. The hardness remained at approximately 480 HV down to depth of 1500 µm, then gradually decreased to ~450 HV between depths of 1500 µm and 2500 µm, and stabilized at this value afterwards. The etched Rail 10-TG specimen showed that the measurements were conducted in an area at the bottom of the upper gauge zone, which was significantly deformed up to a few millimeters.

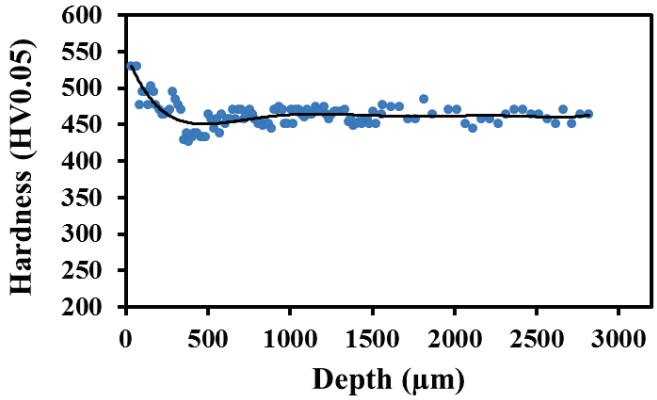

(a)

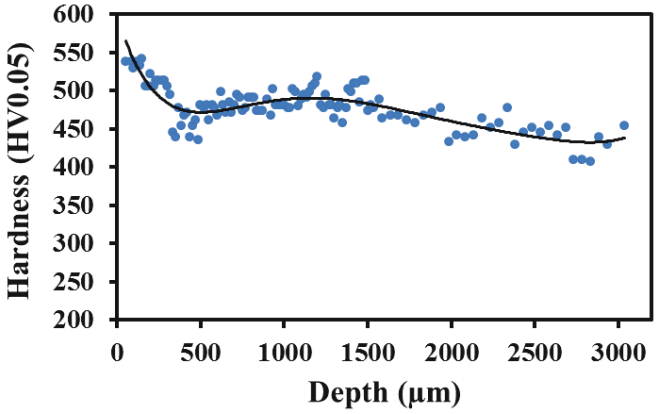

(b)

Figure 2.81 Micro-hardness depth profiles of (a) Top of rail (b) Gauge region of Rail 10 (Rail 10-TT and TG, respectively).

Rail 12: Rail 12-TT specimen (Figure 2.82a) revealed that the hardness experienced a slight decrease from 470 HV to 455 HV within a depth of 200 µm, and remained at this value up

to a depth of 800 µm. Then, the hardness decreased to 425 HV between depths of 800 µm and 1000 µm, and kept this value up to a depth of 1400 µm. Between depths of 1400 µm and 1600 µm, the hardness decreased slightly to 410 HV, and remained at this value afterwards. For **Rail 12-TG** specimen (Figure 2.82b), the hardness was ~465 HV up to a depth of 1500 µm. Then, the hardness gradually decreased to 410 HV, and then remained at this value. Examination of the etched Rail 12-TG specimen demonstrated that the measurements were done in an area at the top of the middle gauge zone, which showed signs of significant plastic deformation up to a few millimeters.

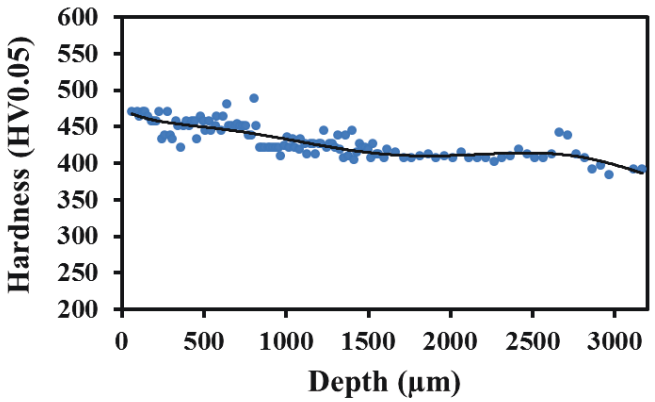

(a)

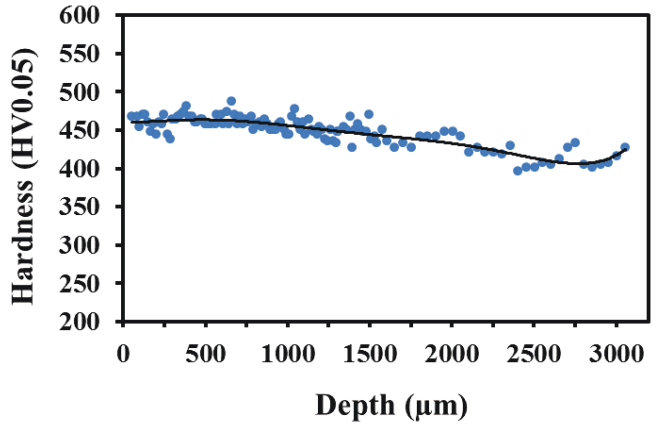

(b)

Figure 2.82 Micro-hardness depth profiles of (a) Top of rail (b) Gauge region of Rail 12 (Rail 12-TT and TG, respectively).

3. Microstructure-based Modeling of Fatigue Failure in Pearlitic Rail Steels

3.1. Numerical Procedures

3.1.1. Microstructure model generation

3.1.1.1 Voronoi tessellation

In order to further explore the effect of microstructure on fatigue behavior of rail steels, a 2D microstructure model of pearlitic rail steel with PE ferrite at grain boundaries was generated using the Voronoi tessellation. In this method, first, a set of seed points are randomly placed within the domain. It is assumed that the number of points is finite and the points are all distinct so that no points concur in the domain. Then, regions are constructed around the seed points so that all points encompassed by a particular region are closer to the seed point of that region than to seed point of any other region. As a result, the regions cover the entire domain with no gaps and they overlap only on their boundaries. As shown in Figure 3.1, these regions are in the form of convex polygons, known as Voronoi polygons or cells, which represent the prior-austenite (PA) grains. This is the grain structure that would exist if the grains start to grow from all the nucleation points together at the same rate. Grain size can be controlled by defining the density of seed points and/or the minimum and maximum distances between the seed points (Jalalahmadi & Sadeghi 2009; Warhadpande & Sadeghi 2010; Franklin *et al.* 2011; Paulson *et al.* 2015). In order to account for the PE ferrite at the grain boundaries, the tessellation boundaries should have a certain width. This can be accomplished by transforming the single-line boundaries into double-line ones utilizing the rule of vector addition/subtraction

(Zhou *et al.* 2012). *Homtools* (Lejeunes & Bourgeois 2011) which is a set of open-source Python scripts for *Abaqus* FEA software (Abaqus 6.14 documentation) was used to produce 2D Voronoi tessellation with double-line boundaries. In order to generate the tessellation, besides width and height of domain, the script requires number of Voronoi cells, minimum distance between seed points, and thickness (width) of double-line boundaries.

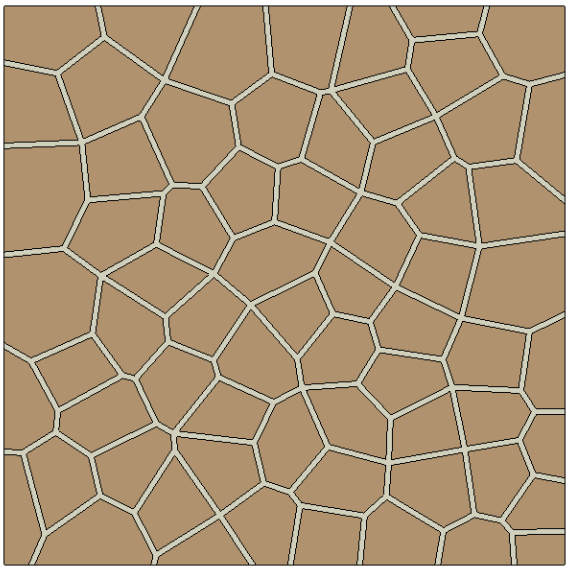

Figure 3.1 Typical domain tessellated with Voronoi method.

To define the mentioned parameters, the microstructural characteristics (grain size and percentage of PE ferrite) reported by Garnham *et al.* (2007) were used as reference (Table 3.1). In their study, they heat treated a standard grade rail steel (labeled as "RN") in two ways; to maximize ("R84") and minimize ("R115") the PE ferrite content. The grain sizes were reported as equivalent circular diameters. But, since most of the generated Voronoi polygons had five sides, the grain sizes were converted to equivalent pentagonal diameters.

Table 3.1 Microstructural characteristics of pearlitic rail steels with three different PE ferrite content [from Garnham and Davis (2007)].

Material	R84	RN	R115
PA grain size, G_A/ASTM	6-4	4-3	4-2
Equivalent circular diameter (μm)	44-88	88-125	88-177
PE ferrite (%)	11.0±2.0	5.8±1.2	2.0±1.6
Average equiv. circular diameter (μm)	66	106	132
Average equiv. pentagonal diameter (μm)	61	98	123
Minimum equiv. pentagonal diameter (μm)	41	82	82

The number of Voronoi cells was obtained by dividing the domain's area by the average Voronoi cells' area. The minimum distance between the seed points was defined as the minimum equivalent pentagonal diameter plus the thickness of grain boundaries. Moreover, the thickness of grain boundaries was found using the following equation (Eriksson *et al.*2011):

$$r_{gb} \approx \frac{3w_{gb}}{d_g} \tag{3.1}$$

where r_{gb} is the volume fraction of the grain boundaries, w_{gb} is the grain boundary width, and d_g is the grain diameter. Using Equation 3.1, the grain boundary widths for R84, RN and R115 steels were found to be ~2.4, ~2 and ~0.9 μm, respectively. However, meshing a grain boundary with any of these widths would require very small elements and, consequently, long computational times. Instead, it was decided to use grain boundary widths of 5, 7.5 and 10 μm.

As shown in Figs. 3.2a-c, to investigate the effect of grain boundary width on the crack initiation and propagation, three (3) microstructure models with minimum and average grain sizes of 82 and123 μm, and grain boundary widths of 5, 7.5 and 10 μm were used. These microstructure models had PE ferrite contents of about 12, 18 and 24%, respectively. In addition,

a microstructure model with minimum and average grain sizes of 41 and 61 µm, and grain boundary width of 5 µm (PE ferrite content of 24%) was used to evaluate the effect of grain size (Figure 3.2d). The reason that 123 µm was considered as the main grain size was to keep the PE ferrite contents in a reasonable range (Franklin *et al.* 2008). It should be noted that the grain sizes and grain boundary thicknesses were input to the script in millimeters. A plane strain thickness of 1 was assumed for the models.

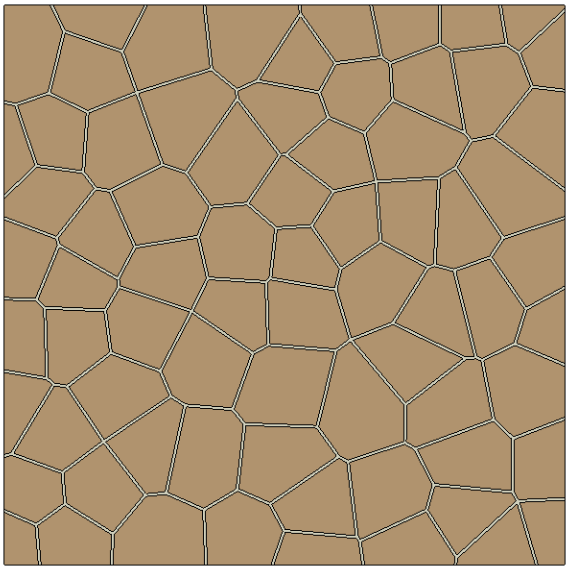

(a)

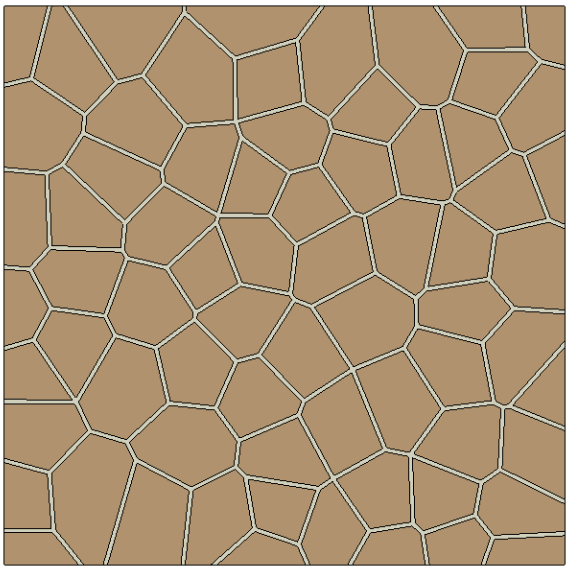

(b)

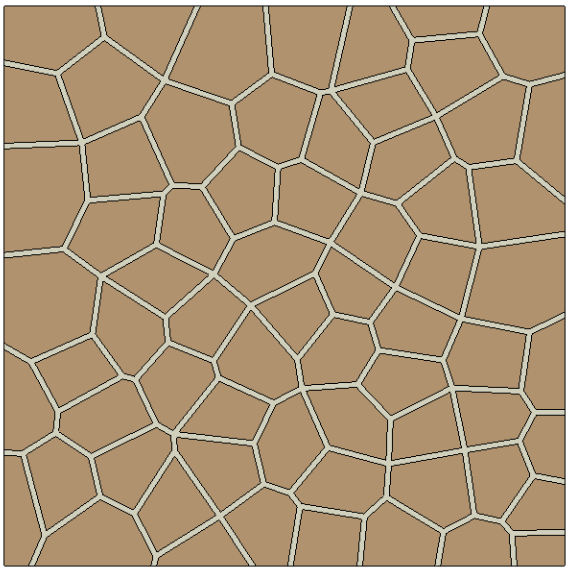

(c)

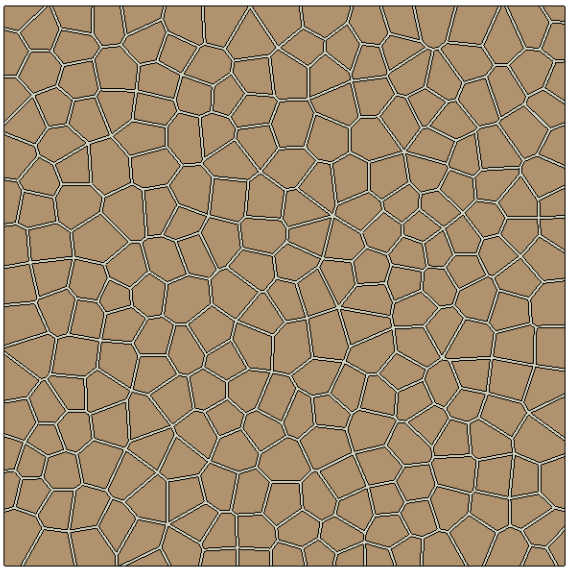

(d)

Figure 3.2 Microstructure models with average grain size and grain boundary width of: (a) 123 and 5 μm (b) 123 and 7.5 μm (c) 123 and 10 μm (d) 61 and 5 μm (domain size of 1.5×1.5 mm^2).

3.1.1.2. Meshing

The microstructure models were discretized using the free meshing technique and quadrilateral elements. The mesh seeds were placed along the edges of the grain boundaries and

the seed density was controlled by specifying the average element size. Average element size of 0.003 mm was the largest that could be used, without having any distorted elements. The 4-node bilinear plane strain quadrilateral elements (CPE4R) with reduced integration and hourglass control were assigned to the meshes.

3.1.1.3. Sensitivity analyses

In order to determine if the domain size is large enough to properly represent the properties of the material, a sensitivity analysis was done using domains with different sizes of 0.5×0.5, 0.75×0.75, 1×1 and 1.5×1.5 mm^2 (Figure 3.3). The effect of domain size was assessed with respect to global cyclic stress-strain response of the material with grain size and grain boundary thickness of 123 and 5 μm, respectively. To account for the scattering of the response, five (5) randomly generated microstructure models were used for each domain size. Once the suitable domain size was obtained, microstructure models with different mesh sizes of 0.002 and 0.003 mm were used to analyze the mesh sensitivity (Figure 3.4).

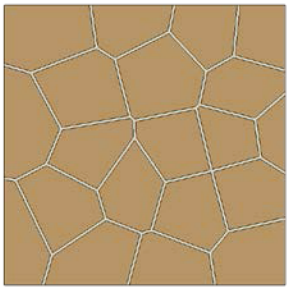

(a)

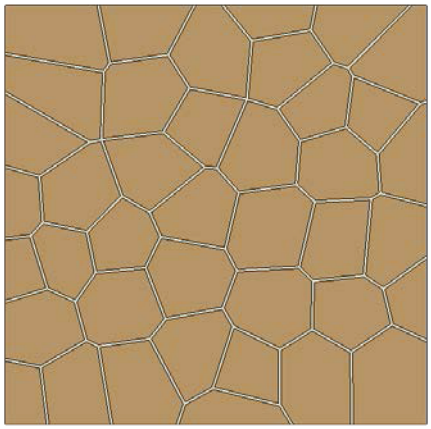

(b)

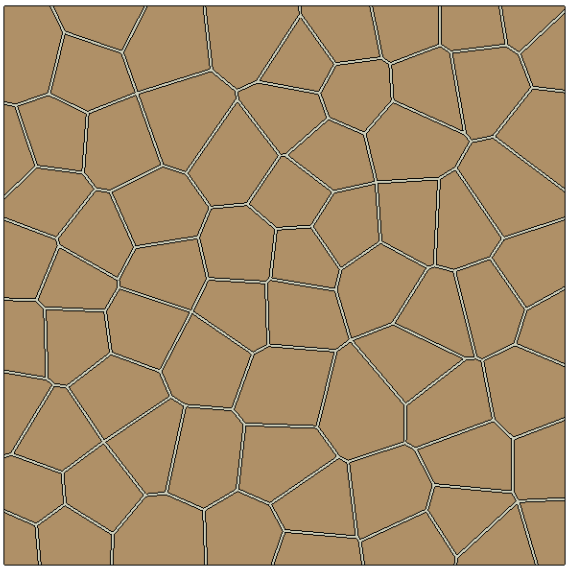

(c)

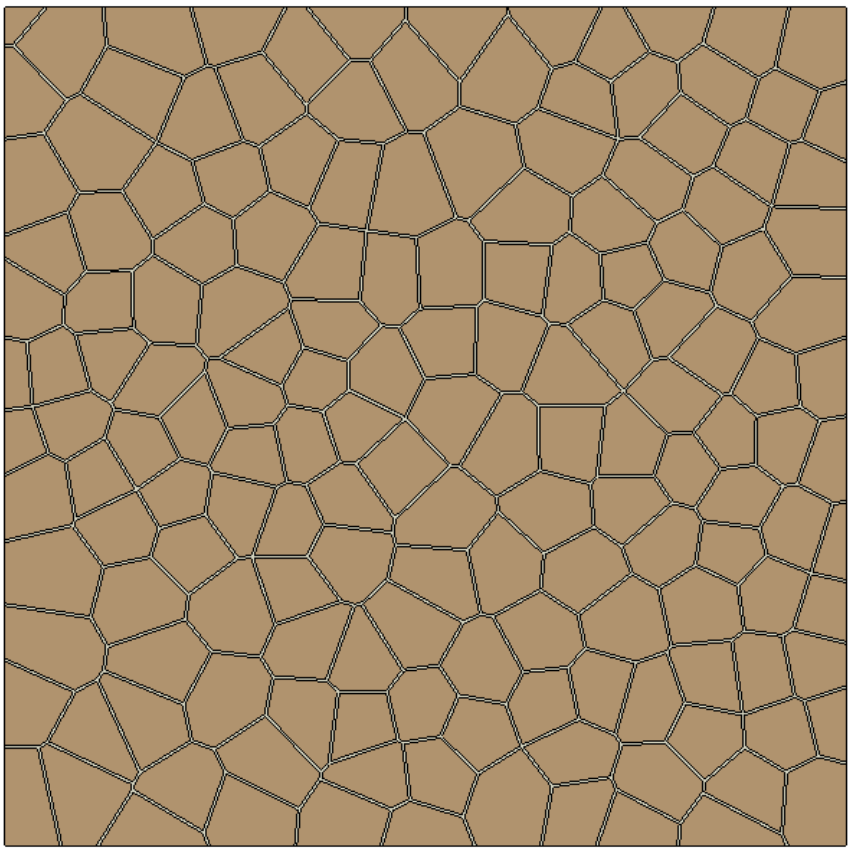

(d)

Figure 3.3 Microstructure models with domain size of (a) 0.5×0.5 mm^2 (b) 0.75×.75 mm^2 (c) 1×1 mm^2 (d) 1.5×1.5 mm^2 (grain size of 123 μm and grain boundary width of 5 μm).

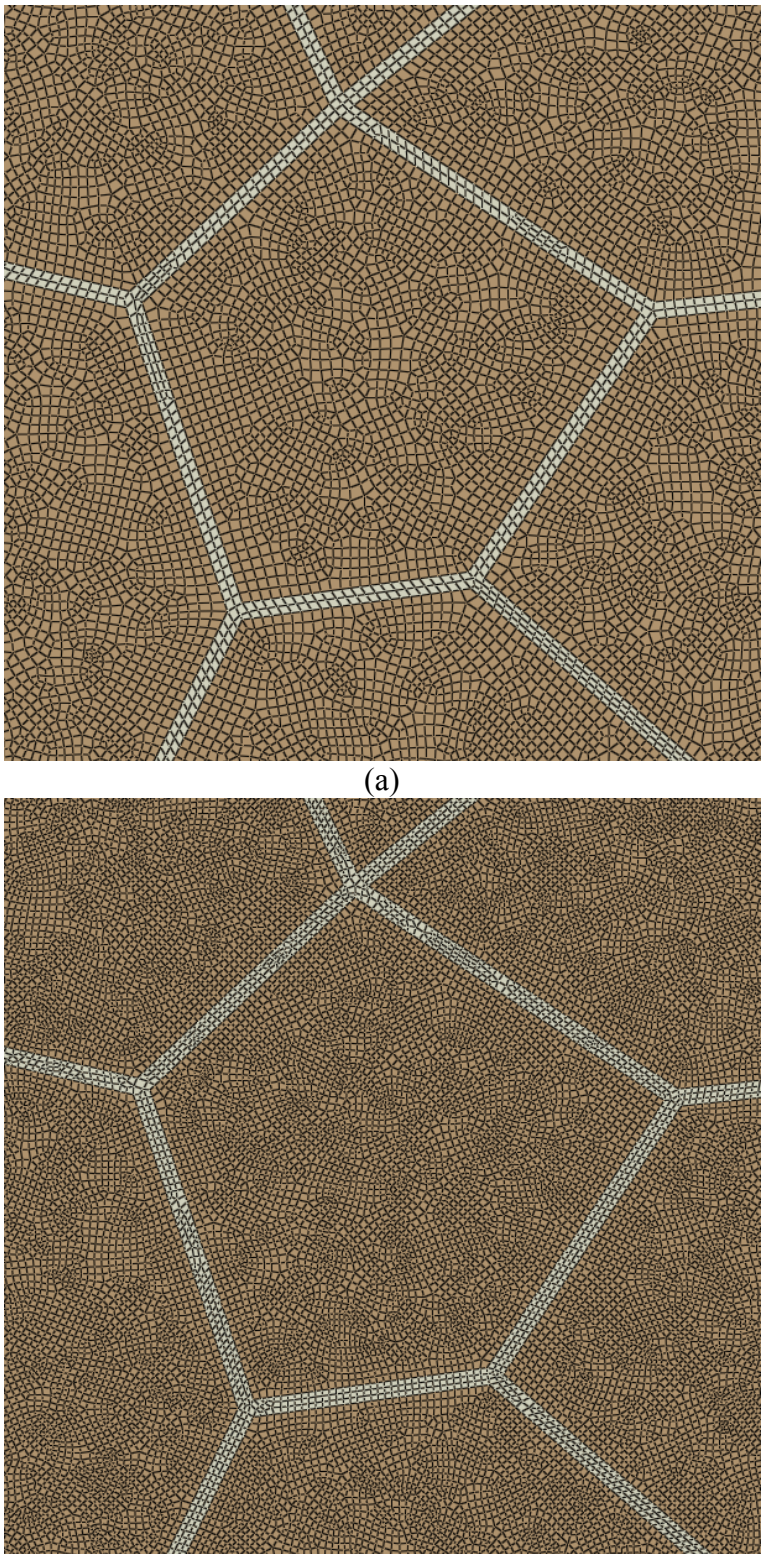

Figure 3.4 Part of a microstructure model meshed with elements size of (a) 0.003 mm (b) 0.002 mm (grain size of 123 μm and grain boundary width of 5 μm).

3.1.3. Material model

3.1.3.1. Nonlinear kinematic hardening model

To study the cyclic plastic deformation behavior of pearlitic rail steel with PE ferrite at grain boundaries, an appropriate kinematic hardening model has to be considered. The nonlinear kinematic hardening model proposed by Chaboche (1991) was used to define the cyclic stress-strain response of pearlite and PE ferrite separately. The model is expressed as (Chaboche 1991):

$$d\bar{\alpha} = \sum_{i=1}^{3} d\alpha_i \tag{3.2}$$

$$d\bar{\alpha} = \frac{2}{3}.C_i.d\bar{\varepsilon}^p - \gamma_i\bar{\alpha}_i d\varepsilon_{eq}^p \tag{3.3}$$

where C_i and γ_i denote kinematic hardening coefficient and kinematic hardening exponent, respectively, which are material constants. $d\alpha_i$ is the back-stress increment vector, $d\bar{\varepsilon}^p$ is the plastic strain increment vector, and $d\varepsilon_{eq}^p$ is the equivalent plastic strain increment. The index i (ranging from 1 to 3) represents the individual back-stress tensor in the third order Chaboche model. In Equation 3.3, the first term denotes the hardening modulus and the second term is a "recall term" that represents the nonlinear effect. The hardening rate during plastic deformation is controlled by the material constant γ_i. According to the model, the total back-stress (α) is the summation of the three decomposed back-stresses ($\alpha = \alpha_1 + \alpha_2 + \alpha_3$). The first back-stress ($\alpha_{1)}$) predicts the high plasticity modulus at the start of yielding and it saturates very quickly. The second back-stress (α_2) represents the transient nonlinear part of the hysteresis loop. Finally, the third back-stress (α_3) simulates the linear hardening in the higher strain range. The loading segment of the stress-strain curve is represented as:

$$\sigma = \sigma_0 + \alpha_1 + \alpha_2 + \alpha_3 \tag{3.4}$$

where σ_0 is the cyclic yield stress.

For the pearlite, the material constants of a fully pearlitic steel (UIC 900A rail steel) reported by Schleinzer and Fischer (2001) were considered. And, the materials constants of ferrite reported by Moeini *et al.* (2017) were used for the PE ferrite. The obtained Chaboche kinematic hardening parameters are provided in Table 3.2. In addition, for both pearlite and PE ferrite, Young's modulus (E) of 206,000 MPa and Poisson's ratio (υ) of 0.28 were assumed.

Table 3.2 Chaboche kinematic hardening parameters [from Moeini *et al.* (2017) and Schleinzer and Fischer (2001)]

Material	σ_0 (MPa)	C_1 (MPa)	C_2 (MPa)	C_3 (MPa)	γ_1	γ_2	γ_3
PE Ferrite	300	42880	5505	980	1600	39	1.5
Pearlite	379	24750	60000	200000	55	600	2000

3.1.3.2. Low-cycle fatigue (LCF) damage model

The crack initiation and propagation due to progressive degradation of material stiffness under cyclic loading was modeled using a continuum damage mechanics (CDM) model. In CDM, the degradation of material stiffness is accomplished by introducing a damage variable, D, which represents the degree of damage in the material (Chaboche 1988). The damage variable is a tensor quantity; however, it can be reduced to a scalar variable assuming that the damage is isotropic. Also, it is assumed that the damage does not affect the Poisson's ratio (Lemaitre & Desmorat 2005). In this way, the stress tensor at any given loading cycle during the simulation is expressed by:

$$\sigma = (1 - D)\bar{\sigma} \tag{3.5}$$

where $\bar{\sigma}$ is the undamaged stress tensor computed in the current increment.

The damage model requires a damage initiation criterion to predict the onset of the damage, and a damage evolution criterion to calculate the rate of degradation of the material stiffness. In the current study, these two criteria are characterized by the accumulated inelastic hysteresis energy per cycle, ΔW, in the stabilized state. The number of cycles that corresponds to the damage initiation is given by (Abaqus 6.14 documentation):

$$N_{int} = c_1 \Delta w^{c_2} \tag{3.6}$$

After the damage initiation criterion is fulfilled at a material point, the degradation of material stiffness is commenced with the damage per cycle rate which is given by:

$$\frac{dD}{dN} = \frac{c_3 \Delta W^{c_4}}{L} \tag{3.7}$$

where c_1, c_2, c_3 and c_4 are material constants, and L is the characteristic length which is correlated to the integration points. The purpose of the characteristic length is to scale the Δw with the mesh size. For simplicity, it was assumed that L is equal to the mesh size. According to Equation 3.5, the material loses its load carrying capacity when D reaches unity. An element is removed from the mesh once all of its integration points have lost their loading capacity.

The amount of damage per cycle can be defined as (Du *et al.* 2017):

$$D_i = \frac{\Delta W_i}{\sum \Delta W_i} \tag{3.8}$$

It can be assumed that the increment of the damage per cycle is constant during the LCF tests. Also, the damage sum can be assumed to be equal to the theoretical damage sum ($D_{th}=1$) for

simplicity, although the real value may be much smaller. Considering these assumptions and using Equation 3.6, the damage per cycle rate can be expressed as:

$$\frac{dD}{dN} = \frac{1}{N} = \frac{1}{c_{1\Delta W^{c_2}}} = \frac{1}{c_1}\Delta W^{-c_2} \tag{3.9}$$

Comparing Equation 3.7 to Equation 3.9 leads to the conclusion that:

$$c_3 = \frac{L}{c_1},$$

$$c_4 = -c_2 \tag{3.10}$$

For strain-controlled LCF tests, the accumulated inelastic hysteresis energy can be found using the following expression (Dzuibinski 1991):

$$\Delta W = \frac{4(1-n')}{1+n'}\sigma'\varepsilon'(2N)^{b+c} \tag{3.11}$$

where $n'$is the cyclic hardening exponent, $\sigma'$is the fatigue strength coefficient, ε' is the fatigue ductility coefficient, b is fatigue strength exponent and c is the fatigue ductility exponent.

The first two damage material constants (c_1 and c_2) for pearlite and PE ferrite were calculated with Equation 3.11 using material parameters reported by Dzuibinski (1991) for a pearlitic steel and a ferritic steel. Then, c_3 and c_4 were found based on Equation 3.10. The obtained damage material constants are given in Table 3.3.

Table 3.3 Damage initiation and evolution parameters [For characteristic length (L) of 0.003 mm].

Material	$C1$ ($\frac{\text{cycle}}{N^{C_2}mm^{-2C_2}}$)	C_2	C_3 ($\frac{\text{mm}}{N^{C_4}mm^{-2C_4}}$)	C_4
PE Ferrite	5.2134×10^{4}	-1.5292	5.7543×10^{-8}	1.5292
Pearlite	2.7693×10^{5}	-1.7605	1.0833×10^{-8}	1.7605

3.1.4. Boundary conditions

Homogenous boundary conditions were applied to simulate conditions close to the fully reversed strain-controlled uniaxial LCF tests. As shown in Figure 3.5, symmetric boundary conditions were assumed for the bottom and left edges of the model; the bottom edge nodes and left edge nodes were fixed in Y and X directions, respectively. In addition, equal displacement conditions were applied to the top and right edges using equation constraints. The top edge moment was constrained in Y direction with respect to the top right node and the right edge moment was constrained in X direction with respect to the top right node. Finally, a displacement was applied to the top right node along the X direction using a sinusoidal waveform with a circular frequency of 4π Rad/s. This displacement resulted in a strain amplitude and an average strain rate of 0.5% and 0.04 s^{-1}, respectively. The global cyclic stress-strain response of the model was obtained using the reaction force and displacement of the top right node along the X direction.

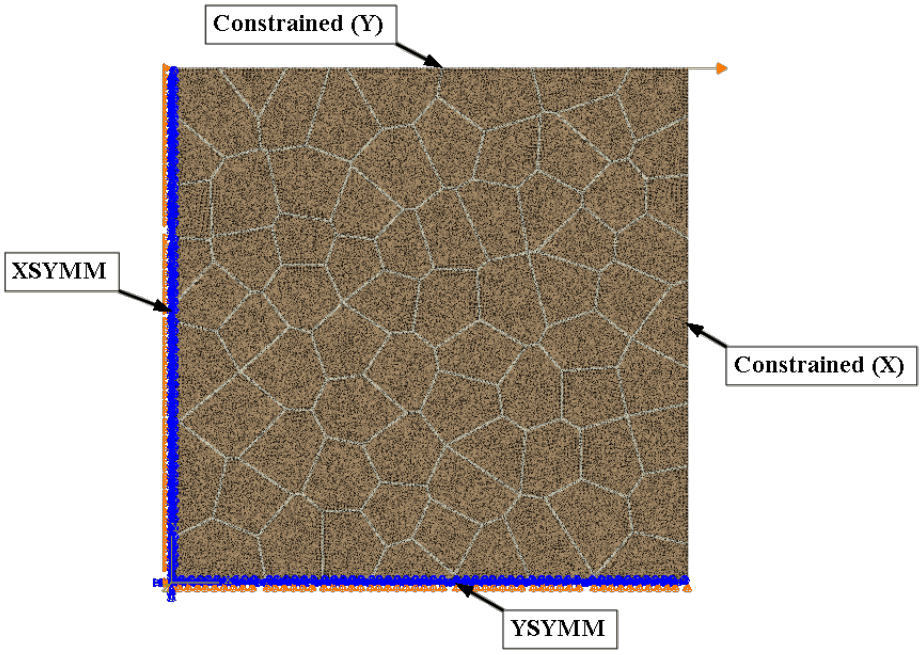

Figure 3.5 Boundary conditions.

3.1.5. Direct cyclic analysis

As mentioned before, the damage initiation and evolution criteria of the LCF damage model are based on the ΔW in the stabilized cycle. The conventional procedure is to repetitively apply the periodic loading until the stabilized response is achieved. However, this method is computationally expensive because it may require many loading cycles. To avoid this problem, a direct cyclic analysis is implemented in *Abaqus/Standard* (Abaqus 6.14 documentation), which enables the direct calculation of the stabilized response. This approach uses a Fourier series approximation along with a modified Newton method to construct a displacement function that describes the response of the structure at all times t during a load cycle with period T. Moreover, the direct cyclic analysis uses a damage extrapolation technique to speed up the LCF analysis. In this technique, the damage variable from the current cycle (D_N) is extrapolated forward over a number of cycles (ΔN) to the new damage state ($D_{N+\Delta N}$).

For the direct cyclic analysis, cycle time period, fixed increment size, and maximum number of iterations were set to 0.5 s, 0.005 and 300, respectively. Also, the number of Fourier terms was initially equal to 11, and could be increased automatically up to a maximum number of 25 Fourier terms. Moreover, the minimum and maximum numbers of cycles over which the damage is extrapolated forward were specified as 100 and 200.

3.2. Results and Discussion

3.2.1. Sensitivity analyses

3.2.1.1. Effect of domain size

The global cyclic stress-strain responses of domains with different sizes of 0.5×0.5, 0.75×0.75, 1×1 and 1.5×1.5 mm^2 were analyzed to assess the effect of domain size. It could be seen that there was no difference between the stabilized hysteresis loops obtained for different domain sizes, which means that all the domains were large enough with respect to prediction of the global cyclic stress-strain response. The obtained stabilized hysteresis loop is shown in Figure 3.6. It should be noted that since the nonlinear kinematic hardening model was used alone (i.e. isotropic component was not included for simplicity), stabilization was predicted after one cycle (Abaqus 6.14 documentation). Experimental data reported in the literature for pearlitic rail steels tested under similar loading condition show that stabilized response was obtained after about 100 cycles due to isotropic softening of the material (Ahlstrom & Karlsson 2005). In addition, the model overpredicted the maximum stress amplitude because it did not consider the effect of isotropic softening.

While all the domain sizes resulted in the same stabilized hysteresis loops, it was noticed that there was a significant difference between their numbers of cycles to damage initiation (Figure 3.7). The average N_{int} for domains with sizes of 0.5×0.5, 0.75×0.75 and 1×1 mm^2 were 39, 21.6 and 11.1% different from the average N_{int} for the domain with size of 1.5×1.5 mm^2, respectively. Due to limited computational power, 1.5×1.5 mm^2 was the largest size that could be used, and even this domain size required long computational times. Therefore, a difference of

11.1% was considered acceptable and domain size of 1×1 mm^2 was used in the rest of the simulations.

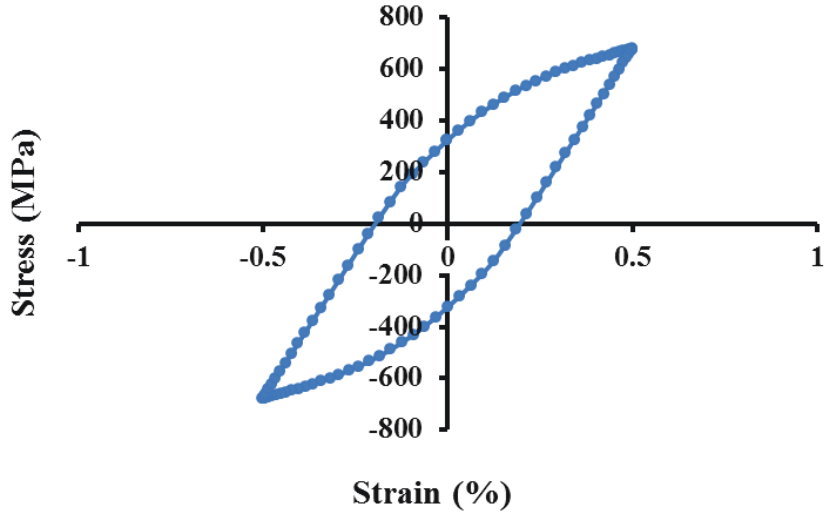

Figure 3.6 Typical hysteresis loop obtained from the sensitivity analyses.

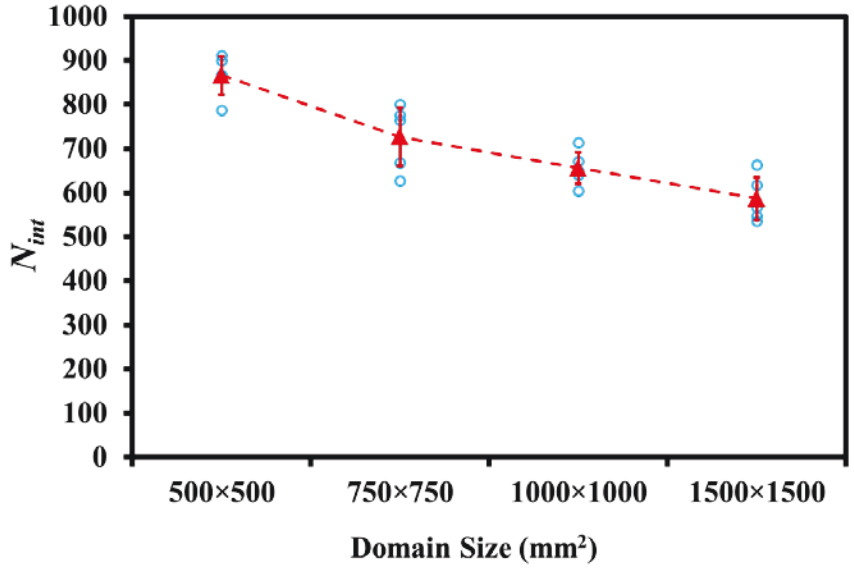

Figure 3.7 Effect of domain size on number of cycles to damage initiation (N_{int}).

3.2.1.2. Effect of mesh size

Two different average element sizes of 0.003 mm and 0.002 mm were used to evaluate the effect of mesh size. As previously mentioned, 0.003 mm was the largest average element size that could be used to have a mesh without any distorted elements. And, 0.002 mm was the smallest average element size that would be allowed by the computational power. 1×1 mm^2 microstructure models meshed using elements with average sizes of 0.003 and 0.002 mm would have about 140,000 and 310,000 elements, respectively.

The stabilized hysteresis loops obtained for the two mesh sizes were the same, which implies that the 0.002 mm mesh size was small enough for prediction of global cyclic stress-strain response. The N_{int} for the microstructure models meshed with average element size of 0.003 and 0.002 were 302 and 274, respectively. Since the difference between their N_{int} (9.7%) was in the acceptable range, the average element size of 0.002 mm was used for the rest of simulations to avoid long computational times. It should be noted that mesh dependency is alleviated during the damage evolution stage, due to implementation of the characteristic length (L) in the damage evolution law (Abaqus 6.14 documentation).

3.2.2. Fatigue crack initiation and propagation mechanisms

To investigate crack initiation and propagation mechanisms, a series of simulations were performed using five (5) randomly generated domains with grain size of 123 μm and grain boundary width of 5 μm (ferrite content of 12%), and the domain whose number of cycles to failure (N_f) was closest to the average (3146 cycles) was chosen for further analysis. Contour plots of equivalent plastic strain (PEEQ) were evaluated at different stages (i.e. different number of cycles) to see how stress and strain distribution at microstructural level affect the initiation

and propagation of fatigue cracks. In addition, contour plots of damage variable (SDEG) were used to monitor damage initiation and propagation.

Figure 3.8 shows the contour plot of equivalent plastic strain for the stabilized cycle (1st cycle). The value of PEEQ inside the pearlitic grains was about 0.07, while the ferritic grain boundaries had PEEQ values mainly between 0.13 and 0.23. This indicated strain partitioning between the PE ferrite and pearlite. Areas with PEEQ value of around 0.28 could be seen at the junctions of the grain boundaries. After 650 cycles, damage initiated at 3 points which were located at the grain boundary junctions. The values of PEEQ for the grain boundaries were between 0.15 and 0.32, whereas the PEEQ value inside the grains increased slightly to about 0.08. At the end of 850th cycle, the maximum value of PEEQ for the grain boundaries increased to 0.42, while this number was 0.1 for the grains (Figure 3.9a). It was observed that damage had initiated and evolved mainly at the grain boundary junctions along with a few grain boundaries (Figure 3.9b).

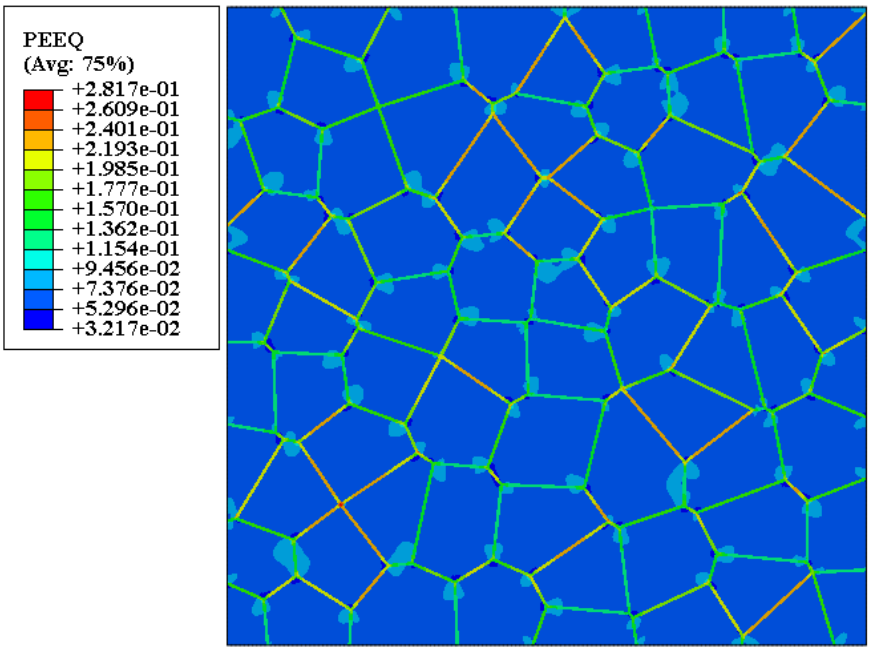

Figure 3.8 Equiv. plastic strain accumulation for microstructure model 123-5 after 1st cycle.

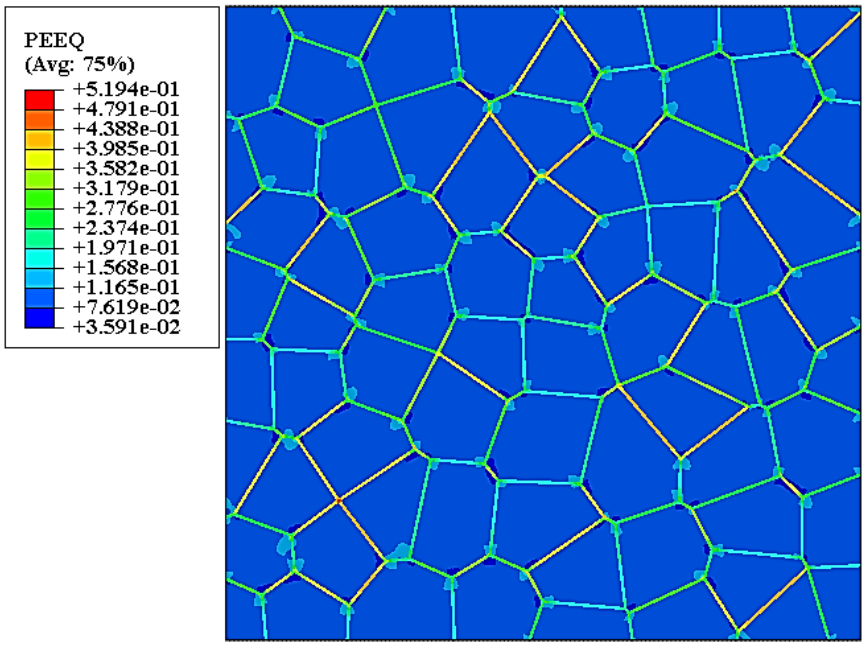

(a)

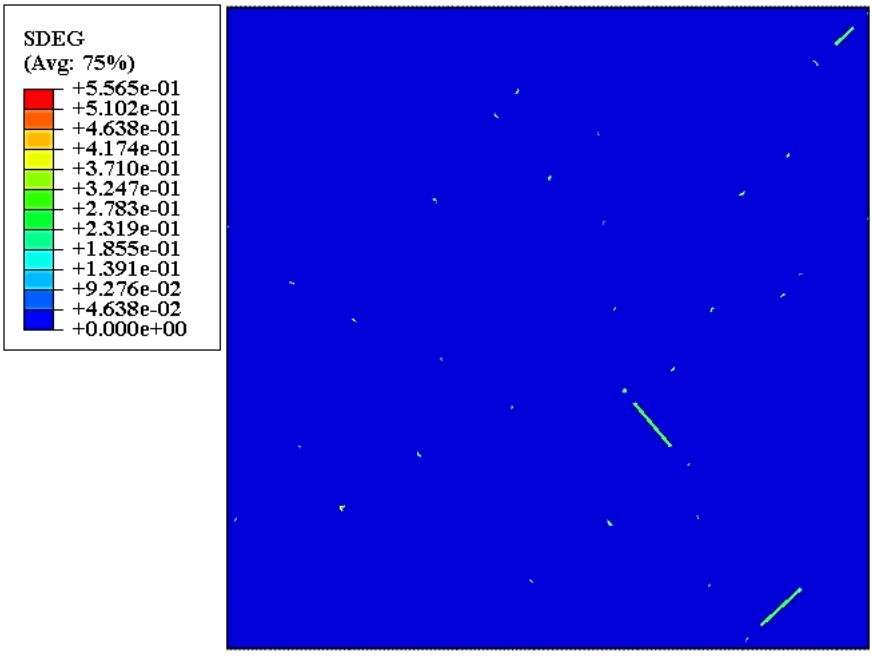

(b)

Figure 3.9 (a) Equiv. plastic strain accumulation (b) Damage state for microstructure model 123-5 after 850 cycles.

The first two (2) voids initiated after 1050 cycles were located at the grain boundary junctions. It could be seen that damage had evolved at several grain boundaries which had PEEQ value of 0.55. The rest of the grain boundaries had PEEG values between 0.22 and 0.44. After the next 200 cycles, several voids were initiated at the grain boundary junctions throughout the material (Figure 3.10a). It was observed that the PEEQ value for the damaged grain boundaries had increased to 0.77 (Figure 3.10b) and damage had evolved at several grain boundaries.

As illustrated in Figure 3.11a, at the end of 1436th cycle, several short cracks were formed along the grain boundaries as a result of void coalescence (Figure 3.11a). These observations are in agreement with the experimental findings reported by Ahlstrom and Karlsson (2009), and Garnham and Davis (2011). At this point, the newly damaged grain boundaries had PEEQ values between 1.5 and 2.5, and PEEQ values for rest of the grain boundaries were between 0.5 and 1.2 (Figure 3.11b). Moreover, it could be seen that several regions inside the pearlitic grains had PEEQ values between 0.35 and 0.45, which implied that the sites of plastic strain localization had started to move from the ferritic grain boundaries to the inside of pearlitic grains. The direction of localized plastic strain was on average 45° to the loading direction.

At the end of the 1536th cycle, it could be seen that the short cracks had joined together and formed several long cracks within the material (Figure 3.12a). While a number of grain boundaries had large PEEQ values in range of about 6-12, the PEEQ values for most of the other grain boundaries were between 1.5 and 3.5 (Figure 3.12b). In addition, The PEEQ values for the regions inside the grains had increased to a range of 2 to 3.5. It was observed that the cracks propagated rapidly during the next 300 cycles (Figure 3.13a). However, as shown in Figure 3.13b, the PEEQ values of the grain boundaries barely changed during these cycles. Instead, significant cyclic hardening was taking place inside the grains.

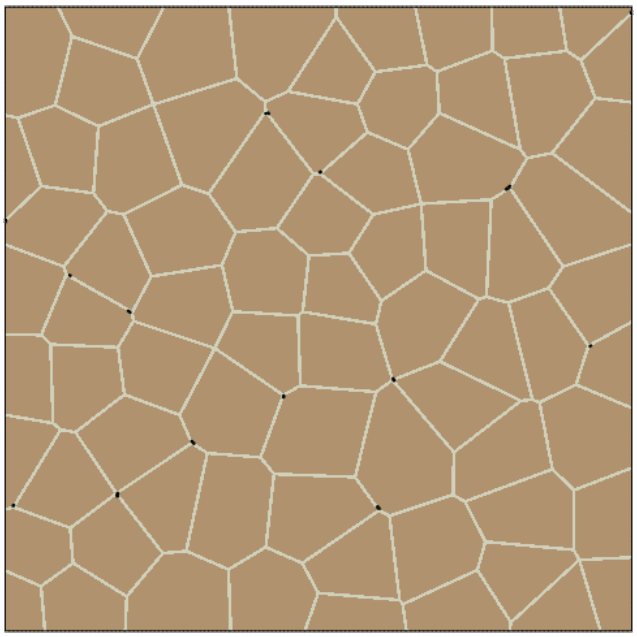

(a)

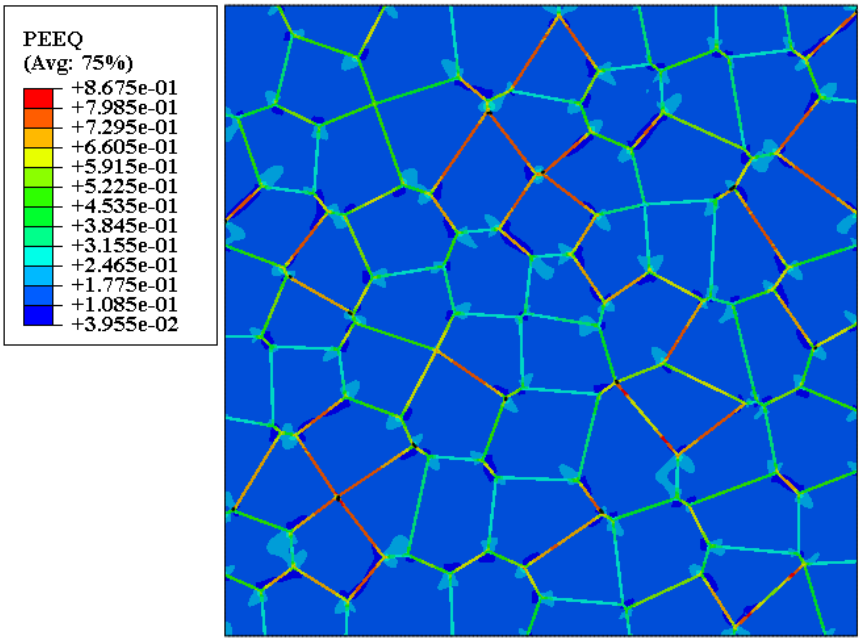

(b)

Figure 3.10 (a) Void formation at grain boundary junctions (b) Equiv. plastic strain accumulation for microstructure model 123-5 after 1250 cycles.

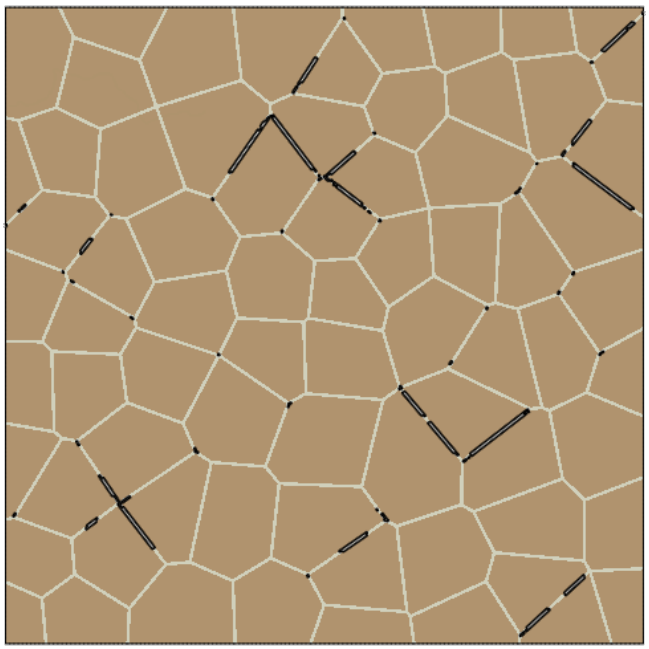

(a)

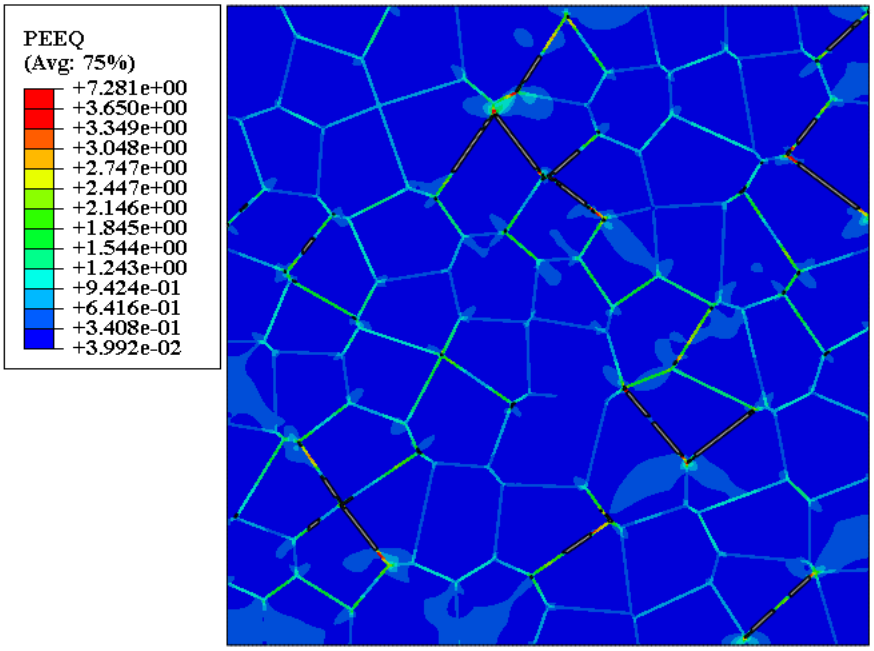

(b)

Figure 3.11 (a) Formation of short cracks (b) Equiv. plastic strain accumulation for microstructure model 123-5 after 1436 cycles.

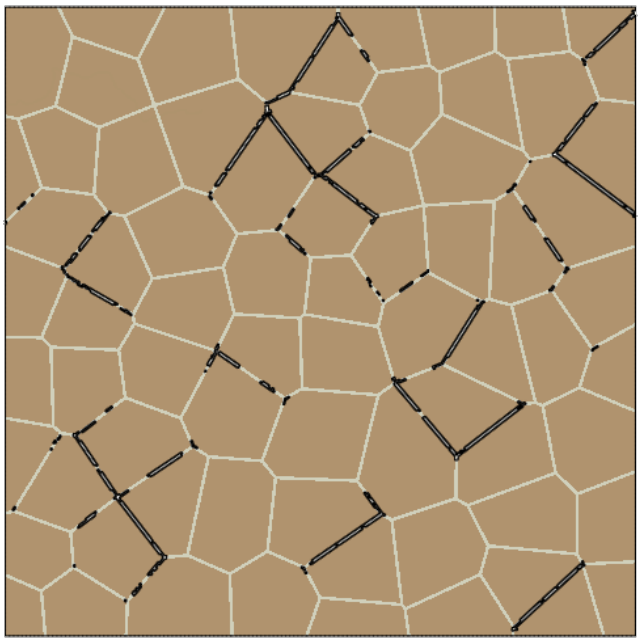

(a)

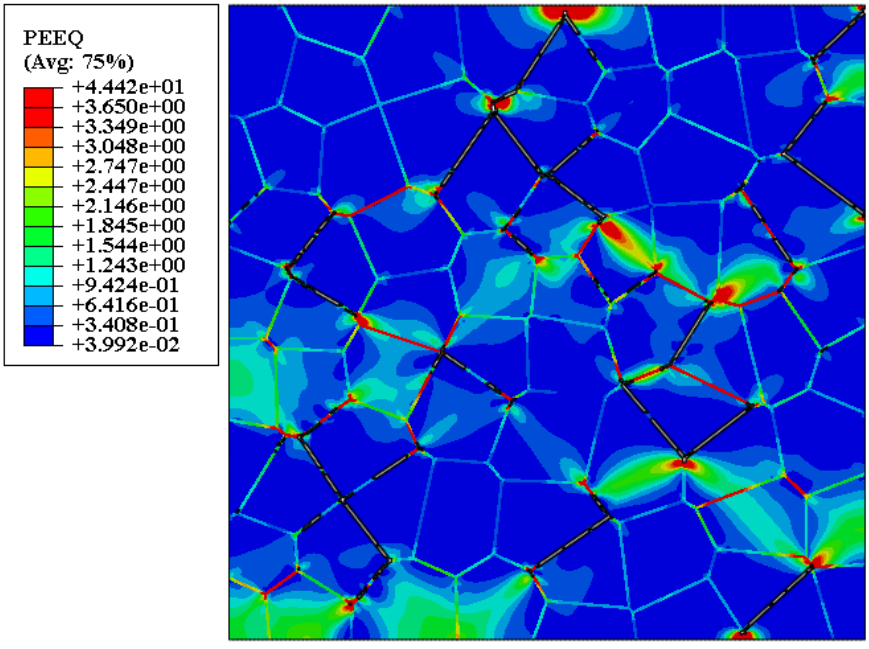

(b)

Figure 3.12 (a) Propagation of cracks (b) Equiv. plastic strain accumulation for microstructure model 123-5 after 1536.

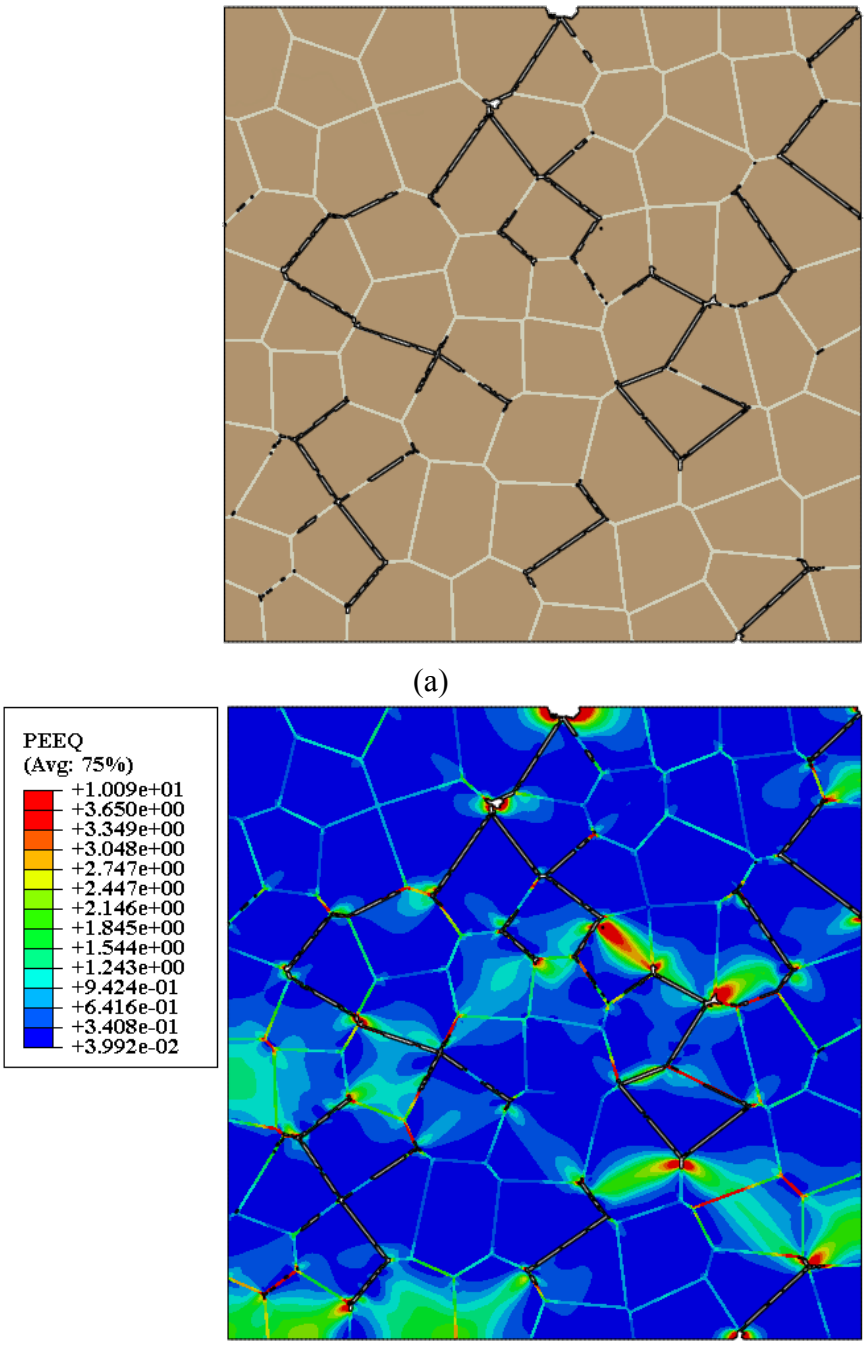

Figure 3.13 (a) Formation of a major crack (b) Equiv. plastic strain accumulation for microstructure model 123-5 after 1836 cycles.

From the 1837th cycle until the final failure (3136th cycle), very slow crack propagation was observed. The reason was that during these cycles, transgranular fracture mechanism was dominant (Figure 3.14), which requires much more energy compared to the intergranular fracture through the ferritic grain boundaries (Wang *et al.* 2013). For the microstructural models, it was assumed that the PE ferrite at the grain boundaries is a continuous network. However, in the actual microstructure of standard rail steels, PE ferrite is partially discontinuous. Since largely strained PE ferrite at the grain boundaries facilitates the crack initiation and growth, this assumption would result in a lower number of cycles to failures compared to the ones reported in the literature (Ahlstrom & Karlsson 2009).

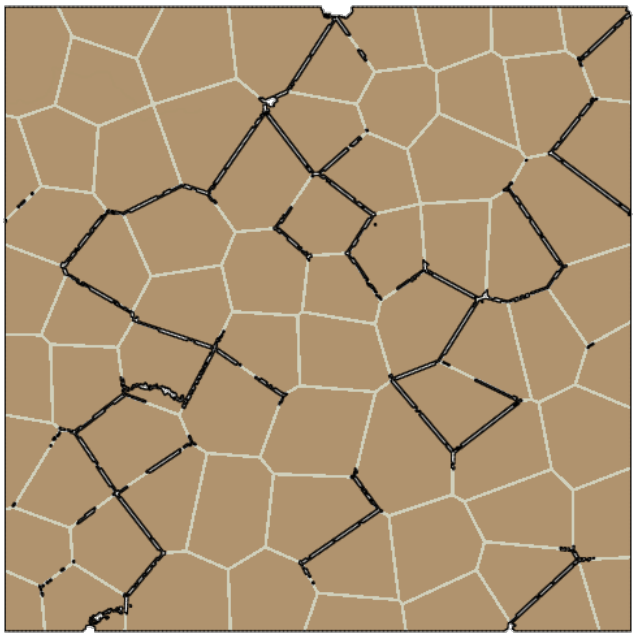

Figure 3.14 Final failure of microstructure model 123-5 after 3136 cycles.

3.2.3. Effect of microstructural characteristics on fatigue life

Besides the microstructure model with a grain size of 123 μm and grain boundary width of 5 μm (ferrite content of 12%), two other microstructure models with the same grain size of

123 μm and different grain boundary widths of 7.5 and 10 μm (ferrite contents of 18 and 24%, respectively) were analyzed to see how the grain boundary width affects the fatigue life. In addition, a microstructure model with grain size of 61 μm and grain boundary width of 5 μm (ferrite content of 24%) was utilized to evaluate the effect of grain size. Five (5) randomly generated domains were used for each microstructure model. For each microstructure model, the domain whose number of cycles to failure (N_f) was closest to the average was used.

The number of cycles to damage initiation and the number of cycles to failure obtained from the simulations on the microstructure models are presented in Figs. 3.15 and 3.16, respectively. The microstructure models were labeled based on their grain sizes and grain boundaries widths (e.g. microstructure model 123-5). The average N_{int} for microstructure models 123-5, 123-7.5, 123-10 and 61-5 were 656, 594, 616 and 614, respectively. The average N_{int} for microstructure models 123-7.5, 123-10 and 61-5 were 9.9, 6.3 and 6.6 % different from the average N_{int} for the microstructure model 123-5, respectively. This indicated that the change in microstructural characteristics had minor effect on the N_{int}. However, it was observed that the N_f was significantly dependent on the microstructural characteristics. The average N_f for microstructure models 123-7.5, 123-10 and 61-5 were 28.2, 40.5 and 41.3 % different from the average N_f for the microstructure model 123-5, respectively. This indicated that increasing the PE ferrite content would result in a lower fatigue life, which is in agreement with the experimental results reported by Garnham and Davis (2008). For further analysis, the PEEQ contour plots of the microstructure models 123-7.5, 123-10 and 61-5 were compared to the ones from the microstructure model 123-5 at a certain stages of the fatigue life.

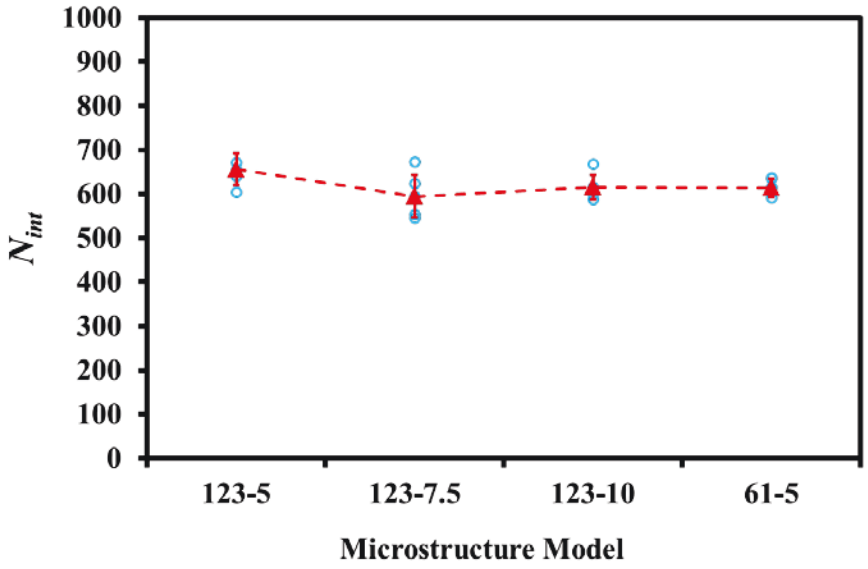

Figure 3.15 Effect of microstructural characteristics on number of cycles to damage initiation (N_{int}).

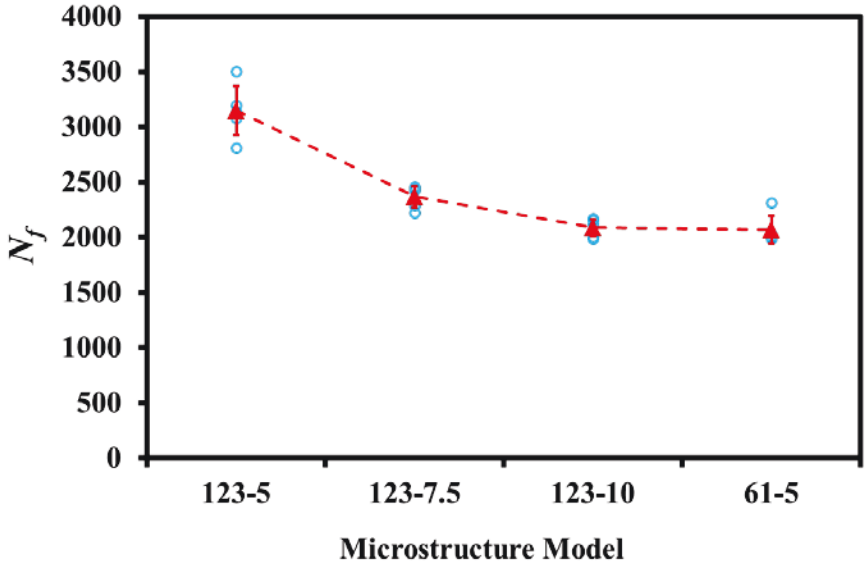

Figure 3.16 Effect of microstructural characteristics on number of cycles to final failure (N_f).

3.2.3.1. Effect of grain boundary width

Figs. 3.17 and 3.18 show the PEEQ contour plots for the microstructure model 123-7.5 at the end of 1423th cycle and microstructure model 123-10 at the end of 1416th cycle, respectively. It could be seen that increasing the grain boundary width had resulted in a larger portion of the grain boundaries with PEEQ values between 1.5 and 2.5. As mentioned previously, largely strained ferritic grain boundaries are locations of crack initiation and propagation. Therefore, a larger portion of these grain boundaries would accelerate the crack growth rate. Also, the largely strained grain boundaries in the microstructure models 123-5 and 123-7.5 are located in separated regions, while in the microstructure model 123-10 they had formed a continuous network. The PEEQ contour plots along with the crack profiles at the end of 1823th cycles for the microstructure model 123-7.5 and at the end of 1816th cycle for the microstructure model 123-10 are shown in the Figs. 3.19 and 3.20, respectively. Unlike the microstructure model 123-5, a major crack with a few small gaps had formed in both of these microstructure models. For the microstructure model 123-7.5 the final failure happened at the 2424th cycle (Figure 3.21a), whereas the microstructure model 123-10 failed at the 2116th cycle (Figure 3.21b). The reason for this difference was that there were fewer largely strained grain boundaries in the microstructure model 123-7.5 compared to the microstructure model 123-10, and the crack was blunted temporarily during the final stage of the fatigue life.

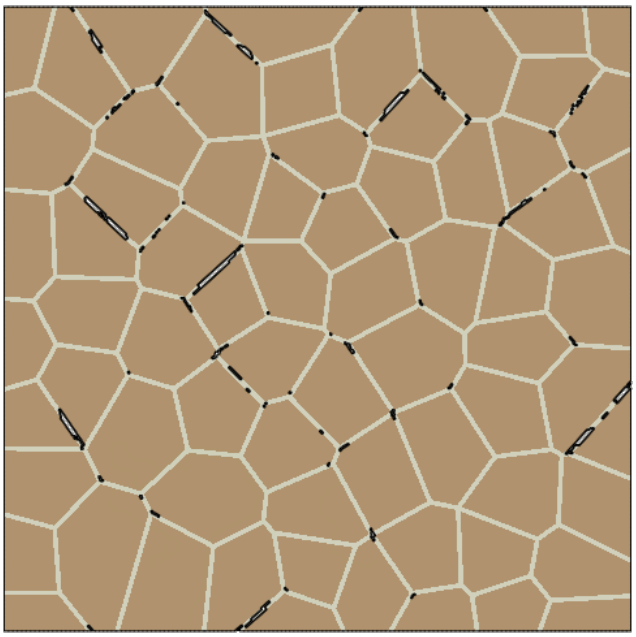

(a)

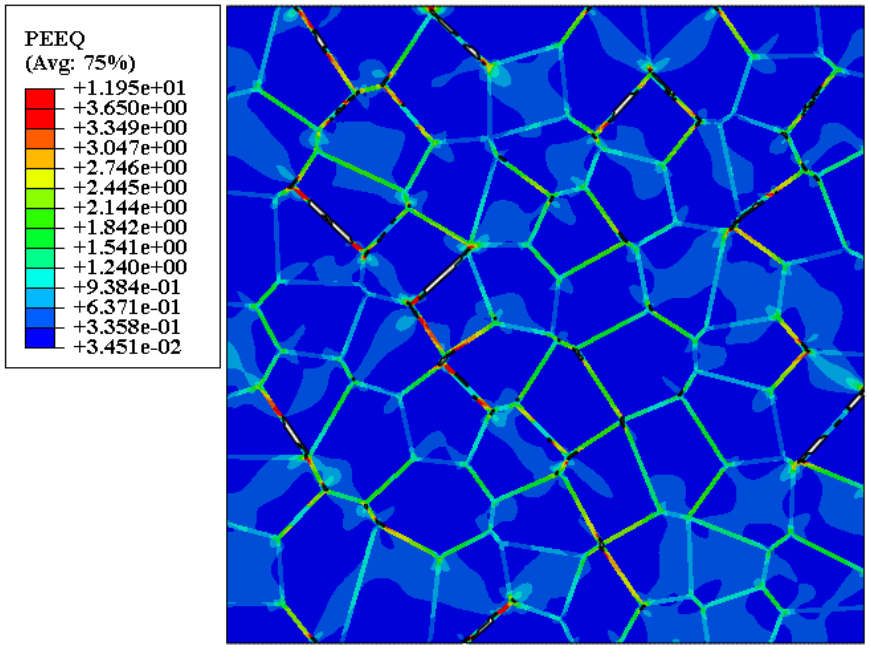

(b)

Figure 3.17 (a) Formation of short cracks (b) Equiv. plastic strain accumulation for microstructure model 123-7.5 after 1423 cycles.

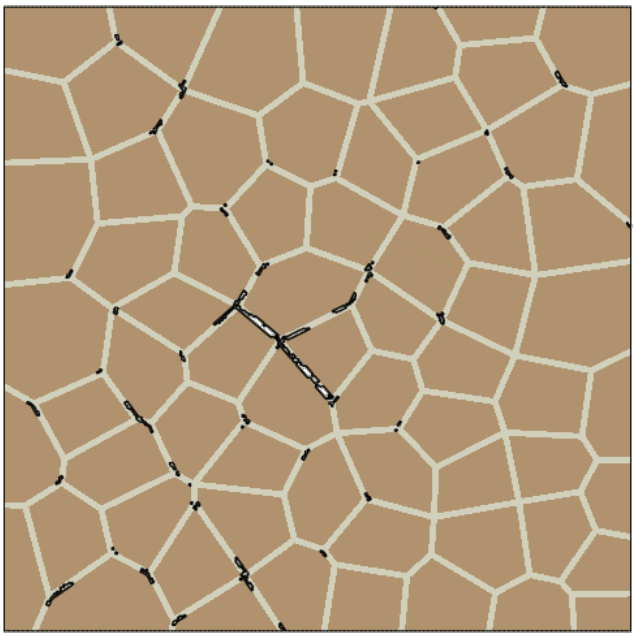

(a)

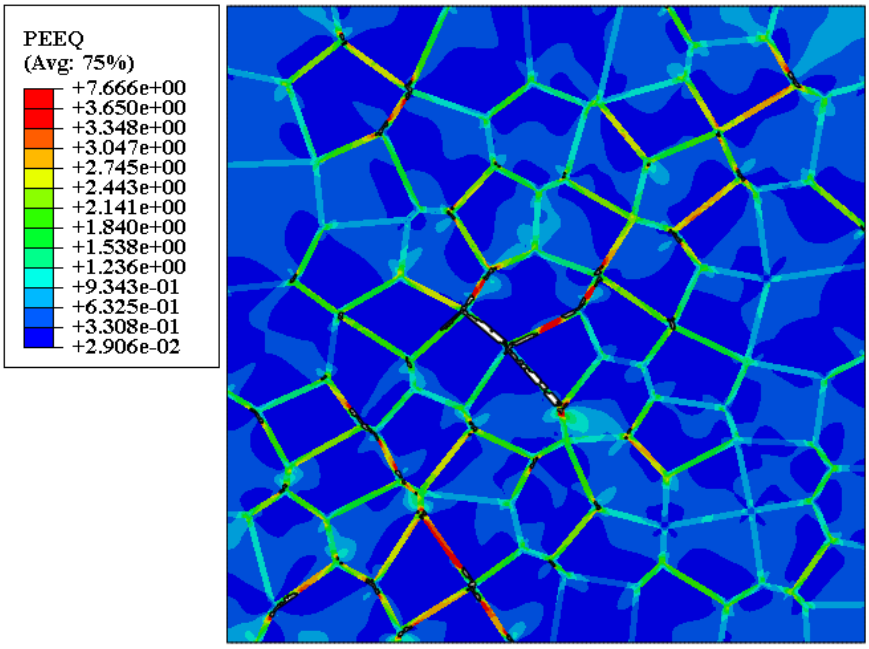

(b)

Figure 3.18 (a) Formation of short cracks (b) Equiv. plastic strain accumulation for microstructure model 123-10 after 1416 cycles.

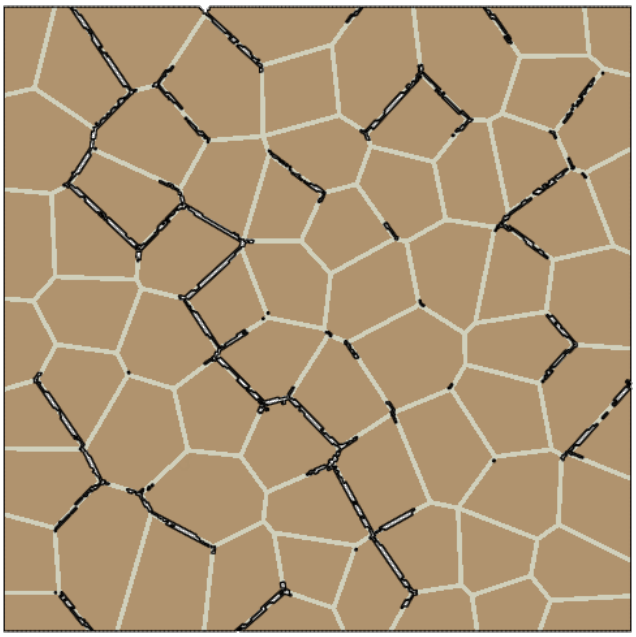

(a)

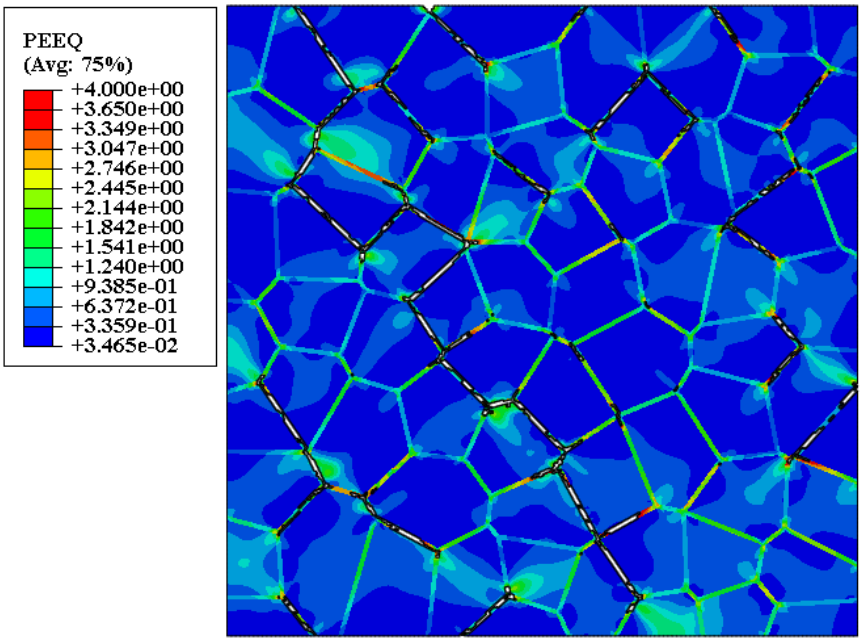

(b)

Figure 3.19 (a) Formation of a major crack (b) Equiv. plastic strain accumulation for microstructure model 123-7.5 after 1823 cycles.

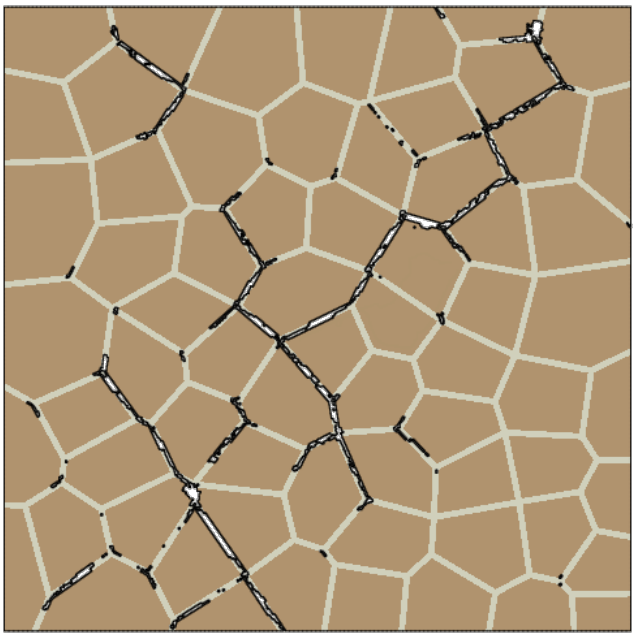

(a)

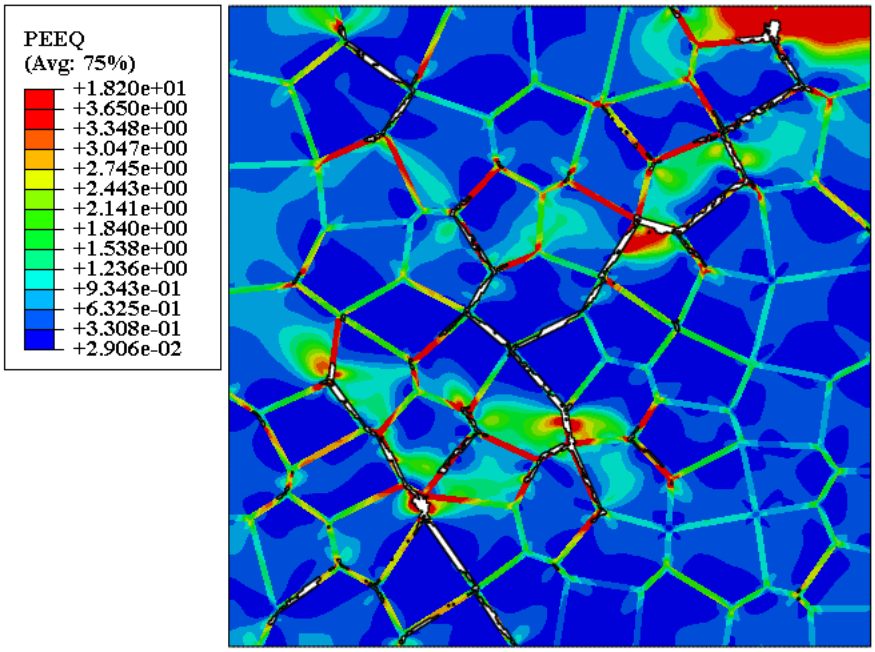

(b)

Figure 3.20 (a) Formation of a major crack (b) Equiv. plastic strain accumulation for microstructure model 123-10 after 1816 cycles.

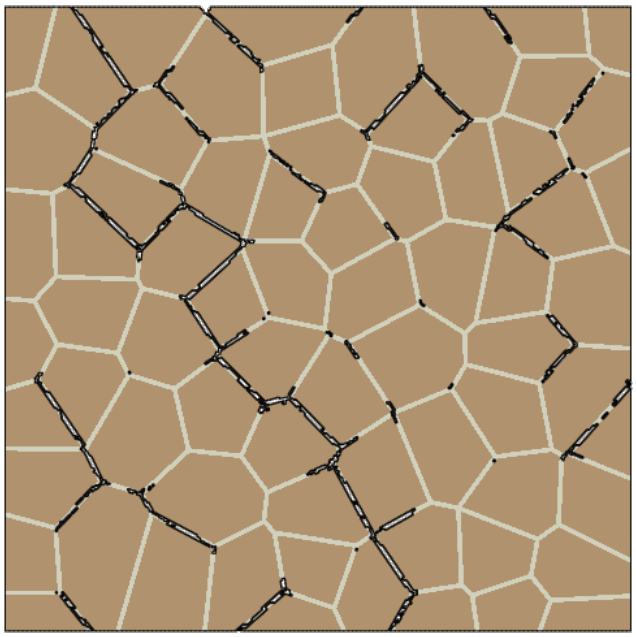

(a)

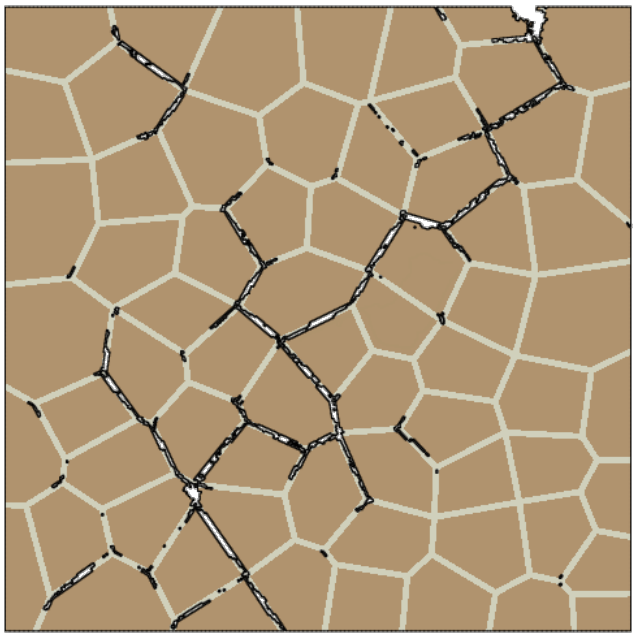

(b)

Figure 3.21 Finale failure of (a) microstructure model 123-7.5 after 2424 cycles (b) microstructure model 123-10 after 2116 cycles.

3.2.3.2. Effect of grain size

Figure 3.22 shows the contour plot of PEEQ for the microstructure model 61-5 at the end of 1437th cycle. It was observed that most of the grain boundaries were largely strained and had PEEQ values were ranging between 1 and 2, which was slightly smaller than the range observed for the microstructure models 123-7.5 and 123-10. As shown in Figure 3.23, this microstructure model had a major crack with only a small gap at the end of 1837th cycle. It could be seen that the cracks had propagated through pearlite grains at several locations, which indicated that both intergranular and transgranular fracture mechanisms were active. This was due to the fact that it is easier for cracks to propagate through grains with smaller size. As a result, the crack growth rate was accelerated and the final failure for this microstructure model happened at the 2036th cycle (Figure 3.24).

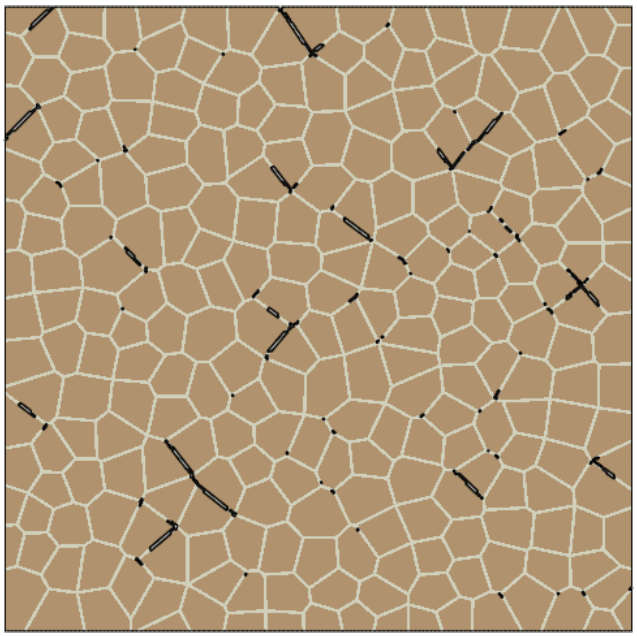

(a)

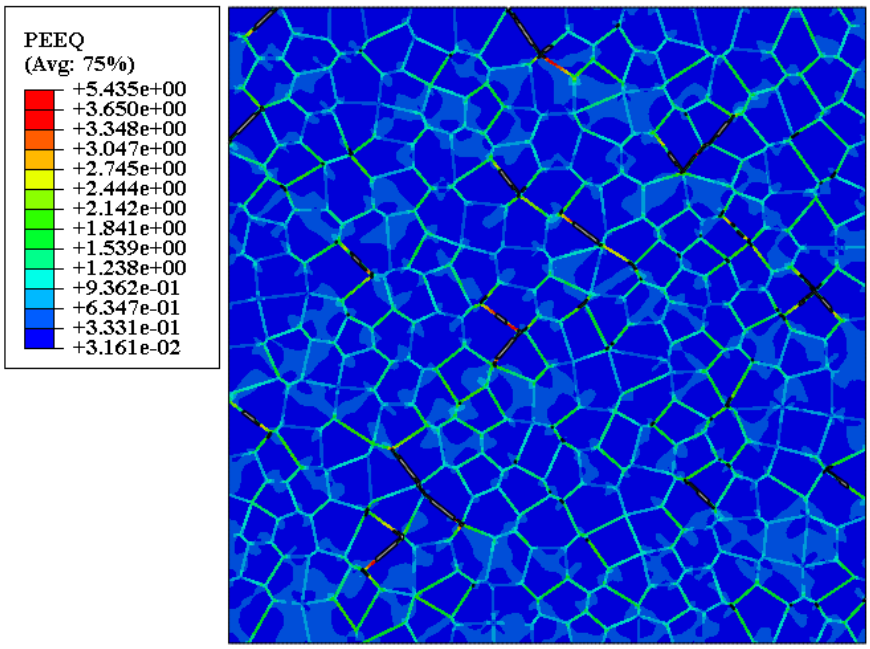

(b)

Figure 3.22 (a) Formation of short cracks (b) Equiv. plastic strain accumulation for microstructure model 61-5 after 1437 cycles.

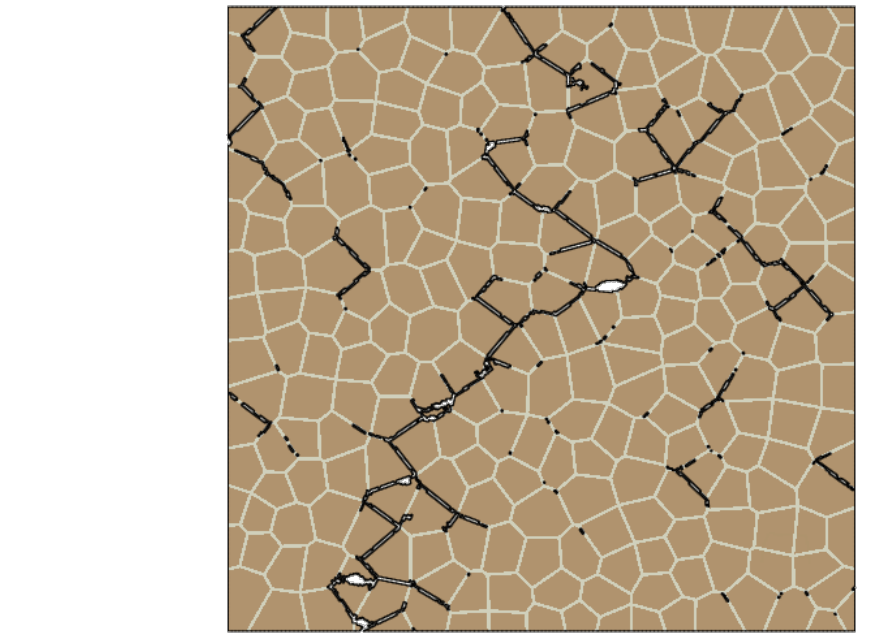

(a)

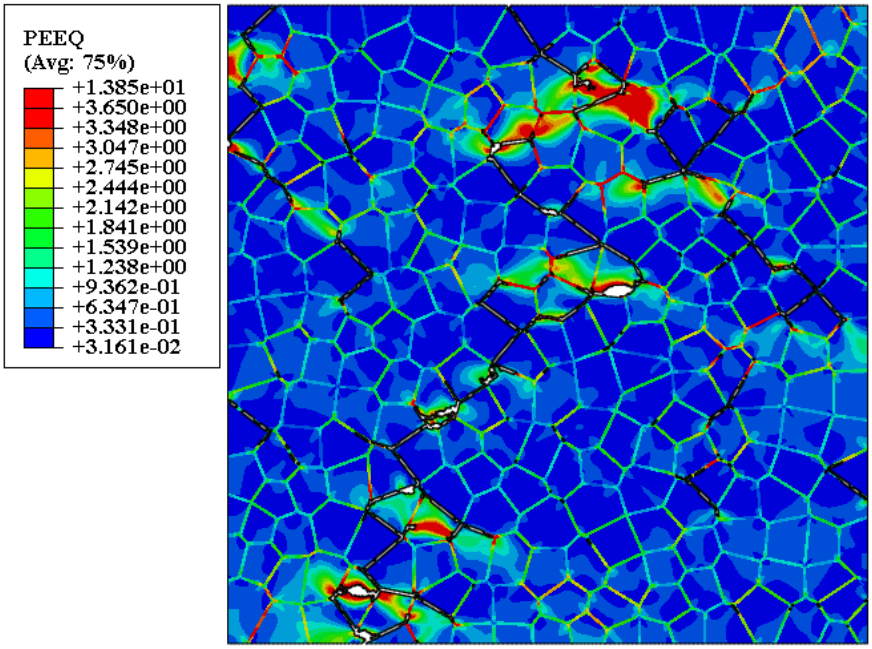

(b)

Figure 3.23 (a) Formation of a major crack (b) Equiv. plastic strain accumulation for microstructure model 61-5 after 1837 cycles.

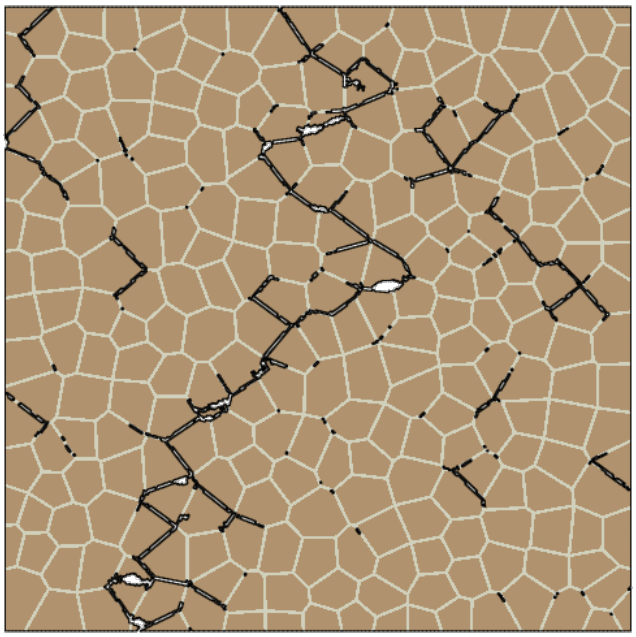

Figure 3.24 Final failure of microstructure model 61-5 after 2036 cycles.

4. Conclusions and Recommendations

4.1. Conclusions

The primary aim of the current study was to investigate the microstructural evolutions in pearlitic rail steels under fatigue loadings and their correlation with RCF cracking, using experimental and numerical methods. Experimental failure analysis was conducted on the rails that have been in use in the US, through optical microscopy and micro-hardness measurements. Besides, a microstructure-based finite element model was built using Voronoi tessellation and continuum damage mechanics to see how the fatigue life of pearlitic rail steels is affected by their microstructural characteristics. Accordingly, the main conclusions are summarized as follows:

- The mid-gauge regions of the rails could be divided into three regions with respect to plastic deformation: largely deformed, mildly deformed and undeformed regions. The thicknesses of these regions were mainly dependent on the grade of rail steel rather than the duration of service life. Moreover, it was observed that the cracks in the mid-gauge regions of the rails had propagated up to the boundaries of their largely deformed regions.
- There were no WELs at the surfaces of mid-gauge regions of the standard rails (Rails 1 and 2), while continuous WELs were observed at the surfaces of the intermediate (Rail 7) and premium (Rails 10 and 12) rails. This was attributed to the fact that head hardened rails are more prone to the grinding-induced WEL formation.

- Decarburized layers were observed at the plastic flow lips of all the rails except Rail 7. These decarburized layers may act as the initiation sites of reverse transverse defects.
- Numerical simulations showed occurrence of strain partitioning between PE ferrite and pearlite under fatigue loading, with preferential strain accumulation in PE ferrite. As a result, the initial fatigue cracks initiation and propagation took place along the strained PE ferrite grain boundaries.
- Increasing the PE ferrite content of the models through increasing the grain boundary widths or decreasing the grain size, led to lower fatigue lives.

4.2. Recommendations for Future Work

In order to further the current work in the future, the following recommendations are proposed:

- The plastically deformed regions and zones observed in the mid-gauge and gauge corner regions can be examined using a scanning electron microscope (SEM) equipped with electron backscatter diffraction (EBSD) system.
- In addition to the mentioned characterization methods, transmission electron microscope (TEM) can be utilized to characterize the WELs observed at the surface of the rails.
- The formation of decarburized layers at the plastic flow lips and their correlation with reverse transverse defects can be studied.

- Fully reversed strain controlled uniaxial LCF test can be conducted to obtain the hardening and damage parameters of the pearlitic rail steels. In addition, nanoindenation can be utilized to acquire these parameters for the PE ferrite.
- To create more realistic microstructure models, cementite lamellae and crystallographic orientations can be included in the simulations. Also, microstructure models can be built using the micrographs obtained from optical microscopy or EBDS.

Bibliography

Ahlström, J. & Karlsson, B. (2009). Modified railway wheel steels: Production and evaluation of mechanical properties with emphasis on low-cycle fatigue behavior. *Metallurgical and Materials Transactions A: Physical Metallurgy and Materials Science*, 40(7):1557–1567.

Ahlström, J. & Karlsson, B. (2005). Fatigue behaviour of rail steel - A comparison between strain and stress controlled loading. *Wear*, 258(7–8):1187–1193.

Al-Juboori, A., Wexler, D., Li, H., Zhu, H., Lu, C., McCusker, A., McLeod, J., Pannil, S. & Wang, Z. (2017). Squat formation and the occurrence of two distinct classes of white etching layer on the surface of rail steel. *International Journal of Fatigue*, 104:52–60.

Alwahdi, F. A. M., Kapoor, A. & Franklin, F. J. (2013). Subsurface microstructural analysis and mechanical properties of pearlitic rail steels in service. *Wear*, 302(1–2):1453–1460.

AREMA. (2010). Chapter 4. In *Manual for Railway Engineering*. Lanham, MD: American Railway Engineering and Maintenance of Way Association.

ASTM Int. (2016). ASTM E384-16: Standard Test Method for Microindentation Hardness of Materials. In *ASTM Standards*. West Conshohocken, PA: American Society for Testing and Materials.

Benoît, D., Salima, B. & Marion, R. (2016). Multiscale characterization of head check initiation on rails under rolling contact fatigue: Mechanical and microstructure analysis. *Wear*, 366–367:383–391.

Beynon, J. H., Garnham, J. E. & Sawley, K. J. (1996). Rolling contact fatigue of three pearlitic rail steels. *Wear*, 192(1–2):94–111.

CAC. (2015). Transportation & Ports. Retrieved from https://www.coal.ca/coal-resources/about-the-coal-industry/transportation-ports/.

Cannon, D. F., Edel, K. O., Grassie, S. L. & Sawley, K. (2003). Rail defects: An overview. *Fatigue and Fracture of Engineering Materials and Structures*, 26(10):865–886.

CAPP. (2015). *Crude Oil Forecast, Markets & Transportation*.

Carroll, R. I. & Beynon, J. H. (2006). Decarburisation and rolling contact fatigue of a rail steel. *Wear*, 260(4–5):523–537.

Carroll, R. I. & Beynon, J. H. (2007). Rolling contact fatigue of white etching layer: Part 1. Crack morphology. *Wear*, 262(9–10):1253–1266.

Chaboche, J. L. (1988). Continuum damage mechanics: Part I— General Concepts. *Journal of Applied Mechanics*, 55(1):59–64.

Chaboche, J. L. (1991). On some modifications of kinematic hardening to improve the description of ratchetting effects. *International Journal of Plasticity*, 7(7):661–678.

Chen, H., Zhang, C., Liu, W., Li, Q., Chen, H., Yang, Z. & Weng, Y. (2016). Microstructure evolution of a hypereutectoid pearlite steel under rolling-sliding contact loading. *Materials Science and Engineering: A*, 655(10):50–59.

Dassault Systemes Simulia Corporation. (2014). Abaqus, V. 6.14 Documentation.

Dhua, S. K., Ray, A., Sen, S. K., Prasad, M. S., Mishra, K. B. & Jha, S. (2000). Influence of nonmetallic inclusion characteristics on the mechanical properties of rail steel. *Journal of Materials Engineering and Performance*, 9(6):700–709.

Donzella, G., Faccoli, M., Mazzù, A., Petrogalli, C. & Roberti, R. (2011). Progressive damage assessment in the near-surface layer of railway wheel-rail couple under cyclic contact. *Wear*, 271(1–2):408–416.

Du, W., Luo, Y., Wang, Y., Chen, S. & Yu, D. (2017). A new energy-based method to evaluate low-cycle fatigue damage of AISI H11 at elevated temperature. *Fatigue and Fracture of Engineering Materials and Structures*, 40(6):994–1004.

Dziubiński, J. (1991). Fatigue failure criterion based on plastic strain energy density applied to welds. *International Journal of Fatigue*, 13(3):223–226.

Eden, H. C., Garnham, J. E. & Davis, C. L. (2005). Influential microstructural changes on rolling contact fatigue crack initiation in pearlitic rail steels. *Materials Science and Technology*, 21(6):623–629.

Ekberg, A., Åkesson, B. & Kabo, E. (2014). Wheel/rail rolling contact fatigue - Probe, predict, prevent. *Wear*, 314(1–2):2–12.

Ekberg, A. & Kabo, E. (2005). Fatigue of railway wheels and rails under rolling contact and thermal loading-an overview. *Wear*, 258(7–8):1288–1300.

Eriksson, A., Einarsrud, M. A., & Grande, T. (2011). Materials Science Aspects Relevant for High-Temperature Electrochemistry. In *Solid State Electrochemistry II: Electrodes, Interfaces and Ceramic Membranes* (pp. 415–465). Weinheim: Wiley-VCH Verlag GmbH & KGaA.

Franklin, F. J., Gahlot, A., Fletcher, D. I., Garnham, J. E. & Davis, C. (2011). Three-dimensional modelling of rail steel microstructure and crack growth. *Wear*, 271(1–2):357–363.

Franklin, F. J., Garnham, J. E., Fletcher, D. I., Davis, C. L. & Kapoor, A. (2008). Modelling rail steel microstructure and its effect on crack initiation. *Wear*, 265(9–10):1332–1341.

Garnham, J. E. & Davis, C. L. (2011). Very early stage rolling contact fatigue crack growth in pearlitic rail steels. *Wear*, 271(1–2):100–112.

Garnham, J. E., Ding, R. G. & Davis, C. L. (2010). Ductile inclusions in rail, subject to compressive rolling-sliding contact. *Wear*, 269(11–12):733–746.

Garnham, J. E., Fletcher, D. I., Davis, C. L. & Franklin, F. J. (2011). Visualization and modelling to understand rail rolling contact fatigue cracks in three dimensions. *Proceedings of the Institution of Mechanical Engineers, Part F: Journal of Rail and Rapid Transit*, 225(2):165–178.

Garnham, J. E., Franklin, F. J., Fletcher, D. I., Kapoor, A. & Davis, C. L. (2007). Predicting the life of steel rails. *Proceedings of the Institution of Mechanical Engineers, Part F: Journal of Rail and Rapid Transit*, 221(1):45–58.

Garnham, J. E. & Davis, C. L. (2008). The role of deformed rail microstructure on rolling contact fatigue initiation. *Wear*, 265(9–10):1363–1372.

Gould, B., Greco, A., Stadler, K., Vegter, E. & Xiao, X. (2017). Using advanced tomography techniques to investigate the development of White Etching Cracks in a prematurely failed field bearing. *Tribology International*, 116(June):362–370.

Haidemenopoulos, G. N., Sarafoglou, P. I., Christopoulos, P. & Zervaki, A. D. (2016). Rolling contact fatigue cracking in rails subjected to in-service loading. *Fatigue and Fracture of Engineering Materials and Structures*, 39(9):1161–1172.

Hohenwarter, A., Taylor, A., Stock, R. & Pippan, R. (2011). Effect of large shear deformations on the fracture behavior of a fully pearlitic steel. *Metallurgical and Materials Transactions A: Physical Metallurgy and Materials Science*, 42(6):1609–1618.

Jalalahmadi, B. & Sadeghi, F. (2010). A Voronoi FE Fatigue Damage Model for Life Scatter in Rolling Contacts. *Journal of Tribology*, 132(2):021404.

Kapp, M. W., Hohenwarter, A., Wurster, S., Yang, B. & Pippan, R. (2016). Anisotropic deformation characteristics of an ultrafine- and nanolamellar pearlitic steel. *Acta Materialia*, 106:239–248.

Larijani, N., Brouzoulis, J., Schilke, M. & Ekh, M. (2014). The effect of anisotropy on crack propagation in pearlitic rail steel. *Wear*, 314(1–2):57–68.

Lejeunes, S. & Bourgeois, S. (2011). Une Toolbox Abaqus pour le calcul de propriétés effectives de milieux hétérogènes. *10Ème Colloque National En Calcul Des Structures*, 1–9. Retrieved from https://hal.archives-ouvertes.fr/hal-00592866

Lemaitre, J., & Desmorat, R. (2005). *Engineering damage mechanics: ductile, creep, fatigue and brittle failures*. Berlin: Springer Science & Business Media.

Li, S., Wu, J., Petrov, R. H., Li, Z., Dollevoet, R. & Sietsma, J. (2016). "Brown etching layer": A possible new insight into the crack initiation of rolling contact fatigue in rail steels? *Engineering Failure Analysis*, 66:8–18.

Linz, M., Cihak-Bayr, U., Trausmuth, A., Scheriau, S., Künstner, D. & Badisch, E. (2015). EBSD study of early-damaging phenomena in wheel-rail model test. *Wear*, 342–343:13–21.

Magel, E. E. (2011). *Rolling Contact Fatigue: A Comprehensive Review* (No. DOT/FRA/ORD-11/24). U.S. Department of Transportation, Federal Railroad Administration, Office of Railroad Policy and Development.

Magel, E., Mutton, P., Ekberg, A. & Kapoor, A. (2016). Rolling contact fatigue, wear and broken rail derailments. *Wear*, 366–367:249–257.

Messaadi, M. & Steenbergen, M. (2018). Stratified surface layers on rails. *Wear*, 414–415:151–162.

Moeini, G., Ramazani, A., Sundararaghavan, V. & Koenke, C. (2017). Micromechanical modeling of fatigue behavior of DP steels. *Materials Science and Engineering A*, 689:89–95.

Mughrabi, H. (2015). Microstructural mechanisms of cyclic deformation, fatigue crack initiation and early crack growth. *Philosophical Transactions of the Royal Society A: Mathematical, Physical and Engineering Sciences*, 373(2038).

Najdahmadi, A., Zarei-Hanzaki, A. & Farghadani, E. (2014). Mechanical properties enhancement in Ti-29Nb-13Ta-4.6Zr alloy via heat treatment with no detrimental effect on its biocompatibility. *Materials and Design*, 54:786–789.

Najdahmadi, A., Lakey, J. R. & Botvinick, E. (2018). Structural Characteristics and Diffusion Coefficient of Alginate Hydrogels Used for Cell Based Drug Delivery. *MRS Advances*, 3(40):2399–2408.

Pal, S., Daniel, W. J. T., Valente, C. H. G., Wilson, A. & Atrens, A. (2012). Surface damage on new AS60 rail caused by wheel slip. *Engineering Failure Analysis*, 22:152–165.

Paulson, N. R., Evans, N. E., Bomidi, J. A. R., Sadeghi, F., Evans, R. D. & Mistry, K. K. (2015). A finite element model for rolling contact fatigue of refurbished bearings. *Tribology International*, 85:1–9.

Preibisch, S., Saalfeld, S. & Tomancak, P. (2009). Globally optimal stitching of tiled 3D microscopic image acquisitions. *Bioinformatics*, 25(11):1463–1465.

Rasmussen, C. J., Fæster, S., Dhar, S., Quaade, J. V., Bini, M. & Danielsen, H. K. (2017). Surface crack formation on rails at grinding induced martensite white etching layers. *Wear*, 384–385(April):8–14.

Roberts, G., Ward, R. M., Strangwood, M. & Davis, C. L. (2013). Use of misorientation values to further understand deformation in rail steels. *Ironmaking & Steelmaking*, 40(2):92–97.

Sadeghi, F., Jalalahmadi, B., Slack, T. S., Raje, N. & Arakere, N. K. (2009). A Review of Rolling Contact Fatigue. *Journal of Tribology*, 131(4):041403.

Sahay, S. S., Mohapatra, G. & Totten, G. E. (2009). Overview of Pearlitic Rail Steel: Accelerated Cooling, Quenching, Microstructure, and Mechanical Properties. *Journal of ASTM International*, 6(7):102021.

Schilke, M., Larijani, N. & Persson, C. (2014). Interaction between cracks and microstructure in three dimensions for rolling contact fatigue in railway rails. *Fatigue and Fracture of Engineering Materials and Structures*, 37(3):280–289.

Schindelin, J., Arganda-Carreras, I., Frise, E., Kaynig, V., Longair, M., Pietzsch, T., Preibisch, S., Rueden, C., Saalfeld, S., Schmid, B., Tinevez, J. Y., White, D. J., Hartenstein, V., Eliceiri, K., Tomancak, P. & Cardona, A. (2012). Fiji: An open-source platform for biological-image analysis. *Nature Methods*, 9(7):676–682.

Schleinzer, G. & Fischer, F. . (2001). Residual stress formation during the roller straightening of railway rails. *International Journal of Mechanical Sciences*, 43(10):2281–2295.

Seo, J., Kwon, S. & Lee, D. (2011). Effects of surface defects on rolling contact fatigue of rail. *Procedia Engineering*, 10:1274–1278.

Steenbergen, M. (2015). Squat formation and rolling contact fatigue in curved rail track. *Engineering Fracture Mechanics*, 143:80–96.

Steenbergen, M. (2017). Rolling contact fatigue: Spalling versus transverse fracture of rails. *Wear*, 380–381:96–105.

Steenbergen, M. (2016). Rolling contact fatigue in relation to rail grinding. *Wear*, 356–357:110–121.

Steenbergen, M. & Dollevoet, R. (2013). On the mechanism of squat formation on train rails – Part II: Growth. *International Journal of Fatigue*, 47:373–381.

Thévenaz, P. & Unser, M. (2007). User-friendly semiautomated assembly of accurate image mosaics in microscopy. *Microscopy Research and Technique*, 70(2):135–146.

Tillberg, J., Larsson, F. & Runesson, K. (2009). A study of multiple crack interaction at rolling contact fatigue loading of rails. *Proceedings of the Institution of Mechanical Engineers, Part F: Journal of Rail and Rapid Transit*, 223(4):319–330.

TSB. (2013). *Railway Investigation Report R13E0142*. Retrieved from http://www.bst-tsb.gc.ca/eng/rapports-reports/rail/2013/r13e0142/r13e0142.asp.

Tyfour, W. R., Beynon, J. H. & Kapoor, A. (1996). Deterioration of rolling contact fatigue life of pearlitic rail steel due to dry-wet rolling-sliding line contact. *Wear*, 197(1–2):255–265.

Wang, W. J., Guo, H. M., Du, X., Guo, J., Liu, Q. Y. & Zhu, M. H. (2013). Investigation on the damage mechanism and prevention of heavy-haul railway rail. *Engineering Failure Analysis*, 35:206–218.

Wetscher, F., Stock, R. & Pippan, R. (2007). Changes in the mechanical properties of a pearlitic steel due to large shear deformation. *Materials Science and Engineering A*, 445–446:237–243.

Wu, J., Petrov, R. H., Naeimi, M., Li, Z., Dollevoet, R. & Sietsma, J. (2016). Laboratory simulation of martensite formation of white etching layer in rail steel. *International Journal of Fatigue*, 91:11–20.

Zeng, D., Lu, L., Gong, Y., Zhang, Y. & Zhang, J. (2017). Influence of solid solution strengthening on spalling behavior of railway wheel steel. *Wear*, 372–373:158–168.

Zhang, X., Zhang, L., Yang, W. & Dong, Y. (2017). Characterization of MnS Particles in Heavy Rail Steels Using Different Methods. *Steel Research International*, 88(1):1–16.

Zhou, T. & Huang, C. (2015). Simulation of crack propagation in single phase ceramic tool materials. *Computational Materials Science*, 104:177–184.

Zhou, Y., Wang, S., Wang, T., Xu, Y. & Li, Z. (2014). Field and laboratory investigation of the relationship between rail head check and wear in a heavy-haul railway. *Wear*, 315(1–2):68–77.